In compliance with the
Canadian Privacy Legislation
some supporting forms
may have been removed from
this dissertation.

While these forms may be included
in the document page count,
their removal does not represent
any loss of content from the dissertation.

# University of Alberta

## Fabrication and Characterization of Dye Sensitized Solar Cells Incorporating Obliquely Deposited Layers

by

Michael John Colgan

A thesis submitted to the Faculty of Graduate Studies and Research in partial fulfillment of the requirements for the degree of Master of Science

Department of Electrical and Computer Engineering

Edmonton, Alberta, Canada
Fall 2003

National Library of Canada
Bibliothèque nationale du Canada

Acquisitions and Bibliographic Services
Acquisisitons et services bibliographiques

395 Wellington Street
Ottawa ON K1A 0N4
Canada

395, rue Wellington
Ottawa ON K1A 0N4
Canada

*Your file Votre référence*
*ISBN: 0-612-87742-6*
*Our file Notre référence*
*ISBN: 0-612-87742-6*

The author has granted a non-exclusive licence allowing the National Library of Canada to reproduce, loan, distribute or sell copies of this thesis in microform, paper or electronic formats.

L'auteur a accordé une licence non exclusive permettant à la Bibliothèque nationale du Canada de reproduire, prêter, distribuer ou vendre des copies de cette thèse sous la forme de microfiche/film, de reproduction sur papier ou sur format électronique.

The author retains ownership of the copyright in this thesis. Neither the thesis nor substantial extracts from it may be printed or otherwise reproduced without the author's permission.

L'auteur conserve la propriété du droit d'auteur qui protège cette thèse. Ni la thèse ni des extraits substantiels de celle-ci ne doivent être imprimés ou aturement reproduits sans son autorisation.

Canada

# University of Alberta

## Library Release Form

**Name of Author:** Michael John Colgan

**Title of Thesis:** Fabrication and Characterization of Dye Sensitized Solar Cells Incorporating Obliquely Deposited Layers

**Degree:** Master of Science

**Year this Degree Granted:** 2003

Permission is hereby granted to the University of Alberta Library to reproduce single copies of this thesis and to lend or sell such copies for private, scholarly or scientific research purposes only.

The author reserves all other publication and other rights in association with the copyright in the thesis, and except as herein before provided, neither the thesis nor any substantial portion thereof may be printed or otherwise reproduced in any material form whatever without the author's prior written permission.

Submitted to the Faculty of Graduate Studies and Research on September 29, 2003
University of Alberta

## University of Alberta

### Faculty of Graduate Studies and Research

The undersigned certify that they have read, and recommend to the Faculty of Graduate Studies and Research for acceptance, a thesis entitled *"Fabrication and Characterization of Dye Sensitized Solar Cells Incorporating Obliquely Deposited Layers"* submitted by Michael John Colgan in partial fulfillment of the requirements for the degree of Master of Science.

Dr. James Miller

Sept. 24, 2003.
Date

## Abstract

This thesis presents the development of three sequential generations of dye sensitized solar cells incorporating obliquely deposited titanium dioxide films as the electron collecting layer. The films were structurally characterized by SEM, TEM, and XRD before examination of their dye retention capabilities. Basic testing of the photovoltaic properties of constructed devices revealed trends relating to deposition and processing parameters that were used to improve the performance of subsequent device generations. Generation III devices yielded energy conversion efficiencies greater than 2%, with short circuit current densities of up to 1.4 $mA/cm^2$, and open circuit voltages of 550 to 635 mV. These cells were compared against devices constructed from conventional nanocrystalline particles and found to have superior performance under the test conditions employed.

## Acknowledgements

For making this experience so much easier for me than many have it, I would like to thank the Natural Sciences and Engineering Research Council of Canada, the Informatics Circle of Research Excellence, and the Alberta Heritage Scholarship Foundation.

For providing funding, such that I need not have worried about the daily costs of research, I would like to thank Micralyne Inc., along with those just mentioned.

For inviting me into his research group, making all this funding available and giving me the space, equipment, encouragement, and freedom to pursue my goals, I would like to thank my supervisor, Dr. Michael Brett.

For his help with many of these experiments and his knowledge of all things chemistry, I would like to thank Dr. Gregory Kiema.

For her skill with the TEM and willingness to answer my endless questions, I would like to thank Barbara Djurfors.

For his ability with the SEM and many hours of pleasant chats, I would like to thank George Braybrook.

For many (perhaps too many) hours of enjoyment wiled away at the foosball table, I would like to thank you, (you know who you are).

For giving me the financial leg up, such that loans did not force me into the workforce, your support, and everything else you've ever done for me, I'd like to thank my parents.

For her patience, her understanding, her care of me, and her love, most of all I'd like to thank Nicole.

## Table of Contents


**1. Chapter One: Introduction ..... 1**

1.1 History ..... 1

1.2 Motivation ..... 2

1.3 Scope ..... 3

**2 Chapter Two: Solar Cells ..... 4**

2.1 Figures of merit ..... 4

2.2 Solid-state ..... 7

2.2.1 Principles of operation ..... 7

2.2.2 Technological developments ..... 9

2.2.3 Maximum efficiencies ..... 13

2.3 Organic ..... 14

2.3.1 Principles of operation ..... 14

2.3.2 Maximum efficiencies ..... 15

2.4 Dye sensitized ..... 15

2.4.1 Principles of operation ..... 16

2.4.1.1 Electron injection ..... 17

2.4.1.2 Charge transport ..... 18

2.4.1.3 Origin of the photovoltage ..... 19

2.4.1.4 Recombination mechanisms ..... 20

2.4.2 Level of development ..... 21

2.4.3 Maximum efficiencies ..... 23

**3 Chapter Three: Generation I Devices: As-deposited Films ..... 24**

3.1 Glancing Angle Deposition ..... 24

3.2 Transparent conductive oxide substrate ..... 27

3.3 Films deposited ..... 29

3.3.1 Deposition ..... 29

3.3.2 Scanning electron microscope analysis ..... 31

3.3.3 Transmission electron microscope analysis ..... 35

3.3.4 Optical transmission ..... 37

3.4 Dye sensitization ..... 38

3.4.1 Dye ..... 38
3.4.2 Solution preparation ..... 38
3.4.3 Sensitization ..... 39
3.4.4 Adsorption ..... 40
3.5 Device construction ..... 42
3.6 Device testing ..... 43
3.6.1 Light source ..... 43
3.6.2 Electrical measurements ..... 44
3.6.3 Device performance ..... 44
**4 Chapter 4: Generation II Devices: Annealed Films ..... 47**
4.1 Annealing ..... 47
4.2 Annealed films ..... 48
4.2.1 Scanning electron microscope analysis ..... 48
4.2.2 Transmission electron microscope analysis ..... 51
4.2.3 X-ray diffraction analysis ..... 52
4.2.4 Optical transmission ..... 53
4.3 Dye sensitization ..... 54
4.3.1 Dye ..... 54
4.3.2 Adsorption ..... 54
4.4 Device performance ..... 55
4.4.1 Annealed GLAD electron collecting layer solar cells ..... 55
4.4.2 Solar cell with nanocrystalline particle collecting layer ..... 57
4.5 Areas of suspicion ..... 60
4.5.1 Light source ..... 60
4.5.2 Substrate ..... 62
4.5.3 Adsorbed water ..... 66
**5 Chapter 5: Generation III Devices: Improved Cells ..... 67**
5.1 Fluorinated tin (IV) oxide glass ..... 67
5.1.1 As-delivered ..... 67
5.1.2 Annealed ..... 68
5.2 Films deposited ..... 69
5.2.1 Deposition ..... 70

5.2.2 Annealing ..... 71
5.2.3 Scanning electron microscope analysis ..... 71
5.2.4 Transmission electron microscope analysis ..... 75
5.2.5 Optical transmission ..... 76
5.3 Dye sensitization ..... 77
5.3.1 Dye ..... 77
5.3.2 Solution preparation ..... 78
5.3.3 Sensitization ..... 78
5.4 Device construction ..... 79
5.5 Device testing ..... 79
5.5.1 Light source ..... 79
5.5.2 Electrical measurements ..... 80
5.5.3 Device performance ..... 81
**6 Chapter 6: Conclusions and Recommendations for Future Work ..... 88**
6.1 Conclusions ..... 88
6.1.1 Crystallinity and composition ..... 88
6.1.2 Deposition angle and efficiency ..... 88
6.1.3 Best results ..... 89
6.2 Recommendations for Future Work ..... 89
6.2.1 Standard testing ..... 89
6.2.2 Parameter variation ..... 90
6.2.3 Surface treatments ..... 90
6.2.4 Stability ..... 90
6.2.5 Fundamental studies ..... 91
6.2.6 Light engineering ..... 91
6.3 And finally ..... 92
**References ..... 93**

## List of Tables

Table 2.1: Semiconductor material bandgaps ..... 12
Table 2.2: Solid-state solar cell performance ..... 14
Table 3.1: Generation I films ..... 31
Table 3.2: Generation I dye incorporation ..... 41
Table 3.3: Generation I device performance ..... 44
Table 4.1: Generation II films ..... 48
Table 4.2: Generation II dye incorporation ..... 55
Table 4.3: Generation II device performance ..... 55
Table 4.4: Nanocrystalline particle device performance ..... 59
Table 5.1: Generation III films ..... 71
Table 5.2: Generation III device performance ..... 81

## List of Figures


Figure 2.1: Current-voltage characteristics of solar cells ..... 4
Figure 2.2: Solar cell equivalent circuit ..... 5
Figure 2.3: Standard AM 1.5 spectrum. ..... 7
Figure 2.4: Process of charge separation in a p-n junction ..... 8
Figure 2.5: Transmission with anti-reflection coating ..... 10
Figure 2.6: Simple light trapping structures ..... 11
Figure 2.7: Functioning of a tandem cell ..... 12
Figure 2.8: Dye sensitized solar cell ..... 17
Figure 2.9: Helmholtz layer. ..... 18
Figure 2.10: Relative energy levels present within the dye sensitized solar cell. ..... 20
Figure 3.1: GLAD: Shadowing and limited adatom mobility. ..... 24
Figure 3.2: Angles and orientations of GLAD. ..... 25
Figure 3.3: Simple GLAD structures ..... 25
Figure 3.4: Increased range of GLAD structures ..... 26
Figure 3.5: SEM of $In_2O_3$:Sn coated glass ..... 28
Figure 3.6: AFM map of $In_2O_3$:Sn surface. ..... 28
Figure 3.7: Transmission of $In_2O_3$:Sn coated glass. ..... 29
Figure 3.8: Deposition chamber and vacuum system layout ..... 30
Figure 3.9: Cross-sectional SEM images of samples A through G ..... 32
Figure 3.10: Oblique SEM images of C through F ..... 33
Figure 3.11: SEM image showing anisotropy of growth ..... 33
Figure 3.12: Curvature of column growth ..... 34
Figure 3.13: Scattering of deposition flux by gas ..... 35
Figure 3.14: Bright field TEM images of samples B, D, and E. ..... 36
Figure 3.15: Diffuse diffraction pattern of sample D ..... 36
Figure 3.16: Optical bench set-up ..... 37
Figure 3.17: Transmission of titanium dioxide films. ..... 38
Figure 3.18: Absorption spectrum of Ru 535 bis-TBA ..... 39
Figure 3.19: Adsorbed dye calibration plot. ..... 41
Figure 3.20: Diagram of constructed devices ..... 43
Figure 3.21: Output spectrum of tungsten bulb ..... 43
Figure 3.22: Generation I: shor circuit current density vs. deposition angle. ..... 45

Figure 3.23: Current-voltage characteristic of the best performing generation I device..... 46
Figure 4.1: Cross-sectional SEM images of samples A-a through G-a..... 49
Figure 4.2: Definition of angles for cosine equation..... 50
Figure 4.3: Bright field TEM images of samples B-a, D-a, and E-a..... 51
Figure 4.4: Dark field TEM of annealed sample..... 52
Figure 4.5: XRD spectra of samples C and C-a..... 53
Figure 4.6: Transmission of annealed titanium dioxide films..... 54
Figure 4.7: Current-voltage characteristic of the best performing generation II device..... 57
Figure 4.8: Current-voltage characteristic of cells incorporating nanocrystalline particle layers..... 59
Figure 4.9: Comparison of spectra of standard AM 1.5 and tungsten bulb..... 61
Figure 4.10: Comparison of transmission spectra of as-delivered and annealed $In_2O_3$:Sn coated glass..... 62
Figure 4.11: XRD spectra of alternatively annealed samples..... 64
Figure 4.12: Bright field TEM images of alternatively annealed samples..... 65
Figure 4.13: Dark field TEM image of aggressively annealed sample..... 65
Figure 5.1: SEM images of as-delivered $SnO_2$:F coated glass..... 68
Figure 5.2: AFM map of $SnO_2$:F surface..... 68
Figure 5.3: SEM images of annealed $SnO_2$:F coated glass..... 69
Figure 5.4: Transmission of $SnO_2$:F coated glass..... 69
Figure 5.5: Cross-sectional SEM images of samples I-a through N-a..... 72
Figure 5.6: Cross-sectional SEM images of samples H and H-a..... 73
Figure 5.7: Top down SEM images of samples H-a through N-a..... 74
Figure 5.8: Bright field TEM images of sample L..... 75
Figure 5.9: Dark field TEM image of annealed sample..... 76
Figure 5.10: Optical transmission of as-deposited and annealed samples..... 77
Figure 5.11: Absorption spectra of Ru 620 H3TBA and Ru 535 TBA..... 78
Figure 5.12: Comparison of the output spectra of the tungsten bulb and projection lamp.. 80
Figure 5.13: Generation III: open circuit voltage vs. deposition angle..... 82
Figure 5.14: Generation III: short circuit current density on deposition angle..... 84
Figure 5.15: Generation III: device efficiency vs. deposition angle..... 85
Figure 5.16: Current-voltage characteristics of the best performing generation III device... 86
Figure 5.17: Diagram of electron paths..... 87

## List of Symbols and Abbreviations

| | |
|---|---|
| $\alpha$ | Flux incidence angle measured from the substrate normal. |
| $\beta$ | Column inclination angle measured from the substrate normal. |
| $\eta$ | Solar conversion efficiency. |
| $\varphi$ | Rotational position of substrate measured about an axis normal to the substrate and passing through its centre. |
| $\lambda_g$ | Absorption wavelength. |
| $\lambda_{mfp}$ | Mean free path of vapour species. |
| $\sigma$ | Absorption coefficient of the material. |
| $\frac{dM_r}{dA_r}$ | Mass deposited per differential area at a distance r from the source. |
| a | Column spacing. |
| A | Absorbance. |
| $A_{illum}$ | Area illuminated by solar radiation. |
| AFM | Atomic force microscope. |
| AM | Air mass. |
| CIGS | Copper, indium/gallium, sulfide. |
| $d_o$ | Molecular diameter. |
| $e^-$ | Electron. |
| $e^-_{counter}$ | Electron in counter electrode. |
| $e^-_{external}$ | Electron in external circuit. |
| $e^-_{TCO}$ | Electron in transparent conducting oxide. |
| $e^-_{TiO2}$ | Electron in titanium dioxide. |
| E | Electric field. |
| $E_{built\text{-}in}$ | Built-in electric field present in p-n junction. |
| $E_{CB\ TiO2}$ | Potential of titanium dioxide conduction band. |
| $E_{redox}$ | Redox potential of electrolyte. |
| FF | Fill factor. |
| GLAD | Glancing angle deposition. |
| $H^+$ | Proton. |
| HOMO | Highest occupied molecular orbital. |

| | |
|---|---|
| $i_{photo}$ | Photocurrent. |
| $i_{mp}$ | Current at maximum power point. |
| I | Electric current. |
| $I^-$ | Iodide ion. |
| $I_{2\ adsorbed}$ | Iodine molecule adsorbed to surface. |
| $I_3^-$ | Triiodide ion. |
| $I_{illum}$ | Illumination intensity. |
| $I_{sc}$ | Short circuit current. |
| IPCE | Incident photon-to-electron conversion efficiency. |
| J | Current density. |
| $J_{sc}$ | Short circuit current density. |
| K | Boltzmann's constant. |
| K $\alpha$ | X-ray produced by decay from the K shell to the L shell. |
| LUMO | Lowest unoccupied molecular orbital. |
| $M_e$ | Total mass evaporated from source surface element. |
| n | Refractive index. |
| O | Overlap integral value. |
| P | Power. |
| $P_{max}$ | Maximum power. |
| r | Distance from source element to substrate element. |
| R | Resistance. |
| $R_{sh}$ | Shunt resistance. |
| $R_s$ | Series resistance. |
| Ru 535 bis-TBA | *cis*-bis(isothiocyanato)bis(2,2'-bipyridyl-4,4'-dicarboxylato)-ruthenium(II) bis-tetrabutylammonium. |
| Ru 620 H3TBA | tris(isothiocyanato)-ruthenium(II)-2,2':6',2"-terpyridine-4,4',4"-tricarboxylic acid. |
| SEM | Scanning electron microscope. |
| T | Transmission. |
| TCO | Transparent conducting oxide. |
| TEM | Transmission electron microscope. |
| V | Voltage. |

| | |
|---|---|
| $V_{oc}$ | Open circuit voltage. |
| $V_{mp}$ | Voltage at maximum power point. |
| XRD | X-ray diffraction |

# 1. Chapter One: Introduction

## 1.1 History

The Sun: Man's first energy source. It provides energy to the plants and through them to the animals, both of which Man has consumed and used on his way to evolving into the pre-eminent lifeform on this planet. Since time immemorial, Man has dreamed of harnessing the Sun's power to do with as he pleased. From ancient Greece comes the legend of Phaeton, who tricks his father, the God Helios, into allowing him to drive the Chariot of the Sun. Like so many of Man's other attempts to harness the powers of nature, this adventure ended in disaster as Zeus was forced to strike down the chariot, killing Phaeton.

The beginning of Man's modern attempts to use the Sun's energy to produce a more useful form of energy began in 1839 with Becquerel's discovery of the photovoltaic effect in a liquid system [1]. When solutions of metal halide salts were illuminated, a current was observed to flow between two immersed platinum electrodes. His discovery that the ultimate energy source could be harvested has been pursued with vigor as it has the greatest potential to save Man from the other destructions he has wraught upon this world. The liquid based approach to energy conversion taken by Becquerel was later superceded by the development of solid-state devices.

Some of the first work in solar to electric, or photovoltaic, conversion with solid-state devices was done by Russel Ohl of Bell Laboratories. While examining purity issues and material properties of silicon, Ohl discovered that when silicon was recrystallized, "grown-in" junctions would form between regions of impurities. When heated or illuminated, one side of the junction would bias negative. Rudimentary photovoltaic cells, based on these "grown-in" junctions were constructed and first submitted for a patent by Ohl in 1941 [2]. This work was furthered by Chapin et al., who produced the first true solar cells in 1954 with efficiencies of over 6% [3].

The solid-state approach to photovoltaics taken by Ohl and Chapin experienced, and continues to enjoy, both a large research and a large commercialization effort. When the average person thinks of "solar cells" they are typically envisioning the solid-state type of

cell. These are the cells found on rooftops, in large arrays in arid areas, and at the top of many a calculator. They are efficient and they are successful. In recent years however, the chemical approach has experienced renewed interest.

This interest was sparked by the work of O'Regan and Gratzel. In 1991, they reported the first photovoltaic cell with a liquid component with a reasonable energy conversion efficiency [4]. It was made from dyes and tiny spheres that could be spread with a squeegee. Since the initial cell was reported, the dye sensitized approach to photovoltaics has been an area of intense research, with interest spanning material properties, device physics, and device improvement.

## 1.2 Motivation

This thesis presents the development of a dye sensitized solar cell based upon a highly porous material deposited by oblique deposition. A critical component of conventional dye sensitized solar cells is the porous network of wide band gap semiconductor materials that acts as the electron collector. This material is typically deposited either by screen or squeegee printing of particles in colloidal solutions. Although these techniques are both simple and inexpensive, they lack the ability to control the morphology of the films and are prone to device inconsistencies.

Oblique deposition, embodied here within the more advanced concepts of glancing angle deposition (GLAD), provides the ability to create highly porous materials with control over the structure on length scales less than 100 nm [5-7]. It offers an attractive alternative to the conventional methods used to deposit the electron collecting layer. The ability to tailor the GLAD structure presents the possibility of integrating light trapping elements into the electron collecting layer without sacrificing device performance. In addition, GLAD structures are typically significantly more open than the nanocrystalline particle network found in conventional dye sensitized solar cells. This increased accessibility of the electron collecting layer to the electrolyte may lead to improved performance. Finally, GLAD is easily applicable to a wide range of materials on a wide range of substrates, allowing easier variance of the material type than is possible with particle based approaches.

The goal of this work was to produce dye sensitized solar cell prototypes with performances comparable to conventional dye sensitized solar cells. Titanium dioxide was the material of choice for the electron collecting layer and all other components of the prototypes were similar to those reported in the literature. This was in order to isolate the effect of the obliquely deposited layer on device performance.

## 1.3 Scope

Chapter two presents the figures of merit commonly used in comparisons between photovoltaic cells and reviews the main approaches to fabrication. In particular, this chapter provides a detailed overview of the functioning of dye sensitized solar cells, in order that the reader may be more informed when examining the effects of the obliquely deposited layer.

Chapters three, four, and five present detailed characterizations and studies of the three successive generations of devices incorporating obliquely deposited layers. Chapter three details the initial efforts with as-deposited layers of varying parameters. In chapter four, these same structures, in an annealed form, are used as the electron collecting layers. Chapter five presents the third generation of solar cells, including many improvements over previous devices. From chapter to chapter, comparisons with previous generation devices and conventionally constructed cells are made and conclusions drawn on the source of device improvement.

Chapter six outlines the future work to be done in further developing and characterizing GLAD based dye sensitized solar cells.

# 2 Chapter Two: Solar Cells

A number of approaches have been pursued in the development of solar cells. The goal is to produce a device that converts sunlight into electricity with minimal loss at a very low cost. In order to compare between various types and approaches, common figures of merit must be used. These figures of merit will be examined and then the three major approaches to making solar cells will be discussed.

## 2.1 Figures of merit

Because the number of ways to compare solar cells is quite numerous, this section will present only some of the common ways. Ideally, a solar cell acts as an ideal current source, providing a stable current regardless of the load placed on it. The voltage produced should be only a function of the load placed on it, until the open circuit voltage is reached as shown by the ideal curve in Figure 2.1. In reality however, cells have internal energy dissipation mechanisms that decrease the performance from the ideal as shown by the real curve in Figure 2.1. The equivalent circuit diagram includes both a resistor in series with a current source and a resistor in parallel with both of them as shown in Figure 2.2. These resistances represent loss mechanisms within the cell that may vary as the circuit conditions change from short to open circuit.

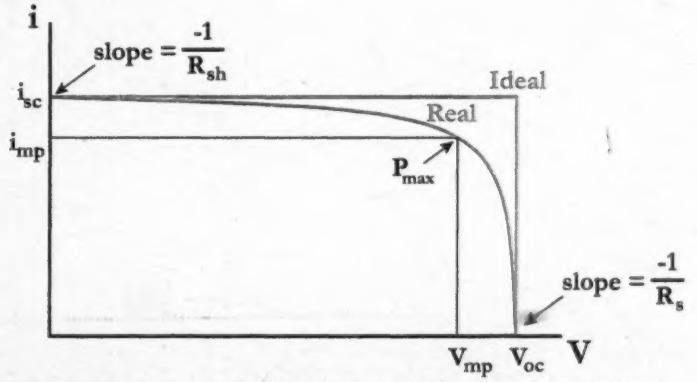


**Figure 2.1: Current-voltage characteristics of an ideal solar cell and a more realistic solar cell.**

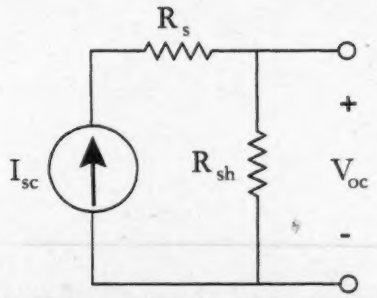


**Figure 2.2: Equivalent circuit with resistors representing internal energy dissipation mechanisms shown.**

The two major circuit parameters used in characterizing solar cells are the open circuit voltage and short circuit current density of the cell. The open circuit voltage is the voltage that develops between the two external contacts of the cell when no load is connected between them. This is the maximum voltage that the cell can provide. The short circuit current density, defined by equation 2.1a, is the current produced per unit area exposed to illumination when the two external contacts of the cell are connected directly together by a near zero impedance wire. This parameter provides a way of comparing the current producing capabilities of cells of differing size.

$$J_{sc} = \frac{i_{sc}}{A_{illum}} = \left.\frac{i}{A_{illum}}\right|_{load=0} \qquad \textbf{Eq. 2.1a}$$

Because the cells are not ideal, their current-voltage characteristics vary from the desired sharp curve. The fill factor is a measure of how much the cell's maximum power output is decreased from the ideal value. As shown in equation 2.1b, it is mathematically defined as the ratio of the maximum power (mp) produced by the cell over the product of the open circuit voltage and the short circuit current.

$$FF = \frac{P_{\max}}{i_{sc}V_{oc}} = \frac{i_{mp}V_{mp}}{i_{sc}V_{oc}} \qquad \textbf{Eq. 2.1b}$$

The most important characteristic of the cell is the conversion efficiency. This is the efficiency with which the cell converts impinging solar radiation to electricity. Simply, it is the ratio of the power output of the cell over the incoming power from the Sun. The efficiency results from the circuit parameters and characteristics of the cell and may be calculated using equation 2.1c. To maximize the efficiency for a given intensity and

illumination ($I_{illum}$), it is desirable to have high short circuit currents, high open circuit voltages, and near ideal performance evidenced by high fill factors.

$$\eta = \frac{P_{max}}{I_{illum} A_{illum}} = \frac{i_{mp} V_{mp}}{I_{illum} A_{illum}} = \frac{i_{sc} V_{oc} FF}{I_{illum} A_{illum}} \qquad \textbf{Eq. 2.1c}$$

A necessary condition for high efficiency is a high quantum yield, also known as the incident photon-to-electron conversion efficiency (IPCE). This is defined as the number of electrons provided to the external circuit for each incident photon. The majority of solar cells operate on principles that seek to have each incident photon provide one electron to the external circuit. Low values of quantum efficiency result in immediate losses of energy and thus, low efficiencies.

There are, of course, other bases on which to compare solar cells. Briefly, some of these are temporal stability, temperature stability, spectral stability, fragility, and cost, but these have not been standardized in a quantitative way. In this thesis therefore, the quantitative parameters will primarily be used for comparison.

It should finally be noted that most solar cells produce differing results under varying conditions of illumination. In order that the above parameters be comparable, they must be measured under the same conditions. There are three standards primarily used: AM 0, AM 1.0, and AM 1.5. These designations refer to a standard set of wavelengths and intensities. The "AM" stands for air mass, with the following number defining the distance of air the light must pass through relative to the distance it passes through at the equator. The two most commonly used standards are AM 0, which applies to those cells intended for use in space, and AM 1.5, which refers to the amount of illumination when the sun is 41.2° above the horizon. Standard test conditions for terrestrial solar cells are AM 1.5 illumination at 1000 $W/m^2$ (100 $mW/cm^2$) as is shown in Figure 2.3 [8].

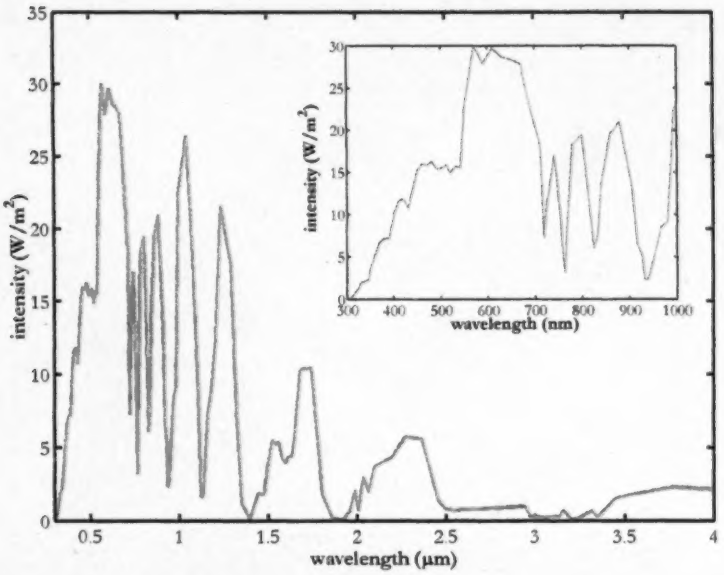


**Figure 2.3: Complete AM 1.5 spectrum with visible and near visible ranges displayed inset.**

## 2.2 Solid-state

Since Ohl's first patent application in 1941 [2], significant progress has been made in the optimization and production of solid-state solar cells. A number of different material systems have been examined thoroughly from both a technological and scientific point of view. The resulting technology is well understood and highly developed. The basic principles of operation, the further development of the technology, and the state-of-the-art performances will be presented.

### 2.2.1 Principles of operation

Solid-state solar cells are based around a p-n junction [9]. The p-n junction is the interface between two types of semiconductor materials: one, termed p-type, has excess electron acceptors, and the other, termed n-type, has excess electron donors. At equilibrium, the excess charges diffuse into the oppositely doped region, creating a space charge region whose resulting built-in electric field opposes further charge diffusion. When a photon with energy greater than the bandgap of the material is incident upon the material, there is a probability that it will be absorbed. The absorption of such a photon creates an electron-

hole pair by exciting the electron into the conduction band of the material. Because only electrons, not holes, are able to move freely in n-type material and vice versa, the electrons in the n-type material are able to be collected at the contact on the n-type side, but not the holes. Similarly, the holes in the p-type material are able to be collected at that contact, exclusive of the electrons. When an external connection is made between the contacts, current flows. Although the built-in electric field assists this motion, it is not the cause of it. This charge flow is known as the photocurrent. This process is illustrated in Figure 2.4.

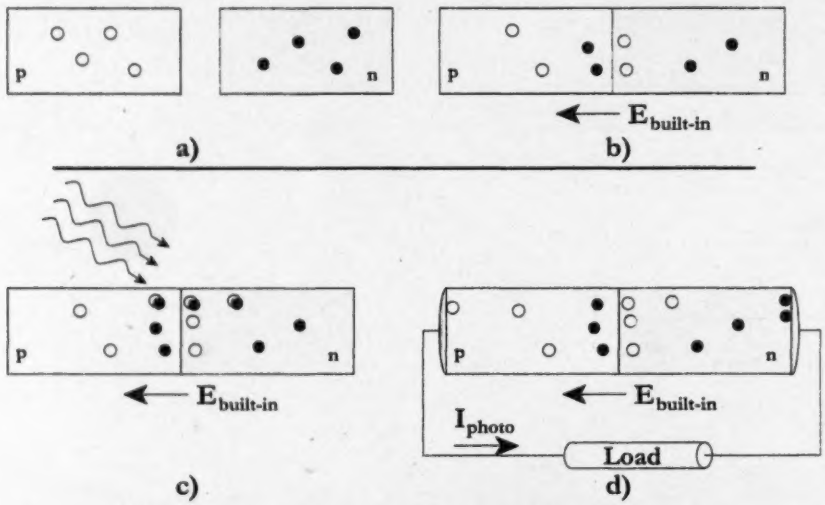


**Figure 2.4: Process of charge separation in a p-n junction. a) Isolated materials. b) Junction at equilibrium. c) Charge generation by illumination. d) Collection of charges at contacts.**

In the ideal device, each photon incident upon the material generates an electron-hole pair, with energy equal to the incident photon, that is collected at the contact. In reality however, there are a number of loss processes that contribute to energy conversion efficiencies that are significantly less than 100%. The first of these processes is the reflection of incoming photons at the front surface of the device, due to the index mismatch of the device with the surrounding air [10]. The next loss process is the incomplete absorption of incident light. Particularly in thin devices at high intensities, a significant portion of the incident light may escape the cell and be lost after one or two passes through the cell. The amount of loss to this process may be calculated using the absorption coefficient of the material. Although both of the previous loss processes may be minimized through proper design, the nature of photon absorption in semiconductors must be dealt with on a material level. For a photon

to be absorbed, it must have energy greater than the bandgap of the semiconductor. Of the standard photovoltaic materials, silicon has the lowest bandgap of 1.1 eV ($\lambda_g$ = 1129 nm). This results in a large part of the solar spectrum being absorbed, but not all. Although it might seem that choosing a material with a small bandgap would maximize the efficiency of the solar cell, the loss due to thermalization of carriers causes the efficiency versus bandgap curve to have a maximum at an intermediate bandgap value [11]. When a photon with energy greater than the bandgap is absorbed, it generates an electron-hole pair with corresponding energy. This high-energy pair quickly loses its energy in excess of the bandgap. A photon with energy just above the bandgap thus produces an electron-hole pair with the same effective energy as a photon with energy much greater than the bandgap. This process alone was calculated to limit the conversion efficiency of silicon solar cells to 44% [12]. Once carriers are generated, they must be collected at the contacts to be of use. Recombination of carriers at defects within the material and at the contacts reduces the overall photocurrent [13]. This loss process may be reduced by minimizing the distance carriers must travel to the contacts and by using high purity materials with low defect concentrations, however radiative recombination will still occur. In modern solar cells, these recombination processes have been minimized to the point where quantum efficiencies of 80-90% are common. It is radiative recombination and the two bandgap considerations that ultimately limit the overall conversion efficiency of an otherwise idealized cell.

In 1961, Shockley and Queisser wrote a paper that defined the "Holy Grail" of photovoltaics [14]. Using radiative recombination processes, photon absorption, and carrier thermalization as their ultimate limits, and black body radiation as the framework of their calculations, they calculated the ultimate efficiency limit for a single junction p-n device to be 31%. This is the efficiency that most strive for and towards which significant progress has been made.

### 2.2.2 Technological developments

As the loss processes of solid-state solar cells have been identified, researchers have created solutions that minimize or eliminate these losses. These solutions will be discussed in the order that the loss processes were previously identified.

The first loss process is the reflection of incoming light. This problem is common to both the optics and photovoltaic industries. The solution that has been implemented is the application of anti-reflection coatings. These coatings consist of materials that are transparent to the radiation of interest and have indices of refraction that are intermediate between the air, normally $n_{air} = 1$, and the top material of the solar cells. As shown by equation 2.2a, the transmission increases as the difference in refractive indices decreases [15]. The optimal value of the refractive index of the anti-reflection coating depends on the material of the device. One example, for a silicon device, is shown in Figure 2.5. The intermediate layer succeeds in increasing the transmission because of the dependence on the difference between the refractive indices at each interface. Note that as the index of the intermediate layer approaches that of either medium, the transmission approaches the value obtained without any anti-reflection coating. The materials of choice have been titanium dioxide and silicon nitride [16]. Often these coatings consist of multiple layers of increasing index or a single layer with a graded index change [17, 18]. The overall effect is to couple more light into the solar cell, thus increasing the input energy that may be converted.

$$T = 1 - \left| \frac{n_1 - n_2}{n_1 + n_2} \right|^2 \qquad \text{for normally incident light} \qquad \textbf{Eq. 2.2a}$$

$$T = T_1 T_2 \qquad \text{for non-absorbing materials} \qquad \textbf{Eq. 2.2b}$$

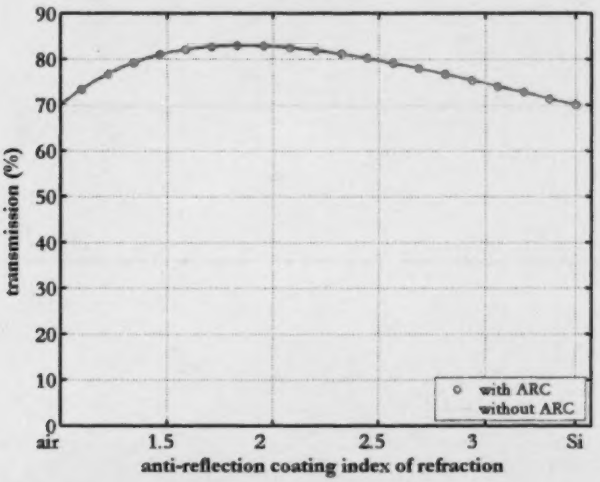


**Figure 2.5: Effect of anti-reflection coating index of refraction on total transmission into underlayer.**

Two solutions have been implemented for increasing the absorption of light in devices. The only way to increase the absorption in a given material is to increase the distance that the light travels through it. The most obvious way of doing this is to increase the physical thickness of the device. However, this approach has two large drawbacks. First of all, increased device thickness means that more material must be used in the construction of the device. Material of sufficient purity for solar cells is expensive and, in fact, constitutes a significant portion of the final cost [11]. Increasing the physical thickness thus increases the cost. Worse yet, the increased thickness does not provide as significant an improvement as one first estimates. As carriers are generated throughout the device, the increased thickness means that some carriers will be generated further from the contacts. This leads to increased recombination probabilities and a smaller than predicted increase in efficiency [19]. A second approach to improving the absorption has been to trap the light within the material. Many different and novel techniques [20, 21] have been explored, but the most commonly implemented solution is texturing of the top surface, with the bottom surface being reflective or also textured [22, 23]. By having either regularly or randomly distributed faces, light reflected from the back surface is retained through total internal reflection as shown in Figure 2.6. This increases the effective optical path length seen by incident light [24], and thus increases the amount of light that may be absorbed within a given physical thickness.

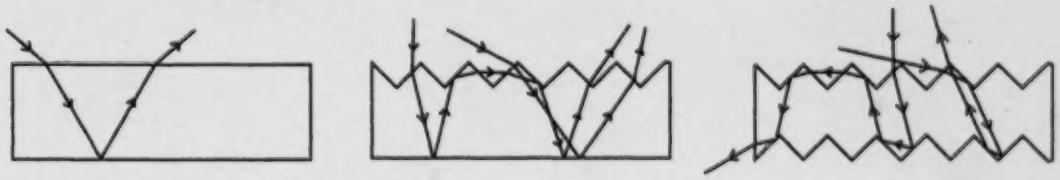


**Figure 2.6: Effect of simple light trapping structures on optical path length in material. a) No texturing with reflective back side. b) Front side texturing with reflective back side. c) Front and back side texturing.**

Although the bandgap considerations are intrinsic to the material being used, designs exist which succeed in partially circumventing the loss. As shown in Table 2.1, the family of commonly used photovoltaic materials, such as silicon in its various forms, gallium arsenide, cadmium telluride, and copper indium diselenide/copper gallium diselenide/copper indium disulfide (CIGS), has a wide window of bandgaps. Each specific bandgap has a maximum

efficiency associated with it, but when combined, the total efficiency of a cell may be increased [25]. The concept, as illustrated in Figure 2.7, is to combine two or more junctions of differing bandgaps. The high bandgap junction is placed first, with the low bandgap cell being placed behind. The high bandgap junction absorbs only the high energy photons, passing the low energy photons on to the second junction. This minimizes the carrier thermalization loss of the second junction, while avoiding the loss of all photons below the bandgap of the first junction. Additional junctions with appropriate bandgaps may be added to further increase the efficiency. Utilizing a similar approach to Shockley and Queisser, efficiency limits have been calculated of 42.7% for a two junction tandem cell and 49.1% for a three junction tandem cell [26]. A variation on this approach is to use a single cell with a graded bandgap in an attempt to eliminate thermalization loss all together [27]. This is most easily accomplished with CIGS cells as the bandgap may be engineered through the composition.

**Table 2.1**

| Material | Bandgap (eV) |
|---|---|
| Crystalline silicon | 1.12 |
| Hydrogenated amorphous silicon | 1.86-1.94 |
| Gallium arsenide | 1.42 |
| Cadmium telluride | 1.56 |
| CIGS | 2.9 |

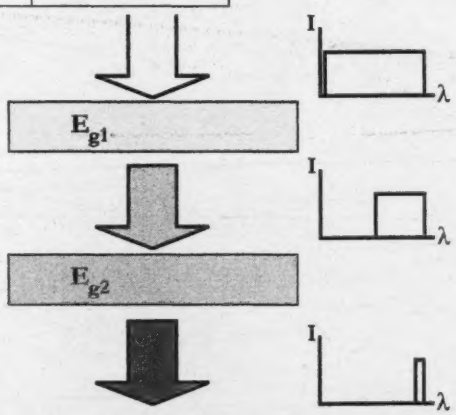


**Figure 2.7: Functioning of a tandem cell. Photons with energy above the bandgap of the first junction are absorbed and converted to electricity, while photons with energy below the bandgap of the first junction pass through to the second junction.**

Three main routes, almost always pursued in parallel, have been taken to minimize the recombination losses in solar cells. In order to avoid bulk recombination losses, high purity materials have been used. Although not of the same purity as those used for microelectronics processing, the increased cost of the material is still significant [11]. It has also been found that surfaces act as recombination centres. Thus, just as the carriers reach the surface and need only travel along the surface to a contact, they have one last, large chance of recombining. To avoid this, the surfaces are typically passivated with a thin layer of oxide or nitride everywhere except where the contact is to be made [28]. The third method is an optimized contact system. In order that the majority of carriers be collected, it is desired that the contacts be as accessible to the carriers as possible. To minimize the distance carriers must travel along the surface, it would be advantageous to have the entire surface covered by the contact. However, highly conductive contacts are, by nature, metallic and thus reflect solar wavelengths. This results in reduced incident light over a given cell area. A trade-off must be made between these two opposing considerations. The usual design is patterned metallic fingers stretching across the face of the cell with varying surface coverages [29]. In order to make the contacts more accessible to the entire surface of the cell, the surfaces are often heavily doped to increase the appropriate carrier mobility.

### 2.2.3 Maximum efficiencies

Because solid-state solar cells are such a mature technology, all of the above technological developments have been well researched and implemented into both experimental and production cells. The improvement in efficiency has typically been a matter of slow increases until one or more of the above developments were implemented, at which point jumps occurred [19].

The most efficient single junction solar cell that has been confirmed by standardized, outside measurements thus far is made by Kopin and is based on gallium arsenide, with an aluminum gallium arsenide window [30]. It has an open circuit voltage of 1.022 V, a short circuit current density of 28.2 $mA/cm^2$, and a fill factor of 87.1%, resulting in a conversion efficiency of 25.1%. Although no details of the actual cell structure are available, the next most efficient cell incorporates all of the features discussed previously [31]. Table 2.2 lists a number of the most efficient single junction cells and their performance parameters.

Table 2.2

| Material | Efficiency (%) | $V_{oc}$ (V) | $J_{sc}$ (mA/cm$^2$) | FF (%) |
|---|---|---|---|---|
| Silicon (crystalline) [31] | 24.7 ± 0.5 | 0.706 | 42.2 | 82.8 |
| Gallium arsenide | 25.1 ± 0.8 | 1.022 | 28.2 | 87.1 |
| CIGS [32] | 18.4 ± 0.5 | 0.669 | 35.7 | 77.0 |

The most efficient cell tested to date is a dual junction tandem cell made by Japan Energy [33]. This cell has a gallium indium phosphide junction stacked with a gallium arsenide junction. These two junctions in series provide an overall efficiency of 30.3%, an open circuit voltage of 2.488 V, a short circuit current density of 14.22 mA/cm$^2$, and a fill factor of 85.6%.

Great progress has been made in developing solid-state solar cells with high efficiencies. The main drawback to these types of cells is in their cost. Although some semiconductor materials are less expensive than others, they remain comparatively expensive and difficult to process.

## 2.3 Organic

The use of organic materials for solar cells was inspired by the first solar cell ever created: the photosynthetic mechanism in plants. Because of the tailorability of the structure of organic molecules, their spectral absorption is easily changed. This capability has led to a great deal of experimentation with different organic molecules in different configurations. This section presents the principles of operation, along with the challenges faced by organic solar cells, and the most efficient organic cell so far reported.

### 2.3.1 Principles of operation

Organic solar cells operate in a manner different from solid-state cells. The presence of a junction within the organic material is optional, although it does lead to better performance, and carrier separation is not immediate. When a photon is absorbed by an organic molecule, it produces a strongly bound exciton. This is usually in the form of an electron in an excited state, but still within the orbitals of the molecule. The dissociation of excitons requires a strong driving force that is provided either by the difference in work functions of the contact materials of a homojunction, or the difference in electron affinity and ionization potential in

heterojunction devices [34]. In homojunction devices, exciton dissociation occurs only at a contact, requiring that the exciton reach the contact by diffusion. Because exciton diffusion lengths are typically 1-10 nm, this requires very thin absorbing layers [34]. Although absorption coefficients of organic molecules are high, this still results in incomplete absorption, particularly in the red end of the spectrum, where organic absorption is weakest.

Dispersed heterojunction devices somewhat alleviate this problem. These devices consist of two materials blended together. Exciton dissociation occurs at the interface between the two materials, eliminating the need for the exciton to diffuse over long distances. Electron transport then occurs by hopping through localized states to the anode. This motion is assisted by the electric field produced by the difference in work functions of the contact materials. Dispersed heterojunction devices improved the quantum efficiency of organic devices to 29% [35] from values less than 1% for homojunction devices.

Despite years of research, the poor spectral match with the solar spectrum, comparatively poor charge transport, limited quantum efficiencies, and lack of environmental stability have prevented any organic devices from going into large scale production.

### 2.3.2 Maximum efficiencies

The most efficient organic solar cell produced so far is based on a doped pentacene heterojunction [36]. It has a conversion efficiency of 4.5%, an open circuit voltage of 0.90 V, a short circuit current density of 7.7 $mA/cm^2$, and a fill factor of 66%.

## 2.4 Dye sensitized

The greatest breakthrough in solar cells in recent years is the dye sensitized solar cell. First reported by O'Regan and Gratzel in 1991 [4], these cells represent a hybrid between organic and inorganic solar cells. The structure and principles of operation of these cells will be discussed in detail, along with their level of development and the most efficient cells reported thus far.

### 2.4.1 Principles of operation

The dye sensitized solar cell borrows heavily from both the photosynthetic structure found in plants and technology originally developed for photography. As in plants, the light absorption and carrier transport functions in dye sensitized solar cells have been isolated and occur in different materials. This has been accomplished through a dye sensitization process analogous to that used in photography. The electron transport material is chosen to be a wide bandgap semiconductor that absorbs only in the ultraviolet range. Contribution to the overall photocurrent from this absorption is minimal. The majority of the photocurrent is due to electrons injected from the dye, which absorbs throughout the visible range.

The structure and electronic processes present in a conventional dye sensitized solar cell are illustrated in Figure 2.8. Conventional cells consist of a transparent conducting oxide (TCO) coated glass substrate further coated by a titanium dioxide layer composed of nanocrystalline particles 5 to 50 nm in diameter. These particles are interconnected in a random way with each other, and finally to the substrate. These particles are sensitized by a monolayer of ruthenium based, light absorbing dye adsorbed on their surfaces. A redox electrolyte, typically containing the iodide/triiodide pair, is allowed to penetrate throughout the titanium dioxide particle network and is brought in contact with a counter electrode coated with a catalytic material such as platinum or graphite [37].

Photons incident upon the cell pass through the TCO coated glass and are absorbed by the dye molecules. When absorbed, the photons cause an electron to enter an excited state, similar to the process in organic solar cells. The dye is chosen such that its lowest unoccupied molecular orbital (LUMO) is slightly above the conduction band of the titanium dioxide. The electron is rapidly injected into the titanium dioxide conduction band, leaving behind a positively charge dye molecule. The dye is reduced by iodide in the redox solution, while the electron percolates through the titanium dioxide layer to the underlying electrode, where it is made available to do work in the external circuit. An electron at the counter electrode reduces triiodide to iodide, completing the regeneration of the cell. The overall process can be described as below.

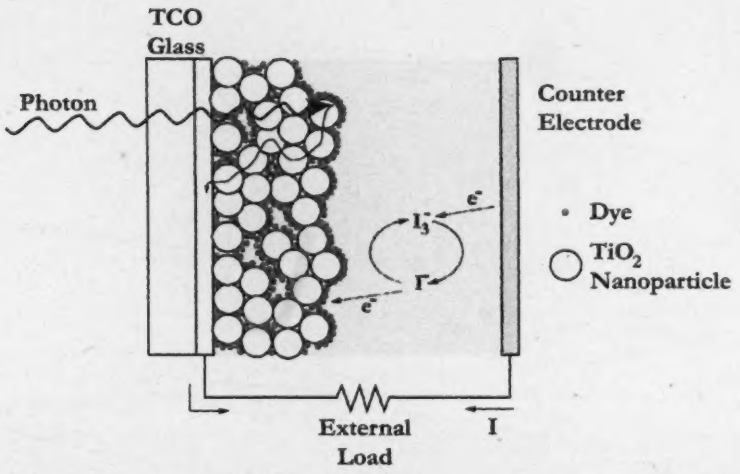


**Figure 2.8: Basic construction and operation of a dye sensitized solar cell. Photon absorption by the dye causes the injection of an electron into the titanium dioxide network. The electron percolates through the network to the underlying contact, where it is made available to do work in the external circuit. The electrolyte reduces the dye and is, in turn, reduced at the counter electrode.**

$$Dye \xrightarrow{photon} Dye^*$$

$$Dye^* \longrightarrow Dye^+ + e^-_{TiO_2}$$

$$2Dye^+ + 3I^- \longrightarrow 2Dye + I_3^-$$

$$e^-_{TiO_2} \xrightarrow{percolation} e^-_{TCO} \longrightarrow e^-_{external} \longrightarrow e^-_{counter}$$

$$I_3^- + 2e^-_{counter} \longrightarrow 3I^-$$

In the last decade, dye sensitized solar cells have been an extremely active area of research. Although controversies still remain regarding the exact mechanisms of some processes, consensus has been reached on the majority of issues. A more detailed look will now be taken at the mechanisms within the cell.

2.4.1.1 Electron injection

Although the proximity of the excited dye molecules to the titanium dioxide particles is essential for the separation of electrons from the dye, it is not sufficient to cause the injection of the excited electrons. Instead, it is believed that the driving force for electron injection is ion adsorption on the titanium dioxide surface. When binding to the surface, the

acidic dyes release hydrogen ions that become incorporated into the region of the surface near the dye. The presence of these hydrogen ions in the surface region, along with the dye molecules near the surface and electrolyte anions attracted by the hydrogen ions form a Helmholtz layer [38], depicted in Figure 2.9, across which there is an electrical potential drop of ~0.3 eV. It is this electric field that provides the major driving force for electron injection. As stated previously, the dye molecule's LUMO is slightly above the conduction band of the titanium dioxide. Electron injection thus also has an enthalpic driving force behind it. Similarly, the highest occupied molecular orbital (HOMO) of the dye is above the redox potential of the electrolyte, providing incentive for dye oxidation by the electrolyte. In addition to the electrical and enthalpic driving forces, there is a much higher density of states in the titanium dioxide conduction band than there is in the dye molecule's orbitals, providing a small entropic inducement for charge injection. These three factors result in ultrafast electron injection into the titanium dioxide. A number of groups have attempted to measure the injection rate and have found that it occurs on subpicosecond timescales less than 25 fs [39, 40]. This high injection speed is one of the key factors in avoiding recombination losses.

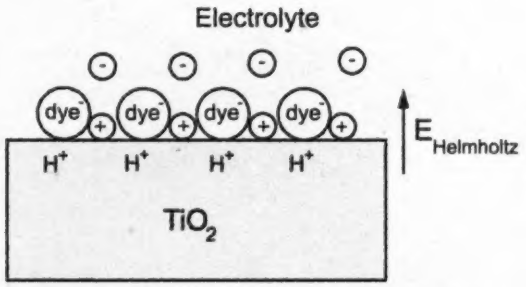


**Figure 2.9: Helmholtz layer causing electron injection.**

2.4.1.2 Charge transport

Since the titanium dioxide particles form such a porous and irregular network, it may be surprising that electrons are transported so efficiently to the underlying electrode. The small size of the individual particles prevents the formation of an electric field in the particles [41] and the screening provided by the electrolyte prevents the build up of an electric field across the thickness of the film [42]. The electron transport is believed to occur by hopping of the electrons via surface traps [43]. On average, it is estimated that there is one electron present in a titanium dioxide particle at a time [44]. These electrons are screened by anions within

the electrolyte and hydrogen ions in the surface regions of the titanium dioxide particles. Movement of the electrons through the titanium dioxide appears to occur by simple diffusion and it takes approximately 10 ms to traverse the layer. This time may vary based on the nature of the traps through which the electron passes. If it happens to pass through several deep traps, the transit time will be much longer. The higher density of states in the conducting oxide acts as a sink for the electrons generated in the dye/titanium dioxide layer.

To complete the regeneration of the cell, the electrolyte in appropriate forms must be present at both the titanium dioxide/dye interface and at the counter electrode. The transport between the two locations also appears to be diffusion driven. Depending upon experimental conditions, either this diffusion or the electron transport in the titanium dioxide can be the limiting factor in charge transport.

2.4.1.3 Origin of the photovoltage

The development of the photovoltage in a dye sensitized solar cell is a result of the conduction band position of the titanium dioxide and the redox potential of the electrolyte [45]. Under illumination, the Fermi level in the titanium dioxide shifts up towards the conduction band edge. Because of the high density of states, the Fermi level can shift no higher than the lower edge of the conduction band. This is the maximum potential present in the cell. At the counter electrode, the catalytic material maintains the redox potential of the electrolyte at its equilibrium value. The maximum photovoltage that may be obtained from the cell is thus the difference between the conduction band edge and the redox potential of the dye [46]. The relative positions of the various energy levels within the cell are shown in Figure 2.10.

$$V_{oc} = E_{CB_{TiO2}} - E_{redox} \quad \textbf{Eq. 2.4a}$$

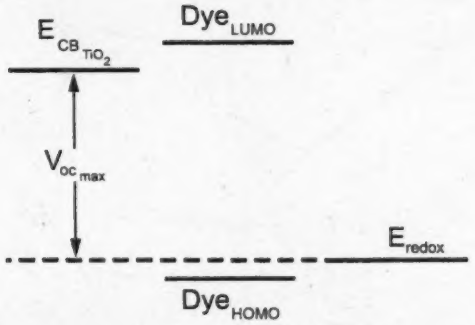


**Figure 2.10: Relative energy levels present within the dye sensitized solar cell.**

2.4.1.4 Recombination mechanisms

$$e^-_{TiO_2} + Dye^+ \longrightarrow Dye$$

$$2e^-_{TiO_2} + I_3^- \longrightarrow 3I^-$$

There are a number of paths by which the electrons injected into the titanium dioxide may follow to avoid being collected at the contact. The degree to which recombination occurs is due primarily to the reaction kinetics that are present. The first potential recombination mechanism is the recapture of an injected electron by a positive dye molecule. This mechanism has been extensively studied and is found to progress in microseconds to milliseconds at short circuit, a comparatively slow speed [47, 48]. This loss mechanism increases however, as the cell approaches open circuit. Another loss mechanism is the recombination of injected electrons with the electrolyte. This may occur when the electron is in two locations: in the titanium dioxide or in the conducting oxide electrode. The probability of this recombination appears to be very high due to the extremely high exposed surface area of the titanium dioxide and the high concentration of electrons in the conducting oxide. Fortunately, both of these reactions occur with very slow kinetics. It has been proposed that this reaction actually occurs in three steps, outlined below the text [49]. In the first step, a triiodide ion dissociates into an iodine molecule and an iodide ion. If the iodine happens to adsorb to the titanium dioxide or conducting oxide, it may recombine with an injected electron to form an $I_2^-$ ion. The subsequent dismutation of two $I_2^-$ ions into an iodide ion and a triiodide ion completes the recombination process. Both the second step and the third step are believed to occur very slowly. Because the concentration of adsorbed iodine is low compared to the iodide ion concentration, the reduction of the oxidized dye by

the iodide is the more probable reaction, occurring in approximately 10 ns [50]. The final step is the rate-limiting step due to the extremely low concentrations of the reactants. The overall time required for the reactions has been found to be hundreds of milliseconds to seconds.

$$I_3^- \xrightarrow{dissociates} I_2 + I^-$$
$$I_{2_{adsorbed}} + e^-_{TiO_2} \longrightarrow I_2^-$$
$$2I_2^- \longrightarrow I^- + I_3^-$$

### 2.4.2 Level of development

The dye sensitized solar cell as first reported by O'Regan and Gratzel was already in a high state of development. The titanium dioxide network was the innovation that pushed the efficiency into a range comparable with solid-state cells. The dye had been tailored to absorb efficiently over the majority of the solar spectrum and the electrolyte chosen to efficiently reduce the oxidized dye.

A great deal of work to improve the performance of cells has centered around modifying or replacing the adsorbed dye with other dye complexes [51-54]. This avenue of research yielded no major results until a new dye was developed, again by Gratzel [55]. The new "black" dye is discussed further in Chapter 5. One method to improve the absorption across the entire solar spectrum is the use of multiple dyes in a way analogous to multiple junctions in tandem solid-state cells. The effects of the dyes were found to be additive in producing photocurrent, although careful selection is required to ensure the adsorption of the second dye monolayer [56].

Work has also been done varying the material that comprises the porous network. Various oxides with wide bandgaps were used, but titanium dioxide proved to be the optimal choice [57, 58]. Various methods of depositing the titanium dioxide layer have also been attempted in order to be able to use current microprocessing techniques and improve control over the microstructure. Although methods such as sputtering [59, 60], spray pyrolysis [61], and sol-gel deposition [62] have produced comparable results, none have exceeded the bar set by screen printed nanocrystalline particles.

A number of methods have been attempted to modify the dye/titanium dioxide complex in order to improve cell performance [63-66]. The majority of these have focused on decreasing recombination at the titanium dioxide/electrolyte interface. One of the most successful methods found is the treatment of the dye/titanium dioxide complex with 4-*tert*-butylpyridine [49]. Treatment with this chemical is speculated to prevent adsorption of iodine to the titanium dioxide surface, thus significantly reducing the rate of recombination of titanium dioxide conduction band electrons with the electrolyte. This leads to increased open circuit voltages and a significant increase in efficiency. Another method of modification is ultraviolet exposure. It has been shown that a short UV illumination provides a small increase in photocurrent and a small decrease in open circuit voltage, with a net increase in efficiency, for optimized dyes [67]. This effect is maintained so long as the cell remains assembled. It has been hypothesized that the UV exposure causes the conduction band edge of titanium dioxide to move, resulting in a greater driving force for electron injection.

The largest drawback of the dye sensitized solar cell is the liquid electrolyte. Since the iodide/triiodide pair is dissolved in a volatile solvent, stable long term performance requires the cells to be hermetically sealed. This presents fabrication challenges and various groups have attempted to replace the liquid electrolyte with a non-volatile solid charge transport medium [68-70]. These attempts have met with limited success as the solid charge transport mediums often lack the ability to screen the injected electrons. Hopefully new materials will be developed to meet the challenges.

Although the chemical and material systems have been somewhat optimized to provide maximum performance, dye sensitized solar cells have not yet taken advantage of the technology developed for solid-state solar cells. Innovations that have direct application to dye sensitized solar cells include anti-reflection coatings and light trapping structures. Anti-reflection coatings are not as critical for dye sensitized solar cells as they are for solid-state cells because the index of the TCO coated glass is a much closer index match to air than the semiconductor materials of solar cells. Light trapping structures are thought to be less important for dye sensitized cells as well because the titanium dioxide layer scatters incoming

light. However, as solid-state cells have demonstrated, every small increase in efficiency is worth pursuing. One development that has a significant amount to offer to dye sensitized solar cells is improved electrode design. At present, the contact to the titanium dioxide is made using glass coated with a transparent conducting oxide. This is sufficient to make contact, however it possesses a relatively high resistance per square. The patterned metallic fingers commonly used in solid-state cells cannot be used due to the corrosive nature of the electrolyte [65]. Only compounds or inert metals are able to withstand the corrosion for long periods of time. In addition to the high cost of using inert metals as the contact, care must be taken not to introduce a surface that may act as a catalyst to electron/electrolyte recombination. With additional processing, there are a number of possibilities one might imagine for making improved contact.

### 2.4.3 Maximum efficiencies

The highest reported efficiency for a dye sensitized solar is 10.4%. This cell incorporated the "black" dye and was treated with butyl pyridine before assembly [71]. This value has not been confirmed by external tests. The highest efficiency confirmed by external tests is 8.2%, with an open circuit voltage of 0.726 V, a short circuit current density of 15.8 $mA/cm^2$, and a fill factor of 71.2% [72].

# 3 Chapter Three: Generation I Devices: As-deposited Films

This chapter discusses the development of the first generation of dye sensitized solar cells with electron collecting layers fabricated using the Glancing Angle Deposition (GLAD) technique. A brief overview of the GLAD technique will be given, the main components of the solar cell will be examined individually, the details of the cell assembly will be given, and finally performances of the cells will be examined.

## 3.1 Glancing Angle Deposition

Glancing Angle Deposition, or GLAD, is a technique developed at the University of Alberta by Robbie and Brett [5, 73]. Based on physical vapour deposition, GLAD utilizes computer controlled substrate motion and relies on limited adatom diffusion and shadowing of collimated flux at oblique incidence angles to fabricate porous microstructured films with a high degree of control over the film structure. Typically performed at flux incidence angles greater than 80°, extreme shadowing of incoming flux by previously deposited material, as shown in Figure 3.1, causes voiding in the deposited film. This voiding results in isolated columns of material that are inclined towards the incoming flux. The column angle and film porosity produced in this way are characteristic of the angle at which the film was deposited. When the angle of flux incidence is changed, the shadowing conditions are perturbed, resulting in a change in the porosity of the film and a change in the angle of the column. Well known at lower flux incidence angles, this effect has been quantified by the tangent rule [74]. At angles great than 60°, this effect is more properly described using the geometrically derived Tait's rules given by equations 3.1a and b [75].

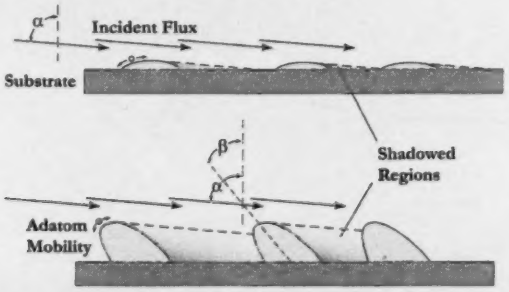


**Figure 3.1: Critical phenomena affecting GLAD: Shadowing and limited adatom mobility.**

$$\beta = \alpha - \sin^{-1}\left(\frac{1-\cos\alpha}{2}\right) \qquad \text{Eq. 3.1a}$$

$$a = \frac{1}{2}\left[1 + \frac{1}{\cos\alpha}\right] \qquad \text{Eq. 3.1b}$$

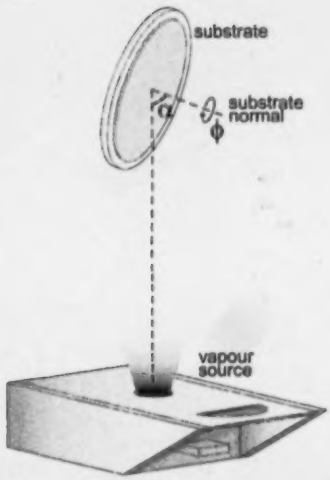


**Figure 3.2: Illustration of the angles and orientations controlled in the GLAD process.**

When the substrate is rotated about the axis normal to its surface and passing through its centre, shown in Figure 3.2, the columns follow the apparent motion of the source. At relatively low substrate rotation speeds with respect to the deposition rate, this results in corkscrew structures usually termed helices [76]. With faster substrate rotation, the vertical distance between each turn of the corkscrews decreases until, at very high rotation rates, the individual turns become indiscernible and the structure is more properly described as vertical posts [77]. The column angle in this case is 0° because the flux is effectively incident from all sides. This progression of structure with increasing rotation rate is pictured in Figure 3.3.

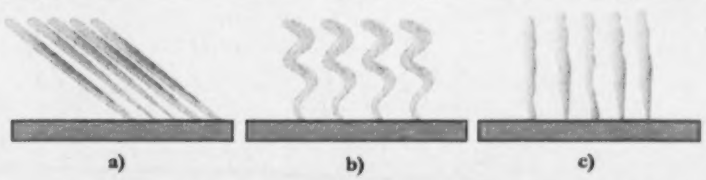


**Figure 3.3: Structure obtainable with continuous rotation. a) Slanted columns- no rotation. b) Corkscrews- slow rotation. c) Vertical posts- fast rotation.**

Continuous motion permits the fabrication of only these two simple types of microstructures, whereas discontinuous substrate rotation allows the formation of a variety of different film structures, including chevrons, polygonal spirals, twisted ribbons, and variable pitch helices. Advanced rotation algorithms also permit the separation of the column angle and film porosity parameters, leading to a greatly enlarged range of film structures that may be fabricated [78]. Without advanced rotation, the column angle is confined to the line representing Tait's rule in Figure 3.4. Advanced motion permits structures anywhere within the shaded region to be created.

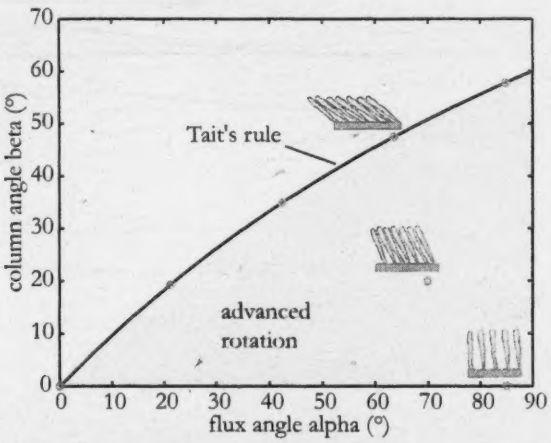


**Figure 3.4: Advanced rotation permits the fabrication of a greatly increase range of structures, whose column angle and porosity parameters have been decoupled.**

Utilizing both substrate rotation and variance of the deposition angle, the porosity of the film may be evolved from dense to porous and back again to dense. This has proven useful in a number of applications, where "capping" of porous regions, dense adhesion layers, or films of varying porosity are required [79].

The nature of this technique allows the fabrication of these films from nearly any material on any substrate able to withstand the temperatures of the deposition process. The most commonly used deposition materials are metals, oxides, and other simple compounds. Films have been deposited on silicon, glass, and polymer substrates [80]. Thus far, GLAD has been applied to the physical vapour deposition techniques of evaporation, sputtering [81], and pulsed laser deposition [82].

Precise control over the structure is achieved using feedback from a quartz crystal oscillator placed normal to the incoming flux, near the substrate. This rate information is modified by a ratio accounting for the difference in vertical growth on the substrate as compared to that on the quartz crystal. Signals from this monitor are fed back to a computer program that controls the motors' motions based on mathematical descriptions of the structure.

Due to the relatively recent development of the technique, work is ongoing in modeling [83] and characterizing both the basic growth process of GLAD films [84-86] and a wide variety of material properties [87-89].

The unique ability to create highly porous films with controlled structure on such a small scale has made the GLAD technique useful in a variety of applications. GLAD films have been developed for applications ranging from liquid crystal alignment [90], optical filters [91], diffraction gratings [92], anti-reflection coatings [93], photonic crystals [94], thermal barrier coatings [95], field emission structures [96], and humidity sensors [97, 98], to catalytic surfaces [99, 100].

## 3.2 Transparent conductive oxide substrate

For the initial attempt at fabricating dye sensitized solar cells, the substrates chosen were glass coated with tin doped indium oxide ($In_2O_3$:Sn). This is the most common transparent conducting oxide and is widely used in cathode ray tubes, liquid crystal displays, and vehicle window defrosters. The particular substrates used in this experiment were 2.5 cm x 2.5 cm pieces of 1.1 mm thick $In_2O_3$:Sn coated glass provided by Philips Research Laboratories. Examination with a scanning electron microscope (SEM), revealed that the $In_2O_3$:Sn layer consisted of a 3 μm layer of indium oxide doped with tin for a conductive layer depth of 135 nm, shown in Figure 3.5 a). The surface revealed by the SEM in Figure 3.5 b) consisted of plateaus separated by sharp edges. Using a Digital Instruments Dimension 3100 atomic force microscope (AFM), this topography was found to have finer structure on the plateaus, as shown in Figure 3.6, and produced an overall rms surface roughness of 4.0 nm. The visible transmission of the substrate was measured using a Perkin Elmer Lambda 900 double beam spectrophotometer equipped with PELA 1003 general purpose optics bench and

integrating sphere with a baseline taken with air. The $In_2O_3$:Sn coated glass exhibited greater than 80% transmission for all wavelengths above 435 nm, decreasing to the reasonably high value of 66% at 350 nm. Using equations 2.2a and 2.2b and assuming a two layer stack of materials with the typical indices of refraction of 1.95 and 1.5 for the $In_2O_3$:Sn and glass respectively, the transmission of the $In_2O_3$:Sn coated glass may be calculated to be near 84.6% in the visible region. This is in good agreement with the measurement, given that indices will change depending upon the exact composition of the $In_2O_3$:Sn and the glass as well as varying with wavelength. Measured using a four point probe, the sheet resistance of the $In_2O_3$:Sn coated glass was found to be 10.3 Ω/sq.

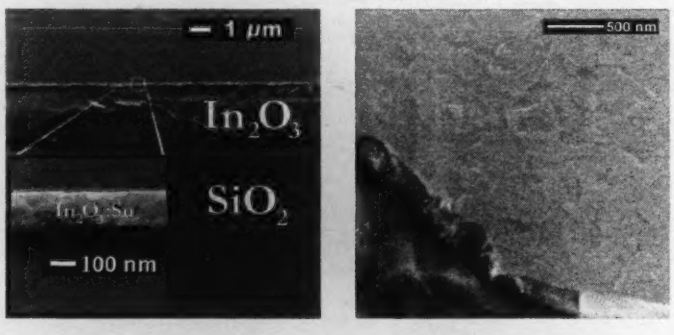


a) b)

**Figure 3.5: SEM images displaying a) layer structure and b) surface roughness of $In_2O_3$:Sn coated glass substrate.**

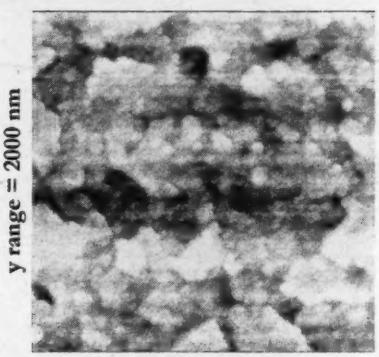


**Figure 3.6: AFM map of the $In_2O_3$:Sn surface from which the roughness was calculated.**

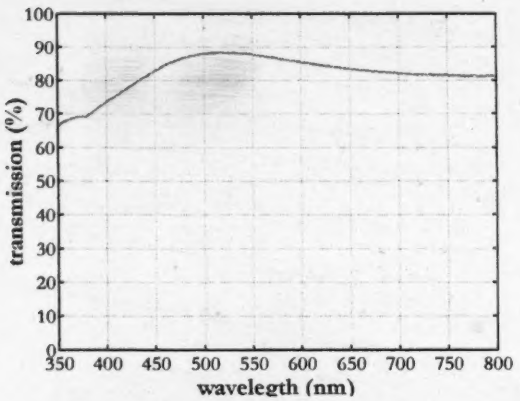


**Figure 3.7: Transmission of $In_2O_3$:Sn coated glass across wavelength range of primary interest.**

## 3.3 Films deposited

### 3.3.1 Deposition

Films of titanium dioxide were deposited on unheated substrates using the GLAD technique and reactive electron beam evaporation in a vacuum system with a water cooled bell jar, the layout of which is diagrammed in Figure 3.8. The substrates were mounted on a motorized substrate holder positioned 42 cm above the crucible. In addition to the $In_2O_3$:Sn substrates previously described, silicon wafers were mounted to serve as witness samples. The chamber was evacuated by rotary mechanical pumping to 13.3 Pa and subsequently by diffusion pumping to base pressures less than $2.4 \times 10^{-4}$ Pa. The source material used was 3-6 mm pieces of 99.9% pure rutile $TiO_2$ from CERAC incorporated. When struck by the electron beam, this source material dissociates into a variety of species and deposits sub-stoichiometrically [101]. In order to improve the stoichiometry of the deposited films, Air Liquide UHP oxygen was added into the chamber near the substrate until a pressure of $7.3 \times 10^{-3}$ Pa was measured by the Bayard-Alpert gauge located at the diffusion pump mouth. This value was chosen such that the GLAD requirement of collimated flux would be maintained. Using this pressure, the mean free path of titanium dioxide was calculated to be greater than twice the crucible/substrate separation. This ensured minimal scattering of the incoming flux.

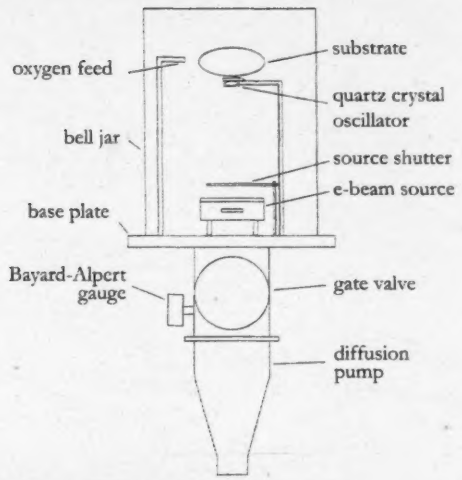


**Figure 3.8: Deposition chamber and vacuum system layout showing components of interest.**

The melt was conditioned before depositions commenced. This involved sweeping the crucible with a low current, 40 - 60 mA, electron beam with the shutter closed until a uniform melt pool was formed. The current was then slowly ramped up to the values required to achieve the desired deposition rate. The speed of the ramping process was limited by off-gassing due to the dissociation of the melt material into titanium, various oxides and sub-oxides, and oxygen [101]. The overall system pressure was required to be maintained below 0.133 Pa to satisfy the electron beam source safety interlocks. When the desired deposition rate was achieved and the melt ceased spitting, the substrate was moved to the initial position and the shutter was opened to begin the deposition.

The deposition rates were maintained between 9 and 10 Å/s using an 8.4 – 8.5 kV accelerating voltage and beam currents of 115 to 170 mA. The Sycon STM 100/MF quartz crystal oscillator controller was programmed with the density and acoustic impedance of stoichiometric titanium dioxide. After completion of the depositions, the samples were allowed to cool in a nitrogen ambient before being stored in air.

In order to cover a reasonably wide parameter space, the depositions were programmed to create a single structure at a variety of angles (slanted columns at 83°, 85°, and 87°), different structures at a single angle (slanted columns, vertical posts, corkscrews, and square spirals at

85°), and a single structure at a single angle with different thicknesses (slanted columns at 85° of ~1.5 μm and ~3.5 μm). All samples except sample G were programmed to be 1.5 μm thick.

### 3.3.2 Scanning electron microscope analysis

The silicon wafer witness samples were cleaved, mounted on aluminum sample stubs using conductive silver epoxy, and coated with a thin layer of chromium for analysis in a JEOL JSM6301FXV scanning electron microscope (SEM) with a field emission electron source running at 5 kV. This instrument allowed analysis of the film structure. The actual thickness found for the samples varied from the programmed 1.5 μm. This is due to slight changes in the quartz crystal oscillator thickness ratio with deposition angle, rotation speed, and wafer position on the substrate holder [102]. Details of the samples from the cross-sectional SEM views of Figure 3.9 are given in Table 3.1.

**Table 3.1**

| Sample | Deposition Angle (°) | Structure | Thickness (μm) | Column Angle (°) |
|---|---|---|---|---|
| A | 83 | Slanted columns | 1.83 | 50 |
| B | 85 | Slanted columns | 1.68 | 52 |
| C | 87 | Slanted columns | 1.33 | 46 |
| D | 85 | Vertical posts | 1.16 | 0 |
| E | 85 | Corkscrews | 1.30 | 59 |
| F | 85 | Square spirals | 1.08 | 48 |
| G | 85 | Slanted columns | 3.45 | 57 |

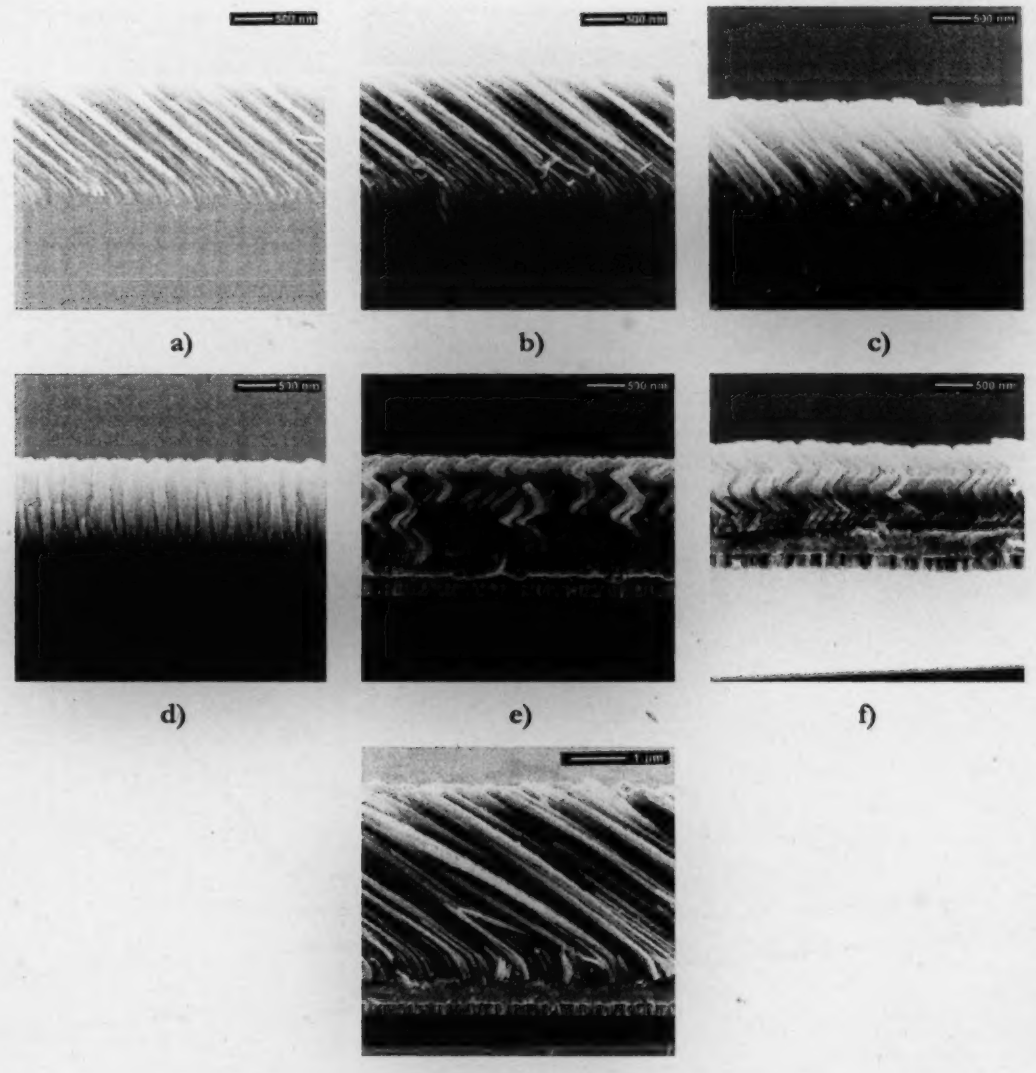


**Figure 3.9: Cross-sectional SEM images of samples A through G as indicated in lowercase below the images.**

The oblique views of the deposited films, Figure 3.10, show them to be highly porous, a property obscured by the large depth of field in the cross-sectional views of Figure 3.9. Only one picture of each type of structure is shown here, as all slanted column films appear similar to sample C. The structures formed are similar to those formed from other materials, with anisotropy in the direction perpendicular to the incoming flux [103, 104], shown in Figure 3.11, and broadening of structure with growth.

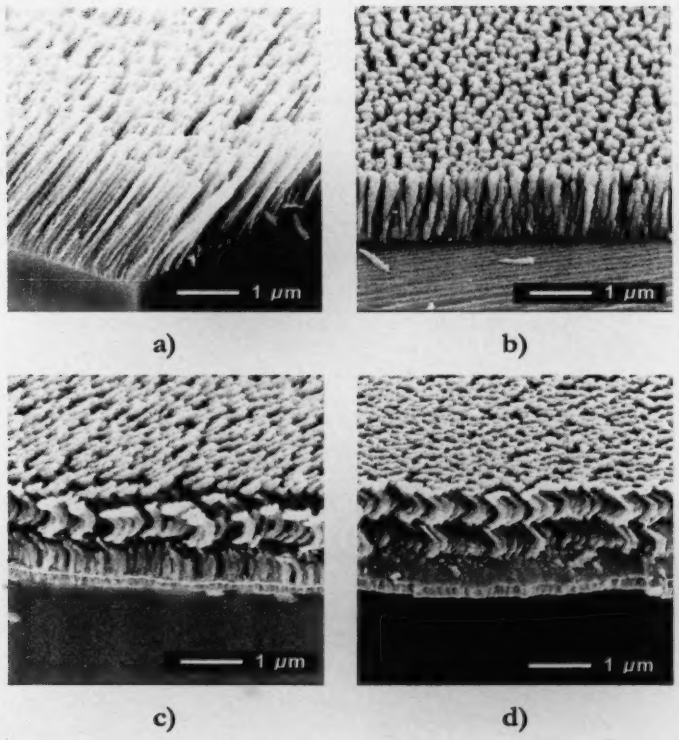


**Figure 3.10: Oblique SEM views of samples a) C, b) D, c) E, d) F showing highly porous nature of the films. Samples A, B, and G appear very similar to sample C.**

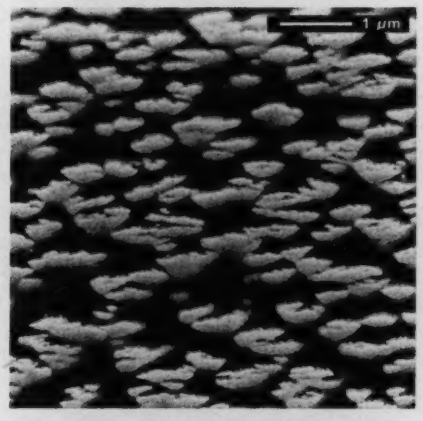


**Figure 3.11: SEM view taken down the columns of sample G. The flux was incident from the bottom of the picture. Anisotropy can be seen in the direction perpendicular to the incoming flux. A difference in texture of the column sides is noted where the columns are smooth on the sides where flux is incident and rough on the opposite side.**

A deviation from standard GLAD structure was observed in the cross-sectional views of the slanted column films. At the very base of the columns, shown magnified in Figure 3.12, growth appears to begin vertically before evolving within the first 200 nm of vertical thickness to the final column angle. This was initially believed to be due to the motion of the substrate as it came from a protected position into the deposition position, but was later shown to be due to increased gas pressure within the chamber. At the beginning of the depositions, the dissociation of fresh melt material caused the chamber pressure to rise significantly. Once the melt became somewhat oxygen depleted, this source of gas decreased and the chamber pressure dropped down to its deposition value. As the deposition began once the melt had been conditioned into a single pool and before the chamber pressure reached its deposition value, a small amount of film was deposited at this higher oxygen pressure. Using the maximum pressure attained at the start of any deposition and equation 3.3a [105], the mean free path of titanium dioxide can be calculated to be less than one fifth of the crucible/substrate separation. Such a high pressure region originating close to the crucible would create highly scattered flux, depicted in Figure 3.12, the result of which would be a nearly isotropic distribution of incoming flux, leading to a dense film with vertically oriented columns.

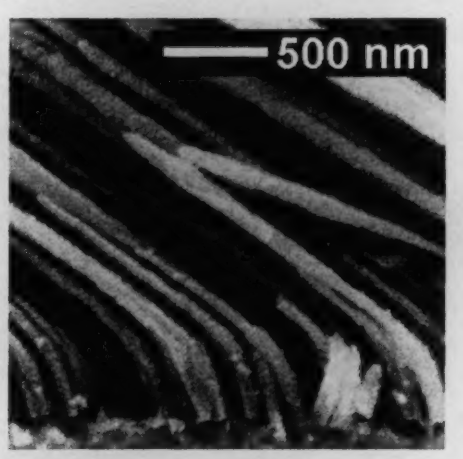


**Figure 3.12: Magnified SEM view of the base of sample G. The initial vertical growth due to flux randomization is seen.**

$$\lambda_{mfp} = \frac{kT}{p\pi\sqrt{2}d_o^{\,2}} \qquad \textbf{Eq. 3.3a}$$

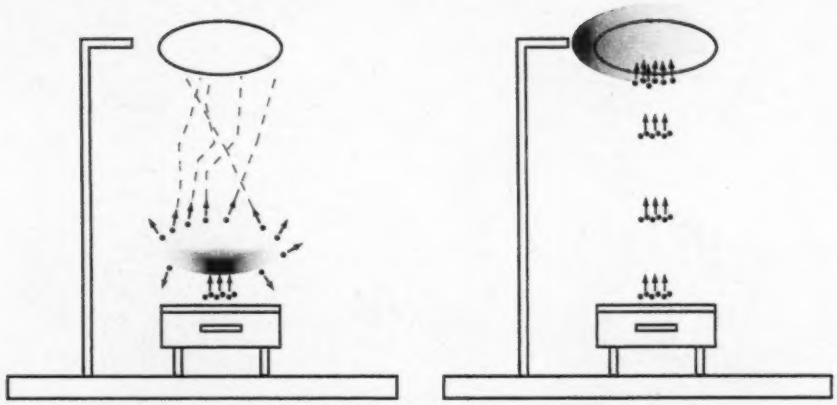


**Figure 3.13: Scattering of deposition flux by gas. a) Initial off-gassing of fresh material causes an extremely high pressure region originating directly above crucible, resulting in highly scattered flux. b) Gas inlet near substrate resulting in a high pressure region close to substrate that scatters flux minimally.**

### 3.3.3 Transmission electron microscope analysis

Samples for transmission electron microscope (TEM) analysis were prepared from silicon wafer witness samples not coated for SEM analysis. Areas of film were scraped off with a scalpel and placed onto carbon coated TEM grids. A drop of isopropyl alcohol was used to evenly disperse the structures over the grids. They were allowed to dry overnight before being analyzed in a JEOL 2010 TEM. The samples were imaged at 200 kV and the crystal structure was analyzed by electron diffraction. This analysis was performed with the assistance of Barbara Djurfors of Chemical and Materials Engineering.

The TEM bright field images, some of which are shown in Figure 3.14, show the films to have even higher surface area than indicated by the SEM. Independent of the type of structure or angle used in the deposition, each individual column or structure has a fine feathery structure. This has been observed before and is due to the bifurcation of the individual fibres that make up the larger structure [106]. This causes the overall surface area of the film to be significantly larger than one might estimate from the SEM images.

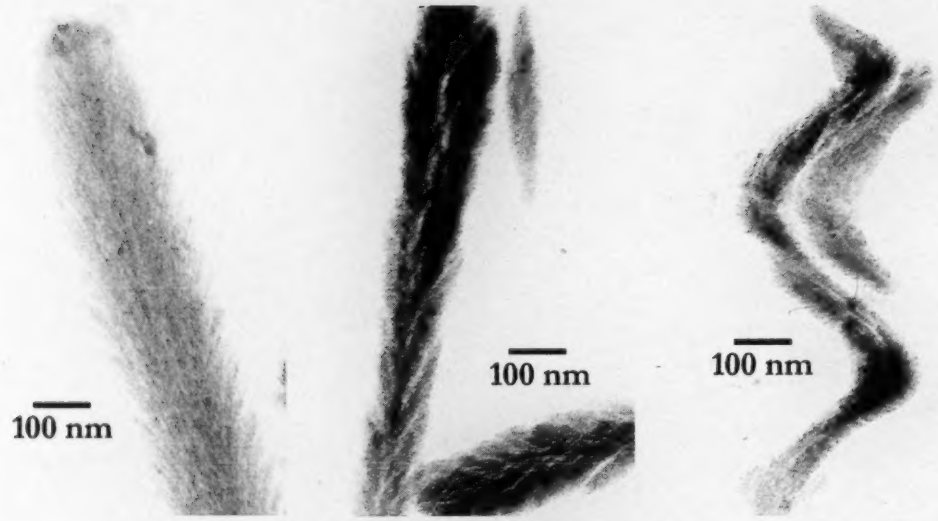


**Figure 3.14: Bright field TEM images of samples B, D, and E, showing highly porous, fine feathery structure of slanted columns, vertical posts, and corkscrews respectively.**

All samples exhibited diffuse amorphous diffraction patterns similar to Figure 3.15. This is in accordance with the literature, wherein titanium dioxide deposited by electron-beam evaporation is found to be amorphous when no substrate heating is utilized [107]. The crystal structure of the particles typically used in dye sensitized solar cells is the low temperature polymorph anatase, while thin films of titanium dioxide are also known to exist in the high temperature stable rutile form.

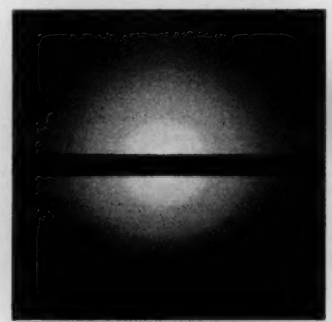

**Figure 3.15: Diffuse diffraction pattern of sample D, indicating the amorphous nature found in all generation I samples.**

### 3.3.4 Optical transmission

The optical transmission spectra of the films were acquired using the same double beam spectrophotometer described previously. GLAD films are known to be highly scattering: a major factor so far preventing them from being integrated as optical components, despite their optical activity [88]. In order to obtain close to the total transmission spectra of the films, the samples were oriented such that the sample beam first encountered the glass, with the film side being placed as close as possible to the sample port of the integrating sphere, as shown in Figure 3.16. A baseline correction [108] was performed using a bare piece of $In_2O_3$:Sn coated glass.

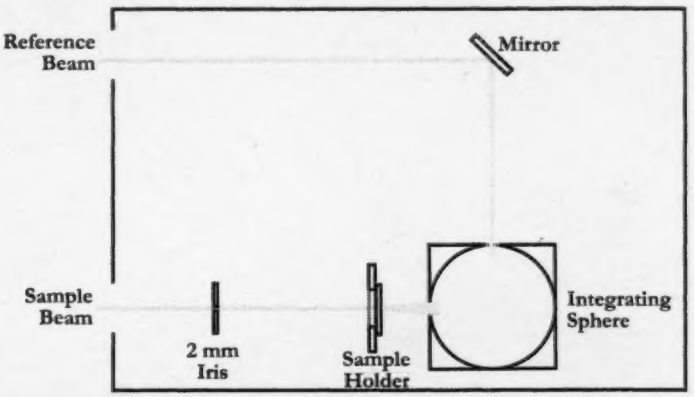


**Figure 3.16: Set-up of optical bench to measure total transmission of samples.**

All of the thinner samples displayed transmission greater than 80% at 800 nm, decreasing to values between 35 and 51% at 350 nm, as shown by Figure 3.17. Only the vertical post film, sample D, exhibited the maxima and minima usually associated with thin film interference. A possible explanation of this phenomenon is that the highly random nature of the other structures, due to extinction and broadening of columns, presents a medium that is highly variable across the beam spot. Only the vertical post film presented a reasonably constant mixed medium. The variation across the beam spot, present in most films, results in destructive interference in one region canceling the constructive interference from another region, thereby eliminating the interference peaks. The transmission decreases as the wavelength approaches the absorption wavelength of titanium dioxide at approximately 350 nm [109]. Because the dye is adsorbed throughout the film, the low external total transmission values were thought to be of little concern.

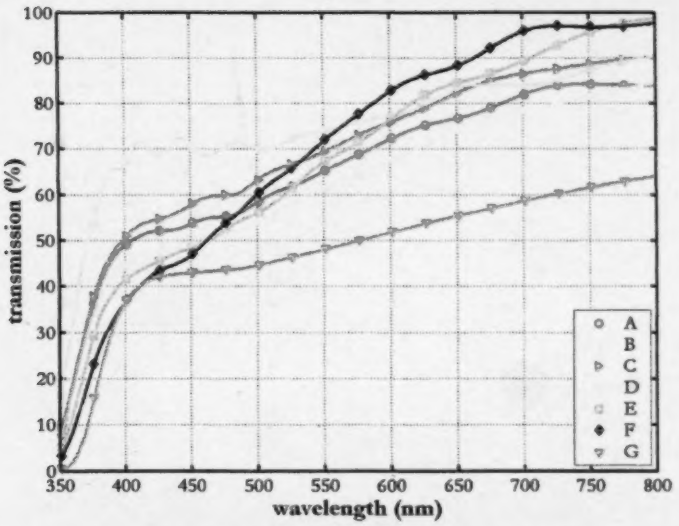


**Figure 3.17: Transmission of titanium dioxide films across wavelength range of primary interest. All samples < 2 μm thick exhibit transmission greater than 80% at 800 nm.**

## 3.4 Dye sensitization

### 3.4.1 Dye

Due to the complexity of the dye synthesis process [53] and the desire to use conventional materials, the dye used in these experiments was purchased from Solaronix SA. Several different dyes were available, and the decision was made to use Ruthenium 535 bis-TBA. This dye, although not identical to that used in the initially reported cells of O'Regan and Gratzel, performs very similarly. This ruthenium dye is said to be an improvement upon that original dye, creating photovoltages 50 to 100 mV higher in an otherwise identical system [110]. The full chemical name of the dye is *cis*-bis(isothiocyanato)bis(2,2'-bipyridyl-4,4'-dicarboxylato)-ruthenium(II) bis-tetrabutylammonium. It has a molar mass of 1188.5 g/mol and, as purchased, consisted of a fine dark purple powder.

### 3.4.2 Solution preparation

In order to prepare solutions appropriate for sensitization of the titanium dioxide electrodes, 35.7 mg of Ru 535 bis-TBA were dissolved in a small amount, approximately 10 mL, of 200 proof pure ethyl alcohol. The concentrated solution and remaining solid pieces of dye were then transferred to a 100 mL volumetric flask and the previously used beaker was rinsed

with ethyl alcohol and poured into the flask. The volumetric flask was topped up with ethyl alcohol and capped, creating a final 0.3 mM solution. The solution was placed in an ultrasonic bath to enhance the dissolution of the remaining solid pieces. Once dissolved, the solution was a dark red/purple colour. The volumetric flask was wrapped in tin foil to prevent any light induced degradation from occurring. The absorption spectrum of the dye in ethyl alcohol, provided by Solaronix SA is shown in Figure 3.18 [111]. The preparation of chemicals and measurement of properties was performed with the assistance of Dr. Gregory Kiema, a Ph.D. chemist currently working as a research associate with Dr. Brett.

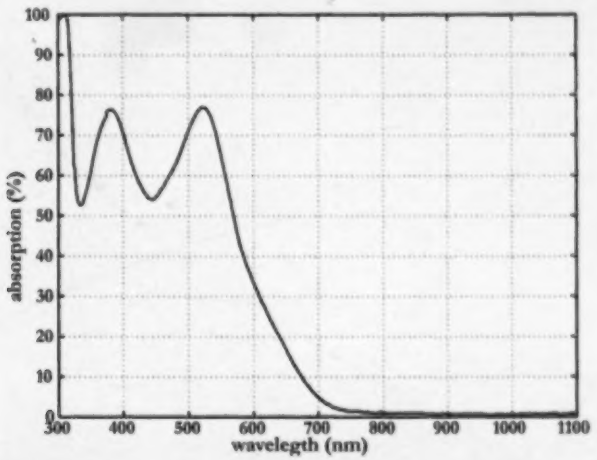


**Figure 3.18: Absorption spectrum of Ru 535 bis-TBA dissolved in ethyl alcohol.**

### 3.4.3 Sensitization

Sensitization of titanium dioxide electrodes was performed in wide-mouthed transparent glass containers. Approximately 50 mL of the prepared 0.3 mM dye solution was poured into two separate containers and one titanium dioxide sample at room temperature was placed in each. The jars were wrapped in tin foil and the samples left immersed overnight as suggested in the literature to allow for full sensitization at room temperature [66]. Once sensitization had occurred, the samples were rinsed with ethyl alcohol to remove any excess dye solution. The samples were then dried in a nitrogen stream and stored in air. After drying, the films had a pink or red coloration.

### 3.4.4 Adsorption

The amount of dye adsorbed in the film is a critical parameter because it indicates both the surface area of the film and the maximum number of electrons that can be injected at high light intensities before saturation of the cell. The amount of adsorbed dye was analyzed by desorbing the adsorbed dye into a known amount of solvent. The solvent chosen in this case was a potassium hydroxide solution. Both water and solutions of potassium hydroxide are known to cause dye desorption, however as potassium hydroxide solutions were used for similar purposes in the literature, they were chosen in the hope that direct comparisons could be made [60].

Using volumetric flasks, 10 mL of 1 mM aqueous potassium hydroxide were measured out and poured over samples in small Petri dishes. To accelerate the desorption process, samples were placed on top of the lid of an ultrasonic bath at low power setting and left for 40 minutes. When completed, the resulting solutions were transferred to amber sample vials for subsequent optical analysis.

Standard comparison solutions were produced by dilution of a carefully prepared 0.3 mM dye solution with potassium hydroxide. The concentrations of these standard solutions ranged from 3 μM to 15 μM. Samples of the standard solutions were placed in optical glass cuvettes transmissive in the 360 – 2000 nm range, with light path lengths of 10 mm, for optical analysis. Complete optical spectra were obtained for these standard sample solutions using the double beam spectrophotometer described earlier with the standard sample compartment and detector. A baseline correction was made using 1 mM potassium hydroxide solution. It was found that the dye had an absorption maximum at 517 nm. The absorbance, as defined by equation 3.4a obtained from Beer-Lambert's Law, was plotted against the known concentration of the solution, resulting in the straight line calibration plot of Figure 3.19, for determination of sample concentration.

$$A = -\log_{10}(T) \qquad \textbf{Eq. 3.4a}$$

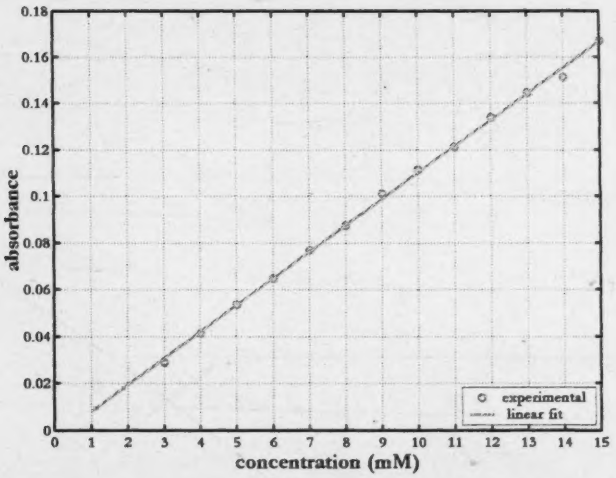


**Figure 3.19: Calibration plot for determination of adsorbed dye concentration from optical transmission of solutions.**

Once the calibration plot had been obtained, the samples obtained from the titanium dioxide films were scanned for comparison. Using the transmission obtained at 517 nm, the absorbances of all samples were calculated and placed on the calibration plot. The resulting concentrations were read off the bottom axis. In order to normalize these concentrations for varying film thicknesses and substrate coverages, they were divided by the overall volume occupied by the film. This volume was calculated by multiplying the top down area of the film by the thickness obtained from SEM imaging. The number of molecules of dye adsorbed per unit volume of the samples is shown in Table 3.2.

**Table 3.2**

| Sample | Amount of dye ($\times 10^{-6}$ moles/cm$^3$) |
|---|---|
| A | 48.9 |
| B | 29.2 |
| C | 46.7 |
| D | 55.9 |
| E | 70.6 |
| F | 42.4 |
| G | 37.6 |

No clear trend is observed across deposition angle, structure or variable thickness. This supports the supposition that GLAD structures evolve in a similar manner regardless of the deposition parameters and, though columns broaden and extinguish with continued growth,

the growth is in a self-similar manner [85]. A very similar procedure was carried out by Gomez et al. [60] with sputtered titanium dioxide, however the method in which the data was reported allowed only for relative comparisons within their data set and cannot be compared against the data obtained in this study.

A detailed study of the adsorption behaviour of a similar ruthenium based dye on titanium dioxide nanocrystalline particles was performed by Fillinger and Parkinson [112]. They found that adsorption slowed significantly after 10 hours, reaching equilibrium for unheated substrates after 60 hours. Desorption of the dye into unagitated ethyl alcohol was found to be significantly slower than the adsorption, taking up to 10 days to reach equilibrium. It was also found that only a fraction, up to one half, of the adsorbed dye desorbed into the ethyl alcohol. It is believed that this issue does not apply to the study described in this thesis because potassium hydroxide solutions have been indicated to rapidly strip ruthenium dyes from titanium dioxide.

## 3.5 Device construction

The construction of the solar cells proceeded in a manner similar to that reported in the literature [60, 67, 113]. The counter electrodes used were electron beam evaporated platinum on silicon wafers. The titanium dioxide electrodes were sensitized in the same manner as described above. These electrodes were separated by microscope cover slips of 150 μm thickness and were held together by binder clips. The electrolyte used was Iodolyte TG 50 from Solaronix SA [114]. This is an iodide based electrolyte containing 50 mM of triiodide in a high boiling point anaqueous solvent. The electrolyte was introduced into the interelectrode space by capillary action and proceeded until the entire space was filled. These cells, depicted schematically in Figure 3.20, were not sealed in any way and were tested for performance immediately after assembly.

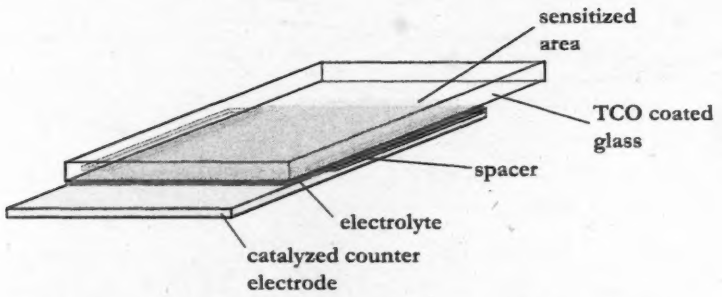


**Figure 3.20: Diagram of constructed devices. Binder clips were used to hold this sandwich structure together.**

## 3.6 Device testing

### 3.6.1 Light source

A standard 100 W tungsten filament light bulb placed 30 cm from the cells was used as the light source for these experiments. A computer based Ocean Optics SD2000 spectrometer with dual infrared/visible input fibres was used to measure the spectral output of the source. This source was found to have a broad peak between 450 and 850 nm, with –3 dB points at 488 and 725 nm. The power of the bulb at the test cell location was measured using a pyro-electric meter and divided by the sensor area to determine an intensity of 22.8 mW/cm$^2$.

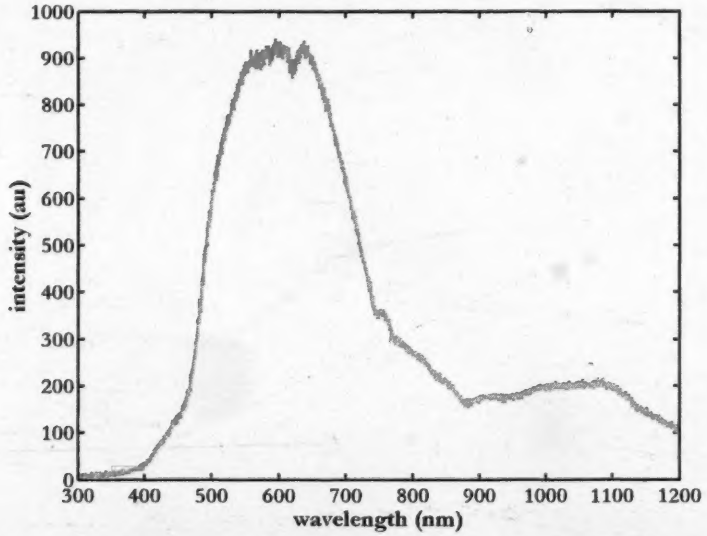


**Figure 3.21: Spectrum of tungsten bulb as measured by Ocean Optics dual input spectrometer.**

### 3.6.2 Electrical measurements

Contact was made to each electrode using flattened alligator clips. A calibrated decade resistor box was used as a variable load between the two connections. The voltage across the cell was measured using a Fluke 73 III Multimeter on DC Voltmeter setting. The current flowing from the cell under test was obtained using Ohm's law. This current was normalized to the exposed active area of the cell to allow for comparison between the cells. The cells were allowed to equilibriate under illumination at open circuit conditions before testing commenced.

### 3.6.3 Device performance

**Table 3.3**

| Sample | $V_{oc}$ (mV) | $J_{sc}$ ($\mu A/cm^2$) | FF (%) | Efficiency (%) |
|---|---|---|---|---|
| A | 564 | 13.5 | 58.1 | 0.0194 |
| B | 558 | 9.27 | 56.0 | 0.0127 |
| C | 564 | 7.54 | 49.0 | 0.0091 |
| D | 566 | 8.30 | 54.2 | 0.0112 |
| E | 561 | 8.76 | 55.5 | 0.0119 |
| F | 552 | 9.43 | 52.8 | 0.0121 |
| G | 552 | 15.7 | 53.0 | 0.0201 |

The open circuit voltages obtained for all samples ranged between 552 mV and 566 mV. These measurements show all materials to have been composed of near identical stoichiometry because of the very close agreement between their conduction band edges. The voltages are similar to those reported in the literature [62, 115], but approximately 150 mV less than those of the highest efficiency cell [71, 72].

The short circuit current densities were found to range between 7.54 and 15.65 $\mu A/cm^2$. With respect to current density, some conclusions can be drawn regarding the effect of deposition parameters. All films approximately 1.5 μm thick and deposited at 85° were found to have similar short circuit current densities. From this, it is seen that the actual structure of the film has little impact on device performance. The deposition angle, however, appears to have a substantial effect on device performance. As the deposition angle varies from 83° to 87°, the short circuit current density is found to decrease by almost half. This trend, plotted in Figure 3.22, implies that more closely spaced columns result in higher current densities. This is likely due to increased surface area available for dye

adsorption. If sample B is ignored, this trend is just visible in the dye desorption results. Finally, the thicker film grown at 85° exhibits the highest short circuit current density of any sample. This was to be expected as it incorporated the most dye and thus had the largest number of dye molecules capable of being excited and injecting electrons. Similar results have been reported for other deposition techniques [115, 116].

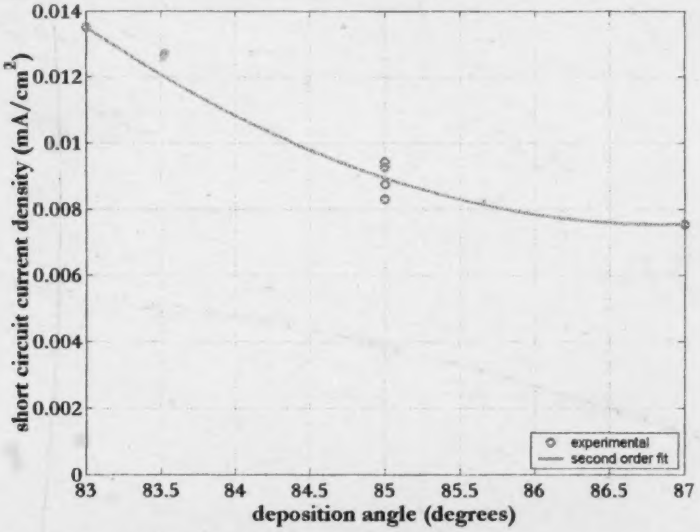


**Figure 3.22: Trend showing decreasing short circuit current density with increasing deposition angle.**

The short circuit current densities found here are significantly below most values reported in the literature. Gomez et al. reported values of between 45 and 490 $\mu A/cm^2$ for sputtered films [60], but these were rapidly improved into the more common range of greater than 1 $mA/cm^2$ [115]. The most efficient cells typically have short circuit current densities of greater than 15 $mA/cm^2$ [71, 72], representing a nearly thousand fold increase from the best value found for these initial GLAD based cells. The most striking material difference between the films used in this study and those used in nearly all other studies is that the GLAD films consist of amorphous titanium dioxide. The random structure likely incorporates a much higher number of traps and has a more poorly defined conduction band than structured crystalline materials. This would result in significantly increased transit times for the electrons, leading to greatly increased recombination with the electrolyte.

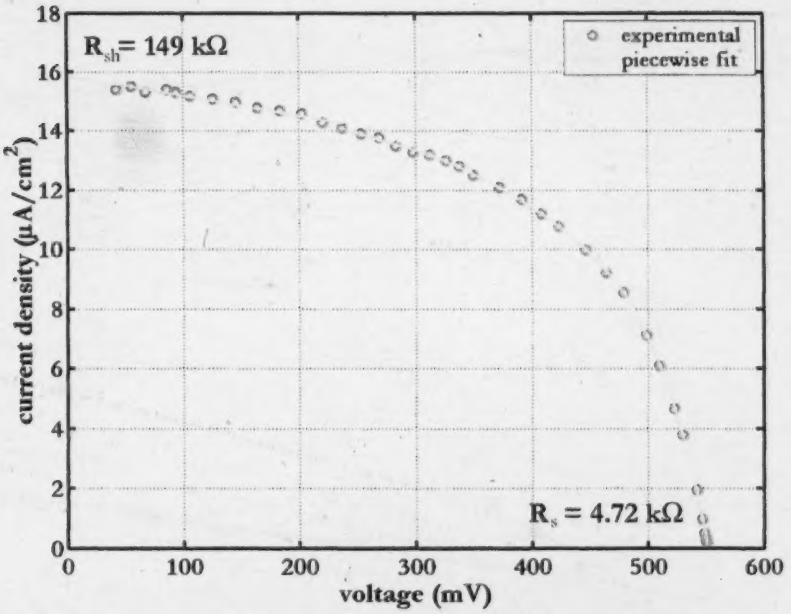


**Figure 3.23: Current-voltage characteristic of device incorporating sample G: the best performing generation I device.**

All films were found to have similar fill factors of between 49.0 and 58.1%, indicating that the current-voltage curves, an example of which is plotted in Figure 3.23, have similar shapes and that similar loss mechanisms are present in all cells. The most efficient cells reported in the literature exhibit fill factors greater than 70% [71, 72], showing superior current providing properties at midload.

The efficiencies of the devices were calculated for the source being used. That is, equation 2.1c was calculated using the measured intensity of the light source. Due to the extremely low photocurrents, the efficiencies of all these devices are well below one percent, ranging from 0.0091% to 0.0201%. Because the efficiencies are limited by the short circuit current densities, the trends in efficiency follow those in the short circuit current density. From these trends, it can be suggested that the structure of the film is unimportant, while lower deposition angles and thicker films result in the highest efficiencies.

# 4 Chapter 4: Generation II Devices: Annealed Films

This chapter discusses the second generation of dye sensitized solar cells incorporating electron collecting layers fabricated by glancing angle deposition. As identified in Chapter 3, the amorphous nature of the titanium dioxide structures is thought to result in extremely large losses. This chapter explores titanium dioxide layers that have been modified by thermal annealing. Details of the annealing process will be given, followed by a thorough characterization of the resulting structures. Finally, the effect of annealing on dye adsorption is examined, along with its ultimate effect on the performance of the solar cells.

## 4.1 Annealing

In nearly all published studies of dye sensitized solar cells using titanium dioxide electron collecting layers, the titanium dioxide was used in a crystalline form, usually anatase [4, 60, 62, 113]. In one particular study, anatase titanium dioxide particles were compared against rutile titanium dioxide particles [117]. It was found that the effective electron diffusion coefficient was lower in rutile films, leading to reduced photocurrent densities at short circuit. The desired crystalline form of titanium dioxide was thus taken to be anatase.

Titanium dioxide has long been used as an optical material because of its high refractive index and non-absorbing nature across the majority of the visible spectrum [118-120]. This has led to many detailed studies of deposition methods and treatment techniques. From this body of knowledge, it is seen that annealing of amorphous titanium dioxide thin films in air results in crystallization, the final form of which may be controlled by the annealing temperature. There is a wide window, extending from 350°C to 800°C, in which anatase films may be obtained [121]. Below 350°C, the annealing temperature is insufficient to cause large scale crystallization, while above 800°C, conversion to rutile is the thermodynamically preferred result. Based on this annealing window and a desire to avoid reflowing of the glass substrates, the annealing temperature was chosen to be 500°C. This is above the temperature required for sintering of nanocrystalline titanium dioxide particles reported by many [51, 116], below the glass transition point of standard glasses (~550°C), and well below the transition point to rutile.

In order that direct comparisons in performance could be made with generation I devices, unused samples from those same depositions were employed in this study. The annealing was performed in air in a Thermolyne 48000 muffle furnace. Samples were annealed for 5 hours and then left to cool for over 14 hours before being removed. At removal, the furnace temperature had cooled to 24 - 28°C. These films were stored in air for at least one day before further analysis took place.

## 4.2 Annealed films

### 4.2.1 Scanning electron microscope analysis

Witness samples on silicon wafers annealed as described above were cleaved, mounted, coated, and imaged in a manner identical to those samples from generation I. These images, shown in Figure 4.1, indicated that no discernible change in microstructure occurred during the annealing process. Film parameters were remeasured and compared against the pre-annealing values in Table 4.1. In some samples, there were small differences in the measured thickness and column angle values. However, no clear trend of increase or decrease for either parameter was seen. Because of the small structure size and porous nature of films fabricated with GLAD, one might expect that some "reflow" along the structure would have occurred. By examining the SEM images, it appears that for these particular annealing conditions, no reflow or densification occurred. The source of difference in these measurements must be found elsewhere.

**Table 4.1**

| Sample | Deposition Angle (°) | Structure | Thickness (μm) | | Column Angle (°) | |
|---|---|---|---|---|---|---|
| | | | Annealed | As-deposited | Annealed | As-deposited |
| A-a | 83 | Slanted columns | 1.71 | 1.83 | 46 | 50 |
| B-a | 85 | Slanted columns | 1.48 | 1.68 | 52 | 52 |
| C-a | 87 | Slanted columns | 1.44 | 1.33 | 45 | 46 |
| D-a | 85 | Vertical posts | 1.15 | 1.16 | 0 | 0 |
| E-a | 85 | Corkscrews | 1.27 | 1.30 | 56 | 60 |
| F-a | 85 | Square spirals | 1.17 | 1.08 | 50 | 48 |
| G-a | 85 | Slanted columns | 3.40 | 3.45 | 53 | 57 |

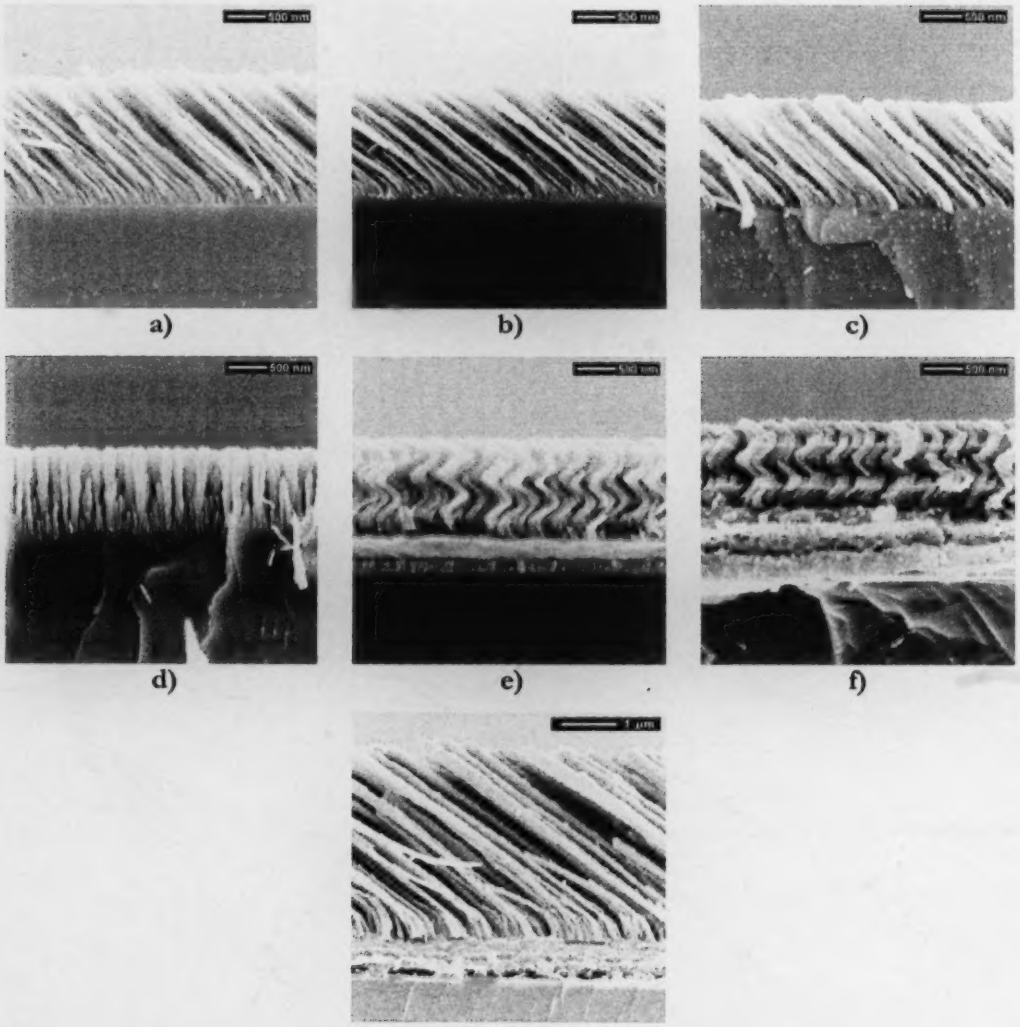


**Figure 4.1: Cross-sectional SEM images of samples A-a through G-a, the first letter as labeled below the image. No major structural changes occurred due to the annealing process.**

The variation in film thickness with annealing was instead attributed to a lack of uniformity of the samples, rather than an effect of the annealing process. Uniformity of thin films is an issue that has received great attention due to its importance in industrial processing. Numerous methods have been attempted to ensure that all substrates in a deposition system receive equal amounts of flux [122-125]. The well-known cosine law of emission is often used to determine the placement of substrates such that equal flux should be deposited on

each [126]. This formula results in substrates being placed progressively closer to the source as they move off of the source normal. The best uniformity is usually obtained using "planetary" arrays, where the substrates are rotated continuously through a variety of positions to randomize the flux they receive. In contrast to all these efforts to achieve uniformity, GLAD conditions accentuate non-uniformity. Particularly for the slanted post microstructure deposited at high angles of incidence, the uniformity across the substrate holder is poor. For example, using the geometry from the deposition system employed in these experiments, changing co-ordinates to those of Figure 4.2, and equation 4.2a, a variation of up to 65% may be calculated across a 4" wafer held stationary at a deposition angle of 87°. In order to minimize these effects, all $In_2O_3$:Sn coated glass substrates were positioned such that they received equal amounts of flux. The silicon witness samples used in these SEM measurements were placed close by, however small variations in conditions from the $In_2O_3$:Sn coated glass samples and other silicon witness samples were expected.

$$\frac{dM_r}{dA_r} = \frac{M_e}{\pi r^2}\cos(\varphi)\cos(\alpha) \qquad \textbf{Eq. 4.2a}$$

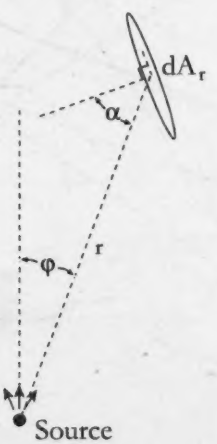


**Figure 4.2: Definition of angles for cosine equation.**

The lack of apparent change should not be taken to indicate that GLAD films are immune to the densification effects reported by others working with normally deposited, or "dense" films [127]. Recent experiments by Peter Hrudey, a fellow graduate student, have shown that annealing a 50 nm europium oxide layer on top of a 400 nm film of yttrium oxide at 900°C for 75 hours resulted in a significant reduction of film thickness. Isolated columns

remained, however reflow of material was clearly visible and the overall thickness of the film had decreased to 300 nm.

### 4.2.2 Transmission electron microscope analysis

Samples of the annealed films were prepared and analyzed by TEM in the same way as those from the generation I devices. In contrast to the SEM analysis, the TEM analysis showed a marked change in the structure of the films. Bright field imaging, examples of which are found in Figure 4.3, showed that the feathery structure found in as-deposited films had collapsed into a solid structure, more closely resembling that revealed by the SEM image. Qualitatively, this resulted in the films having significantly reduced surface area. Again, this effect occurred regardless of the deposition conditions. Although surface area was considered a crucial parameter, it was hoped that improved electron transport through the structures would offset this negative effect of the annealing process.

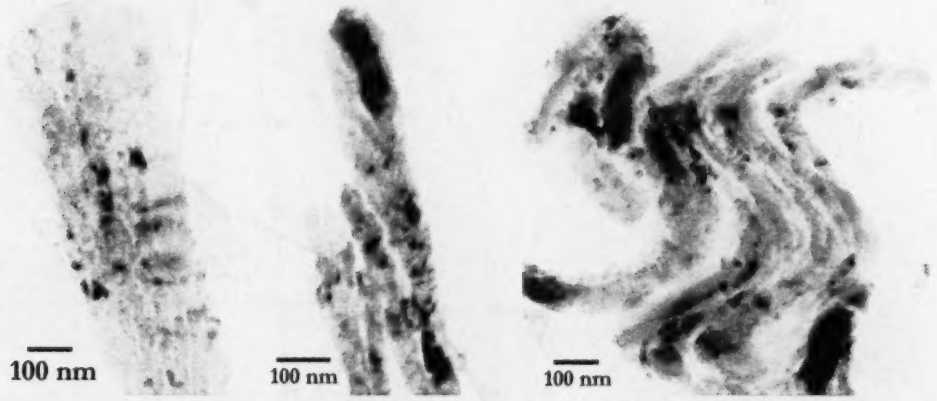


**Figure 4.3: Bright field TEM images of samples a) B-a, b) D-a, and c) E-a showing reduction of fine feathery structure. This reduction occurred in all structures.**

Electron diffraction revealed that the amorphous films of Chapter 3 had transformed to films with a polycrystalline anatase structure. Based on the dark field images, one of which is shown in Figure 4.4, the crystallites were typically 30 nm x 100 nm, although a wide distribution of crystallite sizes occurred. The crystallites were oriented randomly within the film, some spanning the width of the structure, others only forming a partial width of the column. In some images, there was evidence that two or more crystallites had begun to

grow together. A single crystallite was not found to compose an entire column in any of the samples examined, however if annealing had progressed, further crystallite growth until monocrystalline columns formed would not be unexpected.

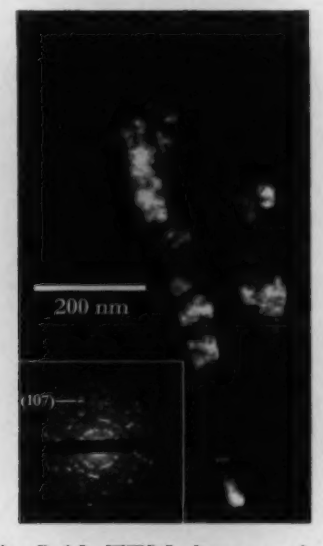


**Figure 4.4: Dark field TEM image showing part of the reflection from the (107) orientation. Inset is the polycrystalline diffraction pattern with the (107) ring labeled.**

### 4.2.3 X-ray diffraction analysis

In order to confirm the electron diffraction analysis, samples of film on silicon were analyzed in a Rigaku Rotaflex rotating anode x-ray diffractometer (XRD) with a thin film camera attachment. The Cu K $\alpha$ x-ray incidence angle was set to 2° from the sample surface to minimize sampling of the substrate. The filament was set to run at 40 kV, with 100 mA of current. Samples were scanned between 5° and 90° at a rate of 2°/min. This procedure was performed with both as-deposited samples from generation I devices and annealed samples from generation II devices. The resulting diffraction spectra, plotted in Figure 4.5, were compared against standard reference cards and confirmed that the as-deposited, generation I sample was amorphous, while the annealed, generation II sample consisted of a number of anatase peaks.

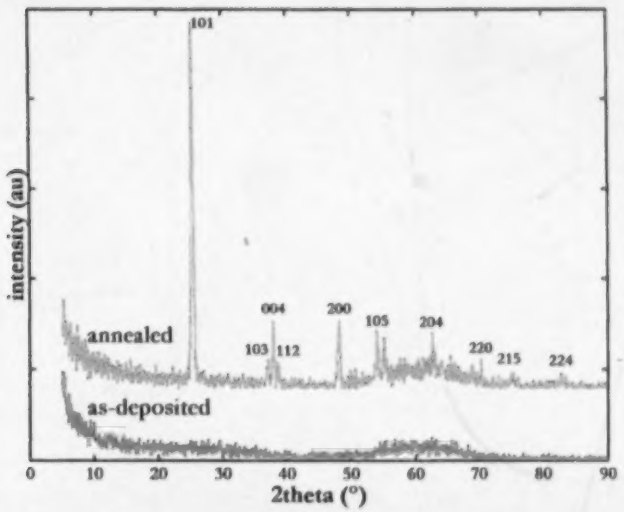


**Figure 4.5: XRD spectra of samples C and C-a as indicated on the figure. These spectra clearly indicate the transition to a polycrystalline anatase form caused by the annealing process.**

### 4.2.4 Optical transmission

The total optical transmission of the annealed samples on $In_2O_3$:Sn coated glass was obtained as described previously, with the baseline correction being made with $In_2O_3$:Sn coated glass annealed under the same conditions as the films, and plotted in Figure 4.6. All of the thinner films showed improved transmission at the long wavelength end, with the transmission being greater than 89% at 800 nm for all samples. The vertical post film remained the only film to exhibit thin film interference maxima and minima. In contrast, the thicker film, sample G-a showed poorer transmission at long wavelengths, with improved transmission at short wavelengths. The cross-over point in this behaviour occurred at 519 nm.

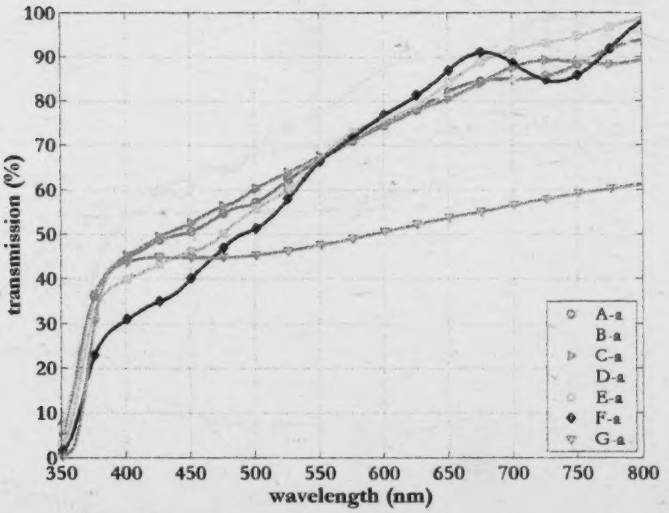


**Figure 4.6: Transmission of annealed titanium dioxide films across wavelength range of primary interest. All samples < 2 μm exhibit transmission greater than 88% at 800 nm.**

## 4.3 Dye sensitization

### 4.3.1 Dye

The dye used for this second generation of devices was identical to that used in the first generation. 0.3 mM solutions were prepared in the same manner previously described. The sensitization of the films for the adsorption study and for device testing was carried out following the procedure described in Chapter 3.

### 4.3.2 Adsorption

Using the desorption process described in Chapter 3, the amount of dye adsorbed into the annealed samples was examined and summarized in Table 4.2. It was found that all annealed samples, except sample B-a, contained less adsorbed dye per unit volume than the as-deposited samples. This finding is in agreement with the lower surface area of the samples seen in the TEM images. The discrepancy of sample B-a is thought to be due to experimental error, rather than an actual difference in the film. It should be noted that sample B-a was the only sample to exhibit a significant decrease in thickness with annealing. As explained previously, such a large decrease may not have actually occurred. Coupled with the uncertainty in determining the sensitized area of the film, this leads to near identical

results for annealed and as-deposited samples. The trend of increased dye incorporation with decreasing deposition angle was again noted.

**Table 4.2**

| Sample | Amount of dye ($\times 10^{-6}$ moles/cm$^3$) | |
|---|---|---|
| | Annealed | As-deposited |
| A-a | 47.1 | 48.9 |
| B-a | 34.9 | 29.2 |
| C-a | 32.9 | 46.7 |
| D-a | 49.7 | 55.9 |
| E-a | 45.0 | 70.6 |
| F-a | 34.2 | 42.4 |
| G-a | 17.6 | 37.6 |

## 4.4 Device performance

Solar cells incorporating the annealed GLAD films were assembled using the procedure described in Chapter 3. Testing was done using the same equipment described previously, but yielded much improved results. In all cases, the annealed samples of the films performed better than their as-deposited analogs. This improvement was found to occur in open circuit voltage, short circuit current densities, and overall efficiency. For comparison, conventional nanocrystalline particle based dye sensitized solar cells were also constructed and tested.

### 4.4.1 Annealed GLAD electron collecting layer solar cells

**Table 4.3**

| Sample | $V_{oc}$ (mV) | $J_{sc}$ ($\mu$A/cm$^2$) | FF (%) | Efficiency (%) |
|---|---|---|---|---|
| A-a | 636 | 31.0 | 65.2 | 0.0564 |
| B-a | 589 | 24.0 | 60.2 | 0.0374 |
| C-a | 651 | 42.6 | 52.8 | 0.0642 |
| D-a | 633 | 38.8 | 54.2 | 0.0585 |
| E-a | 585 | 29.0 | 51.1 | 0.0380 |
| F-a | 585 | 42.4 | 51.8 | 0.0564 |
| G-a | 552 | 33.1 | 55.5 | 0.0444 |

The open circuit voltages ranged between 552 and 636 mV. This comparatively large spread is thought to be due to variations in the cooling rate following the annealing process. The annealing process is believed to have improved the stoichiometry of the titanium dioxide and

raised its conduction band edge. This band movement was also found by a number of other groups whose deposition techniques allowed them to vary the amount of oxygen incorporated into their titanium oxide films [119, 121].

The short circuit current densities of the cells incorporating annealed samples were found to be the greatest source of improvement over the as-deposited samples. The range of current densities was 24.0 to 42.4 $\mu A/cm^2$, showing a minimum factor of improvement of 2.1, with the greatest improvement being shown by sample C-a, where a factor of over 5.6 was found. The trends in current density identified in Chapter 3 vanished with the annealing process. The greatest improvements occurred in the annealed samples whose as-deposited analogs presented the lowest short circuit current densities. Perhaps the greatest surprise is that the cell incorporating the thicker sample, G-a, actually provided a smaller short circuit current than cells with electron collecting layers less than half its thickness. In contrast, nanocrystalline particle and sputtered films have been found to provide increased current with increasing thickness [51, 115]. Intuitively, a thicker film should incorporate more dye molecules, which should be able to provide more electrons for a given intensity of light. This effect was seen in the generation I devices. Sample G-a also provides the lowest open circuit voltage, in fact the same open circuit voltage sample G produced. These two factors indicate that the annealing process had the least effect on this film. This is attributed to more rapid cooling after the annealing process than was experienced by the other samples.

The fill factors of the cells remained somewhat constant. The majority of the cells incorporating annealed collecting layers showed a small improvement in fill factor over their as-deposited relatives, likely due to improved carrier transport properties and reduced recombination.

The efficiencies of these devices were found to improve by factors of 2.2 to 7.0. The range of efficiencies was 0.0374 to 0.064%. The best improvement was found in the cell incorporating sample C-a, whose current-voltage characteristic is plotted in Figure 4.7. This cell showed the greatest improvements in both open circuit voltage and short circuit current density of any cell, as well as displaying an improvement in fill factor. These three factors

resulted in not only the greatest improvement in efficiency, but also the highest overall efficiency of any device.

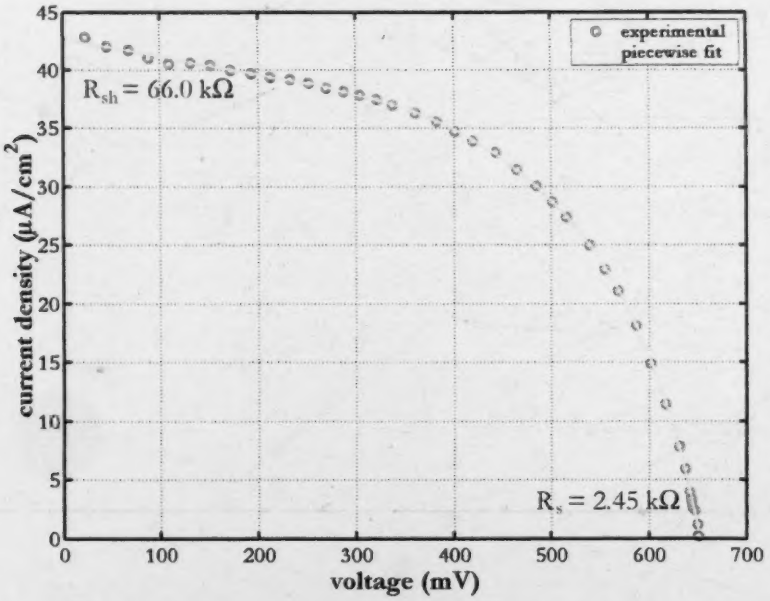


**Figure 4.7: Current-voltage characteristic of the device incorporating sample C-a: the best performing generation II device.**

The low short circuit current densities were again found to limit device efficiencies to values substantially below those reported in the literature. In order that direct comparisons under test conditions could be carried out, a conventional nanocrystalline particle based cell was fabricated.

### 4.4.2 Solar cell with nanocrystalline particle collecting layer

The fabrication of the nanocrystalline particle layer was initially carried out in a manner similar to published procedures [51]. The source material used was Ti-Nanoxide HT from Solaronix SA [128]. This product is a paste of anatase titanium dioxide particles of approximately 9 nm diameter.

Two layers of Scotch Tape from 3M Corporation were placed along the edges of an $In_2O_3$:Sn coated glass substrate. A small volume of the Ti-Nanoxide HT paste was

transferred from the vial onto the exposed $In_2O_3$:Sn surface and spread using a polished glass rod. The paste was dried overnight to allow the solvent to evaporate, resulting in a transparent film. The sample was then placed into a Thermolyne 48000 muffle furnace and heated to 450°C for 30 minutes. After this sintering process, the furnace was turned off and allowed to cool with the door open for 3 hours. At the end of this time, the sample was removed and the titanium dioxide layer was found to be extremely non-adherent. No useable test sample could be obtained with this procedure.

In order to minimize the thermal stress experienced by the sample during cooling, new samples were fabricated using only a single layer of tape. The titanium dioxide paste was spread as before and then left to cool overnight before sintering. The muffle furnace was slowly ramped up to 450°C at a rate no greater than 100°C/min. The sample was sintered for 30 minutes and then allowed to slowly cool overnight with the door closed. When removed, the sample had cooled to 25°C, but was still found to be only partially adherent. Attempts with cooling over several days produced only slightly improved results. Nevertheless, one of these films, sample Nano1, was used in a device.

After consultation with Solaronix, a pretreatment of the $In_2O_3$:Sn coated glass was attempted. First, the area was treated with a 2 mM solution of titanium tetrabutoxide in propanol, followed by a 350°C baking for 3 minutes. The goal of this procedure was to deposit a thin, dense layer of firmly adherent titanium dioxide onto the $In_2O_3$:Sn, after which a layer of adherent titanium dioxide nanocrystalline particles could be deposited.

Following this pretreatment, the nanocrystalline particles were spread over the area using a single layer of tape for spacing. The particles were sintered as before and allowed to cool overnight. The result was a much more adherent layer than previous samples, however non-adherent areas were still present. The non-adherent areas were removed by blowing with a nitrogen stream and this sample was designated Nano2.

Samples Nano1 and Nano2 were sensitized in an identical manner to the GLAD samples. Devices were then assembled using the same procedure and materials as both the generation

I and II GLAD based devices. Again, the same test procedure was employed and yielded the results shown in Table 4.4.

**Table 4.4**

| Sample | $V_{oc}$ (mV) | $J_{sc}$ ($\mu A/cm^2$) | FF (%) | Efficiency (%) |
|---|---|---|---|---|
| Nano1 | 492 | 245.6 | 54.8 | 0.290 |
| Nano2 | 644 | 262.4 | 46.4 | 0.344 |

Both devices incorporating the nanocrystalline particles performed at least five times better efficiency-wise than the top performing generation II device, sample C-a. A direct comparison between the current-voltage characteristics the three cells is made in Figure 4.9. The major source of improvement here was found to be the current providing capabilities of the nanocrystalline particle cells. Both samples were able to provide greater than 5.75 times the short circuit current density of sample C-a. Although these gains over both generation I and generation II GLAD based cells are significant, they are not the factor of 1000 required to reach the highest reported current densities.

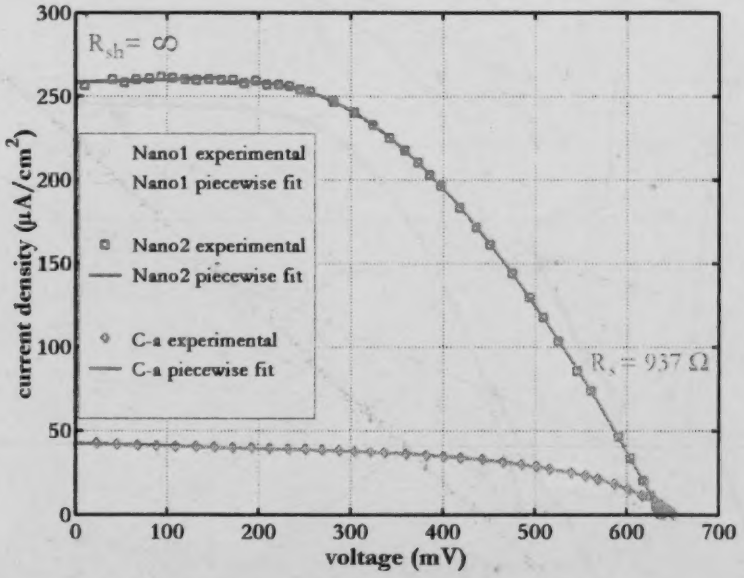


**Figure 4.8: Current-voltage characteristic of cells incorporating nanocrystalline particle layers, with the most efficient generation II device cell plotted for reference.**

Despite being clearly superior to the cells incorporating GLAD electron collecting layers, the nanocrystalline particle films performed significantly worse than the standard values found in

the literature [51]. The main area of limitation was again shown to be the current providing capabilities of the cells. An increase of at least twenty times was required to make these values comparable with those in the literature.

## 4.5 Areas of suspicion

At this point, sources of error in the experimental set-up and deficiencies in the materials were examined in an attempt to account for the discrepancies. A number of possible sources of low efficiency were found

### 4.5.1 Light source

The main area of suspicion in the solar cell testing set-up was the light source. Due to the expense of obtaining a solar simulator, a simple 100 W tungsten bulb was used to provide illumination for these experiments. In an attempt to minimize the effects on the numerical outcomes of the experiment, the source was characterized. The physics of the situation however, do not allow fair comparisons to be drawn using this method. When comparing the spectrum of the lamp against the standard AM1.5 spectrum, it can be seen in Figure 4.9 that the lamp does not produce illumination at either the short or long wavelength end of the spectrum. This lack of intensity appears more significant than simply a loss in power, because one of the dye's absorption peaks occurs below 500 nm, a region in which the tungsten lamp does not emit strongly. In fact, the presence of the absorption peak at 520 nm, a region in which the bulb emits more strongly than an AM1.5 spectrum normalized to the same overall intensity balances this out. This effect can be seen by examining the overlap integral, as specified by equation 4.5a, of the dye's absorption spectra with the intensity spectra of the source, be it tungsten lamp or standard spectrum. The overlap integral with the tungsten bulb was 0.27 and the overlap integral with the AM1.5 spectrum was 0.23. To account for differences in intensity, both intensity spectra were normalized such that the integrated areas under the curves were equal. Although the bulb did produce a larger value for the overlap, they were very close and no significant gain in efficiency was attributed to the spectral differences.

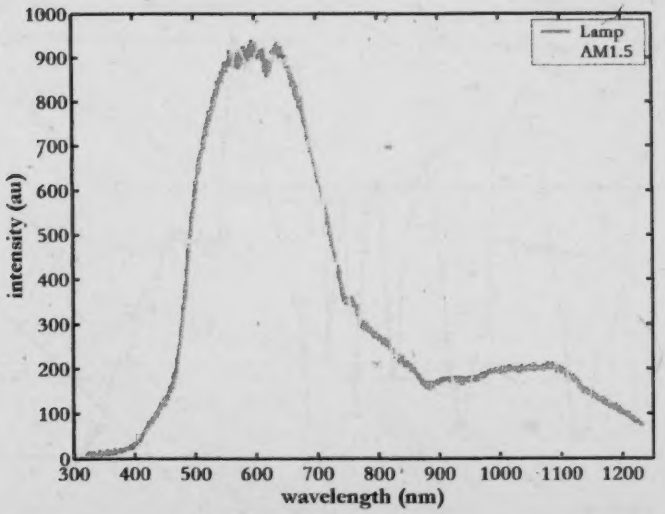


**Figure 4.9: Comparison of spectra of standard AM 1.5 and tungsten bulb. The AM 1.5 spectrum has been normalized to the maximum value of the lamp spectrum.**

$$O = \frac{\int_{\lambda_{min}}^{\lambda_{max}} Absorption(\lambda) \bullet I(\lambda) d\lambda}{\int_{\lambda_{min}}^{\lambda_{max}} I(\lambda) d\lambda} \qquad \textbf{Eq. 4.5a}$$

Instead, the poor performance of the devices was attributed to the low intensity of the source. The photocurrent action spectra of the dyes have been found to be intensity dependent [129]. At both low and high intensities, the incident photon to current conversion efficiency (IPCE) has been found to decrease across all wavelengths. This means that illumination at standard intensity will cause more electrons to be collected for every incident photon than illumination at low and high intensities. In these experiments, the intensity of the lamp is slightly higher than one fifth of the intensity at which standard measurements are made. Measurements made by Trupke et al. show that there is a significant drop off in IPCE when the monochromatic incident light intensity is less than 11 $mW/cm^2$, with a slight decline occurring well before this. Although this may not relate directly to broadband illumination, it is an indicator that the conversion efficiencies of the cells may be higher at the standard illumination of 100 $mW/cm^2$ than at the comparatively low value of 22.8 $mW/cm^2$.

### 4.5.2 Substrate

A problem that was initially overlooked was the temperature stability of the $In_2O_3$:Sn coated glass substrates. Because the annealing temperature was below the glass transition point, it was assumed that annealing would have no effect on the substrate. In fact, the indium doped tin (IV) oxide layer is extremely sensitive to annealing. When a bare piece of $In_2O_3$:Sn coated glass was annealed, under the same conditions as the films, and subsequently measured by four point probe, the sheet resistance was found to increase to 54.6 Ω/square from the pre-annealing value of 10.3 Ω/square. This introduced a significant series resistance to the equivalent circuit that would result in decreased performance when compared with an identical film on an unannealed substrate.

The change in optical transmission was also investigated using the double beam spectrophotometer with air used as the baseline. As can be seen in Figure 4.10, although the transmission of the annealed sample was similar to the as-delivered sample, it was somewhat less transmissive than the as-delivered $In_2O_3$:Sn coated glass between 350 - 523 nm and 685 – 800 nm. Particularly at the short wavelength end of the spectrum, where the dye is most absorptive, this results in a loss of input power to the cell that should be avoided if possible.

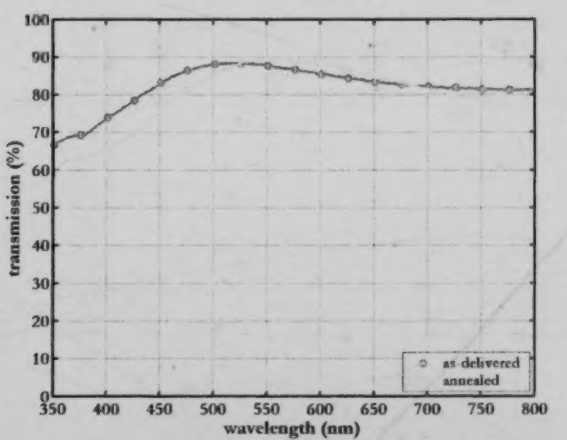


**Figure 4.10: Comparison of transmission spectra of as-delivered and annealed $In_2O_3$:Sn coated glass showing decreased transmission at small wavelengths with annealing.**

In an attempt to avoid these undesirable effects of the annealing process, three alternative annealing procedures were explored. First, the $In_2O_3$:Sn substrates were annealed until their

sheet resistances as measured by four point probe began to change substantially. Once this point was identified, samples of film were annealed under these maximum conditions. After annealing, the samples were examined by x-ray diffraction and TEM to determine whether the annealing was sufficient to cause the transition from amorphous to anatase.

The three alternative methods of annealing attempted were reduced thermal annealing, argon plasma annealing, and ultraviolet annealing. The reduced thermal annealing was found to significantly increase the sheet resistance of the $In_2O_3$:Sn regardless of the length of time or temperatures used. The minimal annealing time was considered to be that required for sintering of the nanocrystalline particles: 450°C for 30 minutes. After annealing under these conditions in the Thermolyne 48000 muffle furnace, the sheet resistance was still found to increase to 42.1 Ω/square. Minimal thermal annealing was abandoned due to this increase, and instead the ability of the structures to withstand increased annealing was explored by annealing for 5 hours at 600°C. The argon plasma annealing was carried out in a μEtch reactive ion etcher (RIE) with a base pressure of 0.67 Pa. Argon gas was flowed into the chamber at a rate of 40 sccm, resulting in a process pressure of 6.27 Pa when the plasma was lit with 75 W of RF power. When annealed under these conditions for 1 hour, there was no visible change in the appearance of the $In_2O_3$:Sn coated glass and the sheet resistance increased only to 14.3 Ω/square. Ultraviolet annealing was carried out in a Loctite UV curing furnace. After annealing for a total of 72 hours, the sheet resistance of the $In_2O_3$:Sn coated glass was found to have increased to 10.6 Ω/square and no visible changes were seen.

Pieces of sample C on silicon were then annealed under these annealing conditions. The increased thermal annealing was found to cause similar crystallization as the prolonged annealing. Polycrystalline anatase titanium dioxide, with features similar to those caused by the standard annealing process, was in evidence in both the XRD spectrum, Figure 4.11, and the TEM images and diffraction patterns, Figure 4.12 a) and 4.13 respectively. The dark field images of this sample showed evidence of crystallite growth, with some of the crystallites extending through large portions of the columns. The argon plasma annealing was found to cause significantly less crystallization than the thermal annealing. In the XRD spectrum, only a single weak peak in the (211) orientation was in evidence. The electron

diffraction analysis carried out in the TEM revealed only a diffuse amorphous diffraction pattern. A bare silicon wafer was then run in the XRD to determine if the (211) peak was actually a substrate peak. This test confirmed the presence of a substrate peak around 55° and thus the XRD analysis agreed with the TEM analysis in identifying the titanium dioxide as amorphous. The argon plasma annealing did appear to have modified the structure of the films. When viewed with the TEM, the feathery structure appeared to have collapsed only on the tops and a single side of the columns. This effect is difficult to see in the published Figure 4.12 b). It is proposed that the modified surfaces were the sides facing up, towards the incoming ions. The structural modification was thus a result of resputtering, rather than an annealing effect. The UV annealing appeared to have the least impact of any annealing method attempted. The XRD spectrum continued to show only the substrate peak, while the TEM analysis produced an amorphous diffraction pattern with no structural modification evident in the bright field images, Figure 4.12 c).

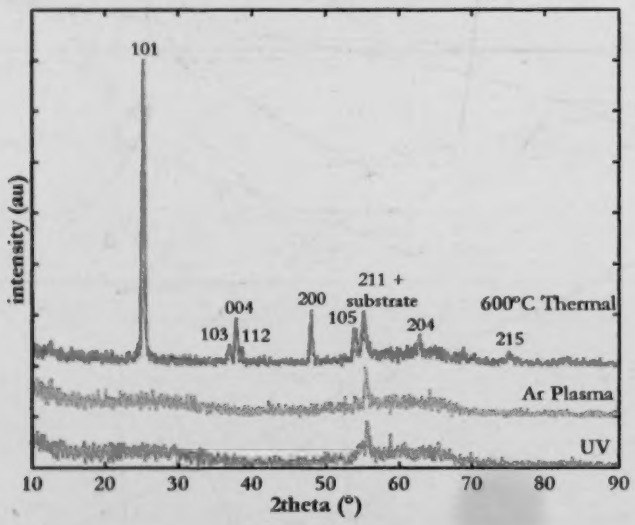


**Figure 4.11: XRD spectra of alternatively annealed samples as labeled on figure.**

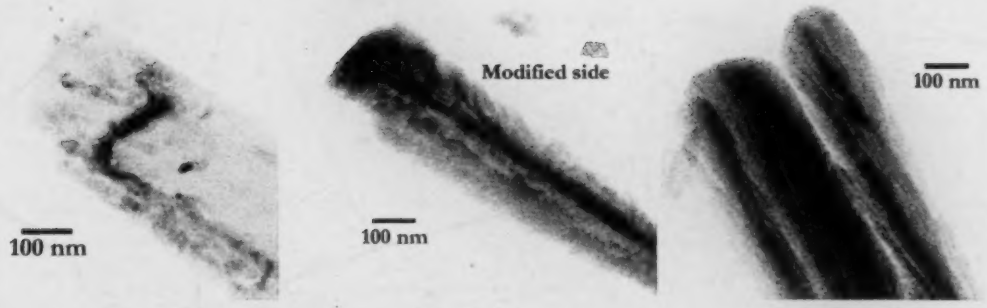


a) b) c)

**Figure 4.12: Bright field TEM images of sample C a) 600°C thermally annealed, b) argon plasma annealed, and c) UV annealed. The thermally annealed sample appeared very similar to previously thermally annealed samples with collapsed feathery microstructure. The plasma annealed sample had a modified structure on only one side that is attributed to resputtering. The UV annealed sample appeared to have no structural modification.**

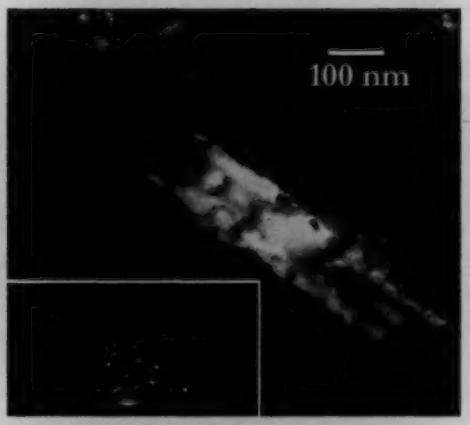


**Figure 4.13: Dark field TEM showing the growth of the individual crystallites with increased annealing. Inset is the polycrystalline diffraction pattern.**

From these results, it was concluded that none of the annealing methods explored here would have significant impact upon the performance of the solar cell devices. The reduced thermal annealing, while achieving the desired effects upon the film, was found to raise the sheet resistance of the $In_2O_3$:Sn to a value approaching that of the prolonged annealing. Neither plasma nor UV annealing was found to have the crystallization effects desired.

From this, it was concluded than an alternate substrate, one with better temperature stability, must be used.

### 4.5.3 Adsorbed water

As already mentioned, the presence of water within dye sensitized solar cells significantly degrades the performance of the cells by preventing the adsorption, or causing the desorption, of dye molecules. In the assembly of both generation I and II devices, efforts were undertaken to ensure that none of the cell components came into contact with liquid water, however no measures were implemented to prevent the adsorption of water vapour from the atmosphere. Because of the porous nature of these films and the high surface areas involved, this is likely to have played a role in the poor performance of the devices.

Before the next generation of devices was constructed, these issues had to be addressed.

# 5 Chapter 5: Generation III Devices: Improved Cells

In an attempt to achieve the best possible results, improvement upon generation II devices proceeded in a number of areas. The substrates used had better temperature stability, the films deposited were thicker to improve the comparison with nanocrystalline particle films, the dye used had an improved overlap with both the AM 1.5 spectrum and the imperfect spectrum of light sources used, the construction procedure of the devices was improved upon, and the light source used emitted more strongly in the short wavelength end of the spectrum.

## 5.1 Fluorinated tin (IV) oxide glass

As identified in the previous chapter, the increase in sheet resistance of the $In_2O_3$:Sn coated glass was found to negatively affect device performance. Although alternative annealing methods were attempted, none were found to meet the requirements of the process. At this stage, fluorinated tin (IV) oxide ($SnO_2$:F) was chosen to be the transparent conducting oxide.

### 5.1.1 As-delivered

This doped oxide is known to have better temperature stability and improve the adhesion with titanium dioxide over $In_2O_3$:Sn [45, 130, 131]. The substrates used in this experiment were 2.5 cm x 2.5 cm, 2.2 mm thick sodalime glass coated with a fluorinated tin (IV) oxide layer from Solaronix SA, specified to have a resistance of 7 – 8 Ω/square. Examination with the SEM revealed the $SnO_2$:F layer to be 655 nm thick, shown in Figure 5.1. The rms surface roughness, calculated from the AFM map of Figure 5.2, was 14.3 nm. The actual sheet resistance of the $SnO_2$:F layer, measured by four-point probe was 5.63 Ω/square. Because of the less transparent conductive coating, the optical transmission of the glass, measured by the double beam spectrophotometer and plotted in Figure 5.4, was found to be significantly lower than the $In_2O_3$:Sn coated glass across the majority of the spectrum. This is not an issue common to all $SnO_2$:F coated glass and should not be considered as a material deficiency. The transparency of the conducting layer may be tailored by adjusting the composition.

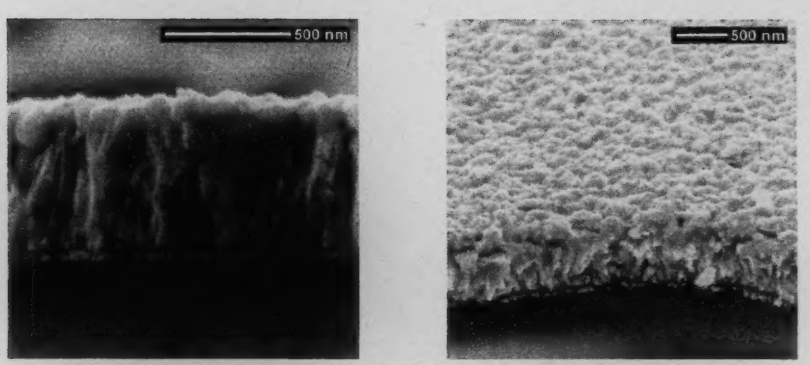


a) b)

**Figure 5.1: SEM images of as-delivered $SnO_2$:F coated glass.**

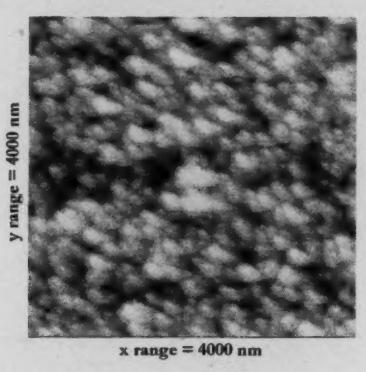


**Figure 5.2: AFM map of the $SnO_2$:F surface from which the roughness was calculated.**

### 5.1.2 Annealed

Due to the improved temperature stability of the $SnO_2$:F layer, it was decided to use an annealing procedure intermediate to the reduced and prolonged techniques described earlier. To examine the effects of this annealing on the $SnO_2$:F coated glass, a bare piece was subjected to annealing in air at 500°C for 3 hours. The substrate was then allowed to cool overnight and removed at a temperature of 23°C. The sheet resistance, measured by four-point probe, had increased to 9.13 Ω/square. Although this amounts to an increase of over 62% from the initial value, it remains below the initial sheet resistance of the $In_2O_3$:Sn coated glass used in the generation I devices. SEM imaging of the $SnO_2$:F layer, Figure 5.3, revealed that the top 190 nm of the $SnO_2$:F was modified significantly by the annealing. The transmission of the $SnO_2$:F coated glass across the majority of the visible spectrum, plotted in Figure 5.4, was found to improve slightly with annealing.

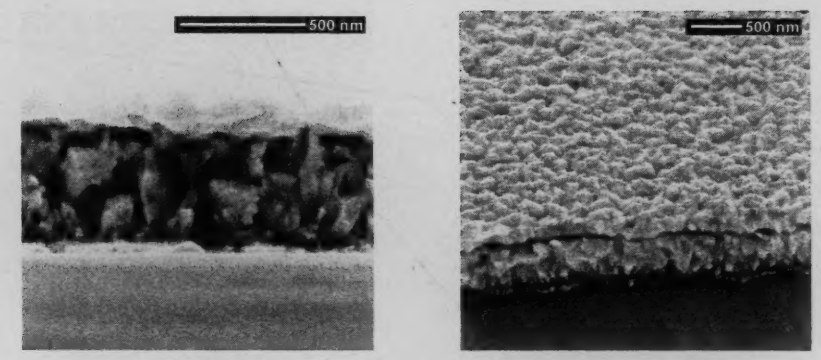


a) b)

**Figure 5.3: SEM images of annealed $SnO_2$:F coated glass. The annealing caused a change in the uppermost portions of the $SnO_2$:F layer that is visible in both the a) side and b) oblique SEM views.**

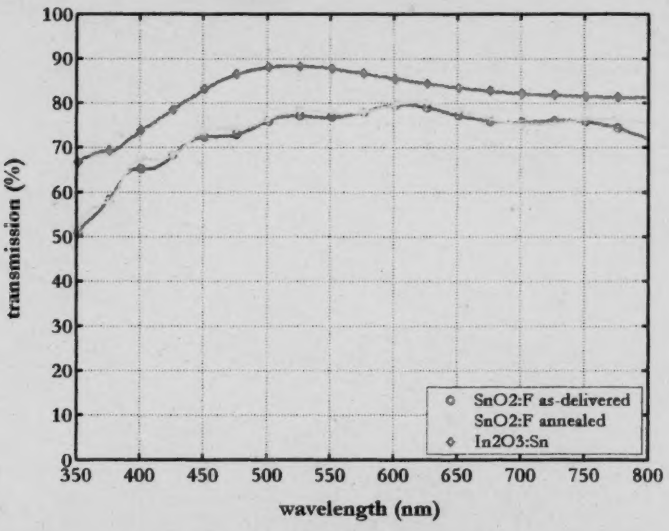


**Figure 5.4: Transmission of $SnO_2$:F coated glass, both as-delivered and annealed, and $In_2O_3$:Sn coated glass. Both $SnO_2$:F coated samples exhibit lower transmission than the $In_2O_3$:Sn coated glass.**

## 5.2 Films deposited

In order to produce films with improved current providing capabilities, thicker and denser films were deposited. Because no clear structure-type related trend could be identified in either generation I or II devices, all films for generation III devices were deposited as the

simplest structure, slanted columns, to allow for identification of other trends. The deposition angle was varied from 0° to 87° with programmed film thicknesses of 10 μm.

### 5.2.1 Deposition

After cleaning with Piranha (3:1 $H_2SO_4$:$H_2O_2$) solution, the $SnO_2$:F coated substrates and silicon witness wafers were placed in the same deposition system used previously. The chamber was evacuated to base pressures below 3.2 x $10^{-4}$ Pa by the diffusion pump. The deposition procedure followed that of the generation I samples, however due to the time required to deposit these significantly thicker films, the deposition rate, measured by the quartz crystal oscillator, was increased to between 14.5 and 15 Å/s by maintaining the beam current between 120 and 225 mA. Although it was desirable to increase the oxygen flow rate in order to maintain the stoichiometry of the deposited films at that of the generation I samples with the increased deposition rate, the decision was made to keep the chamber pressure at 7.3 x $10^{-3}$ Pa. It was feared further reduction of the mean free path of the flux might have negative effects on the GLAD structure.

The overall deposition proceeded in three cycles. Due to the thickness of the final films, the deposition was required to stop twice. At each stoppage, the crucible was refilled with fresh source material and the quartz crystal replaced. The chamber was then evacuated to base pressures below that of the first cycle before the next cycle commenced with conditioning of the melt.

The structures deposited were also modified slightly from the simple slanted column microstructure of the generation I devices. At the start of the deposition, a thin (~10 nm) dense film of titanium dioxide was deposited at normal incidence. This layer was intended to separate the electrolyte from the $SnO_2$:F to prevent recombination with electrons in the substrate. Once this layer had been deposited, the shutter was closed while the substrate holder was rotated to the deposition angle identified in Table 5.1. The shutter was opened and the deposition proceeded as before. All substrates were allowed to cool in a nitrogen ambient before removal.

With the thicker and denser samples, it was feared that thermal stresses might cause adhesion problems. None of the samples exhibited adhesion problems upon removal from the deposition system. After overnight storage, only the witness samples on silicon for sample H showed any signs of thermal stress. All samples on $SnO_2$:F coated glass were found to be adherent.

### 5.2.2 Annealing

One sample on $SnO_2$:F coated glass from each deposition was set aside for testing as-deposited, while another sample from a similar location on the substrate holder was taken for annealing. All samples on $SnO_2$:F coated glass were annealed at the same time to ensure identical annealing conditions. The annealing proceeded as for the bare $SnO_2$:F sample: annealed at 500°C for 3 hours and then cooled overnight before removal.

### 5.2.3 Scanning electron microscope analysis

SEM samples were prepared by cleaving the silicon witness samples at points corresponding to the midline of the $SnO_2$:F coated substrates and then mounting with conductive silver epoxy. At this point, samples on silicon were also taken for annealing from locations directly beside the SEM samples. It was hoped that this would eliminate the uncertainty in film thickness determination of the annealed samples. The silicon samples for annealing were annealed in the same way as the $SnO_2$:F based device samples and then mounted with conductive silver epoxy. Details of the resulting films, obtained from Figures 5.5 and 5.6, are given in Table 5.1

**Table 5.1**

| Sample | Deposition Angle (°) | Thickness (μm) | | Column Angle (°) | |
|---|---|---|---|---|---|
| | | As-deposited | Annealed | As-deposited | Annealed |
| H | 0 | 4.45 | 4.47 | 0 | 0 |
| I | 60 | 11.9 | 12.2 | 34 | 33 |
| J | 65 | 11.1 | 10.9 | 38 | 38 |
| K | 70 | 10.3 | 10.8 | 41 | 45 |
| L | 75 | 10.1 | 9.7 | 45 | 44 |
| M | 85 | 9.9 | 9.8 | 52 | 54 |
| N | 87 | 8.1 | 7.5 | 58 | 60 |

As noted in Chapter 3, there is a variation in thickness from the programmed values that is attributed to the uncertainty in the ratio of vertical film growth to vertical growth on the quartz crystal oscillator. This parameter is both angle and material sensitive. As this thesis presents the first detailed study of titanium dioxide films and includes angles not commonly used for GLAD growth, approximate ratios were used.

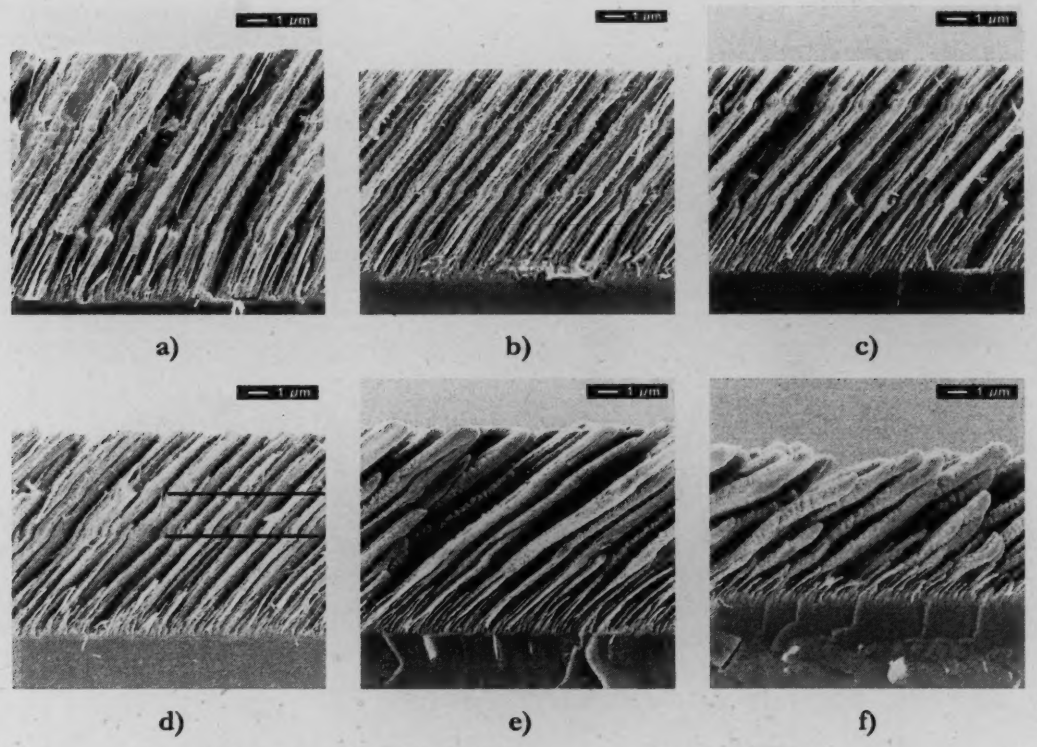


**Figure 5.5: Cross-sectional SEM images of samples a) I-a, b) J-a, c) K-a, d) L-a, e) M-a, and f) N-a. The increased column angle and porosity with increased deposition angle may be seen. SEM views of as-deposited samples appeared identical. The lines on sample L-a emphasize locations of vertical growth.**

The vertical growth at high oxygen pressures is clearly illustrated at three points in the films as seen in Figure 5.5. The first is at the base of the films, similar to those noted in Chapter 3. The other two points occur at varying vertical positions in the film, examples of which are indicated in Figure 5.5 d), depending upon the exact location that the depositions were paused for crystal replacement and crucible refilling. This phenomenon can therefore be explained by the high pressures present at the beginning of each cycle. The substrate holder was not moved to a protected position during the pauses in film growth; it was left at the

deposition angle specified. Also, it should be noted that although these points represent growth from essentially random flux, the GLAD structure is not completely filled in as can be seen from the top down images of the porous films.

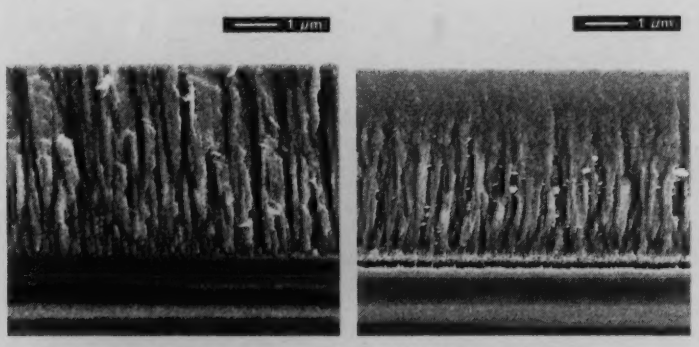


a) b)

**Figure 5.6: Cross-sectional SEM images of sample H a) as-deposited and b) annealed. Densification of the top third of the titanium dioxide layer was observed.**

Sample H, grown at 0° was the only sample to exhibit structural modification by annealing. As can be seen in Figure 5.6, the top third of the film changed from the typical columnar as-deposited film, to a very uniform and continuous layer with annealing. This layer blended into the columnar structure present closer to the substrate. Had annealing been allowed to continue, it is expected the entire film would appear uniform, with no columnar structure.

The top down images, shown in Figure 5.7, clearly demonstrate that the variation in porosity of these samples is quite large. In all of the films, the top SEM views show significantly enlarged structures when compared to images from samples A to G. This is a result of the broadening and competition that occur during film growth [85]. Despite the extinction and joining together of some columns, the overall density of the film has been found by simulation to remain essentially constant throughout the film [102]. That is, the density of the film has been shown to be a function of deposition angle only, not film thickness.

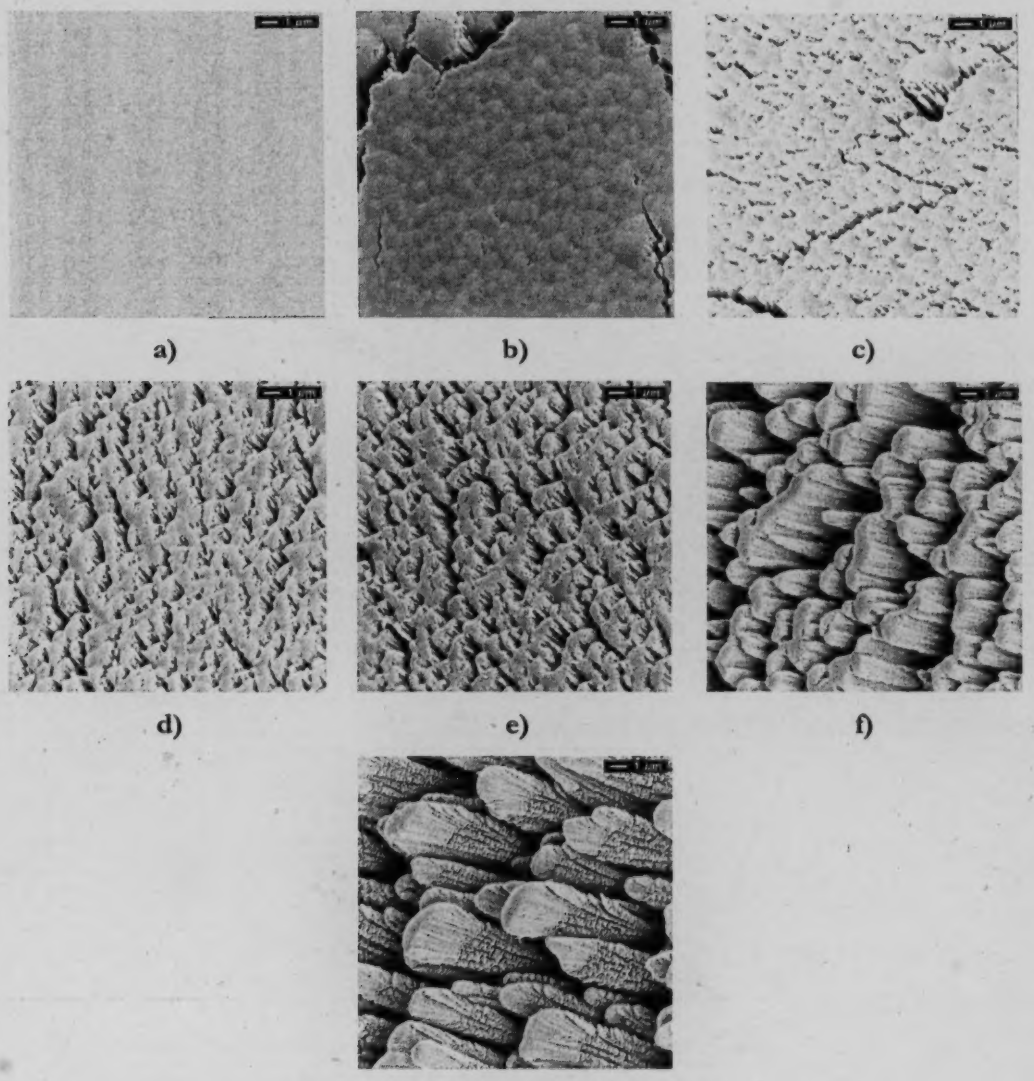


**Figure 5.7: Top down SEM images of samples a) H-a, b) I-a, c) J-a, d) K-a, e) L-a, f) M-a, and g) N-a showing increased porosity of films with increased deposition angle.**

From simulations, it has been seen that the surface area of similar films has a maximum in the range of 65° to 76° [132]. If the simulation was accurate and the current providing capabilities of the solar cells were highly sensitive to the number of adsorbed dye molecules, it would be expected that cells incorporating sample J, K, or L would produce the highest short circuit current densities.

### 5.2.4 Transmission electron microscope analysis

Transmission electron microscope samples were prepared and analyzed by the same technique described in Chapter 3.

Both the annealed and as-deposited films were found to possess similar characteristics as previous samples. Bright field images, an example of which is shown in Figure 5.8 a), of the as-deposited films showed the same feathery structure found in previous samples. Some full-length columns appear to have grown as a single entity throughout the film as shown in Figure 5.8 c). The diffuse electron diffraction patterns of the as-deposited films again show the amorphous nature of the as-deposited films. Bright field images of the annealed films, Figure 5.8 b), show that while some agglomeration of the feathery structure had occurred, it was not as complete as in previous samples. This was likely due to the reduced annealing time. Electron diffraction patterns from the annealed films were again found to be polycrystalline ring patterns indicating a polycrystalline anatase nature for the films. The dark field images, one of which is shown in Figure 5.9, show small crystallites in groups.

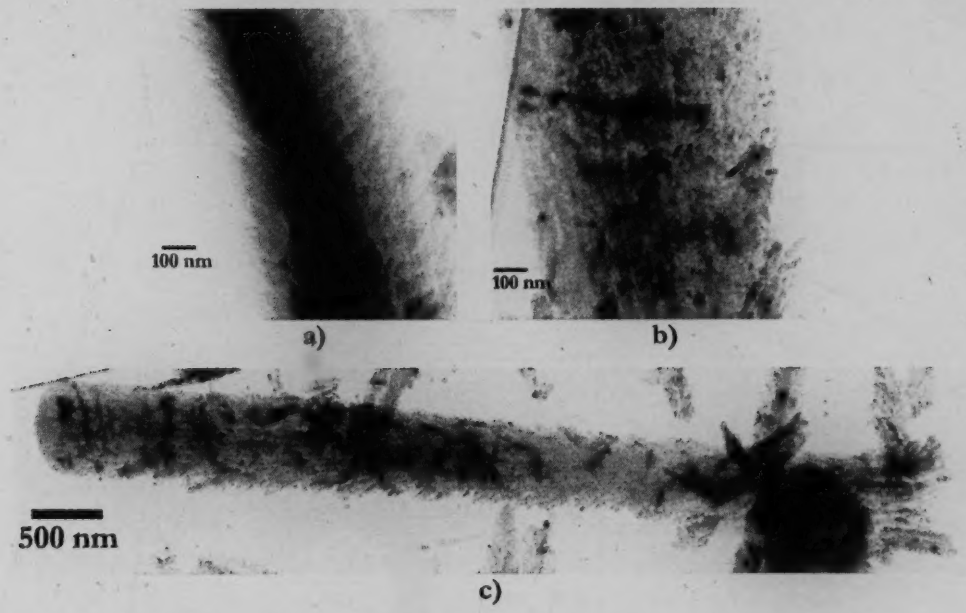


**Figure 5.8: Bright field TEM images of sample L a) as-deposited, b) annealed, and c) a full annealed post showing the collapse of the feathery structure, but to a lesser degree than was evident in Chapter 4.**

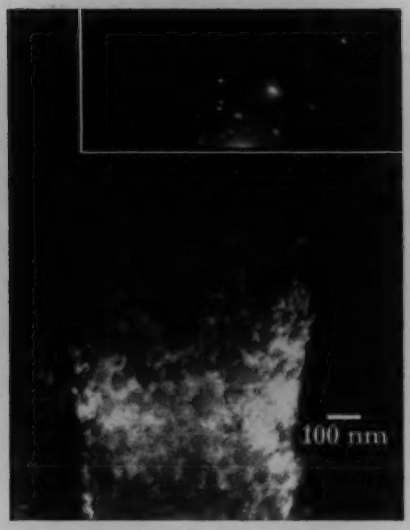


**Figure 5.9: Dark field TEM image showing part of the reflections from a single orientation. The diffraction pattern taken at lower magnification is shown inset.**

### 5.2.5 Optical transmission

Using the same method described before, and as-delivered or annealed $SnO_2$:F coated glass as appropriate for the baseline, the optical transmission spectra of the films were acquired. Due to the increased scattering and absorption in the thicker titanium dioxide films, the maximum transmission at any wavelength for an obliquely deposited film was found to be 8.4%. Two typical spectra, from samples I and I-a, are plotted in Figure 5.10 a). The normally deposited film of similar thickness, whose spectra is plotted in Figure 5.10 b), exhibited transmission greater that 55% for all wavelengths greater than 400 nm. This film is of similar composition, if anything it is more oxygen deficient, and should exhibit similar or greater absorption compared to the obliquely deposited films. Using the standard absorption equation, equation 5.2a [15], the difference in thickness can be shown to be insufficient to account for the entire difference in transmission. The optical loss is thus thought to be due primarily to scattering. If this is the case, this optical "loss" is actually a beneficial effect for light trapping. Though transmission through the cell is quite low, the light is not absorbed by the titanium dioxide, merely directed away from a straight line path.

$$I = I_o e^{-\alpha x} \qquad \textbf{Eq. 5.2a}$$

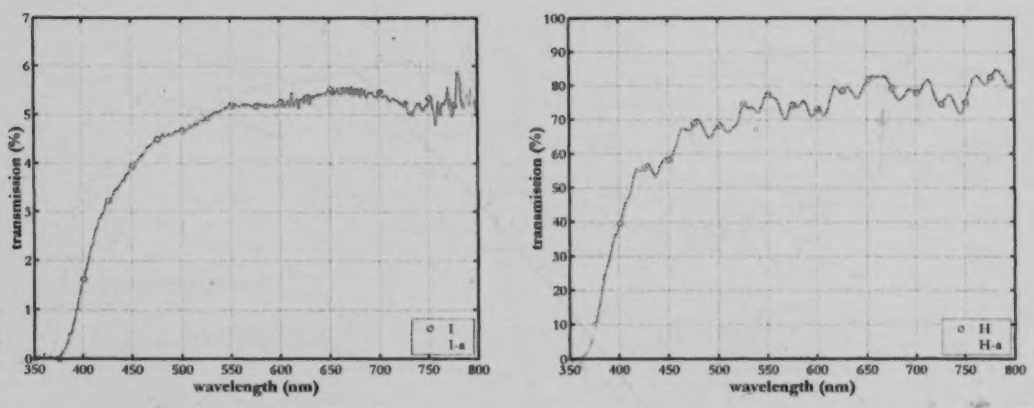


a) b)

**Figure 5.10: Optical transmission of as-deposited and annealed samples a) I and b) H.**

## 5.3 Dye sensitization

### 5.3.1 Dye

The dye chosen for the generation III devices was the improved "black" dye and was purchased from Solaronix SA. Designated Ruthenium 620-1H3TBA, the full chemical name of this dye is tris(isothiocyanato)-ruthenium(II)-2,2':6',2"-terpyridine-4,4',4"-tricarboxylic acid and its molar mass is 640.6 g/mol [133]. As purchased, the dye consisted of a fine black powder. In comparison with the Ru 535 TBA dye used in generation I and II devices, Ru 620 H3TBA has a strong absorption maximum at 620 nm, a region in which only the tail of the Ru 535 TBA absorption spectrum is present. Ru 620 H3TBA also absorbs out to a wavelength of 900 nm, resulting in a much broader range of light being absorbed as can be seen in Figure 5.11. The overlap integrals of the two dyes with the AM1.5 spectrum result in values of 0.23 are obtained for the Ru 535 TBA and 0.38 for the Ru 620 H3TBA. The change of dyes was thus expected to result in an increase in performance of 50 to 60% over cells utilizing Ru 535 TBA.

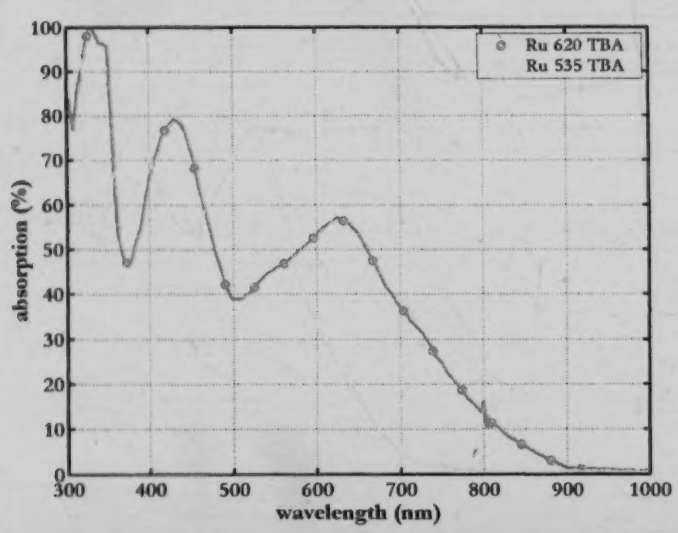


**Figure 5.11: Absorption spectra of Ru 620 H3TBA and Ru 535 TBA, showing increased absorption of Ru 620 H3TBA in the long wavelength end of the spectrum.**

### 5.3.2 Solution preparation

Solutions of Ru 620 H3TBA were made to the same approximate concentration as previous sensitizing solutions: 0.3 mM. To achieve this, a very similar procedure was used, except that 19.8 mg of dye solid were ultimately dissolved in 100 mL of 100% pure ethyl alcohol, resulting in a final solution concentration of 0.31 mM. This solution was a very dark green in colour, appearing almost black.

### 5.3.3 Sensitization

Sensitization was carried out in wide-mouthed transparent glass jars. Approximately 30 mL of dye solution was transferred into each of three jars. Before sensitization of the titanium dioxide films, they were heated to 100°C for 10 minutes in an Isotemp oven. The samples were allowed to cool briefly and placed into the dye solutions. This heating procedure was adopted in order to minimize adsorbed water within the films. It has repeatedly been shown that water causes near immediate desorption of similar dyes [134] and the extremely porous nature of these films and high humidity present during these experiments demanded that such a procedure be implemented. The samples were left immersed for over 22 hours in the dye. When removed, the samples were rinsed with 200 proof ethyl alcohol and dried with a variable temperature heat gun on low setting. The samples were left for 30 minutes to fully

dry. All samples were found to be stained dark green in colour, with variations in the darkness from sample to sample.

## 5.4 Device construction

The components used in these cells were similar to those used in the generation I and II devices. The counter electrodes used in these experiments were silicon wafers coated with a 10 nm titanium layer and a 50 nm platinum layer deposited by sputtering. The interelectrode spacers used were 150 μm thick microscope cover slips. The electrolyte used was Iodolyte TG 50 from Solaronix SA.

Device construction proceeded in exactly the same way for each device. In order to minimize the amount of water incorporated into the device, all components were heated with a variable temperature heat gun on medium low setting. The components were assembled while still warm by placing the spacers between the $SnO_2$:F coated glass and the platinum coated counter electrode and holding them together with binder clips. The electrolyte was then introduced into the interelectrode space by capillary action.

## 5.5 Device testing

### 5.5.1 Light source

The light source was identified as a problem after testing of the generation II devices. For most accurate measurements a solar simulator was desired, however the only solar simulator available had an output of 10 suns, an intensity that saturated the cells and caused the electrolyte to quickly evaporate. In order that measurements could be made, the output of an overhead projector with a 360 W 3M ENX projection lamp was used. The output spectrum of this source was characterized using the computer based Ocean Optics spectrometer and is plotted, along with the output spectrum of the tungsten bulb, in Figure 5.12. The projection lamp is seen to possess a slightly narrower peak than the tungsten bulb, with –3dB points at 481.4 nm and 661.4. The projection lamp also emits more strongly below 560 nm, the range in which the dye is most absorptive. The spectrometer indicated a significantly increased peak intensity with lower contribution from the infrared range. However, when measured by a calibrated pyro-electric meter placed at the position of the

test cells, the projector lamp was found to have an output of 9.35 mW/cm$^2$. This is approximately half the value indicated for the tungsten bulb, seemingly in disagreement with the spectrometer data. The light from the tungsten bulb is quite diffuse and a great deal of it will lie outside the relatively small collection angle of the optical fibre input of the spectrometer. The output of the projection lamp is comparatively collimated and hence more light will be within the collection angle of the spectrometer fibre inputs. Examining the overlap integral of the projection lamp with the new dye spectrum, it was expected this source would produce improved results. The overlap integral of the Ru 620 H3TBA was calculated to 0.39 be with the tungsten bulb and 0.47 with the projection lamp.

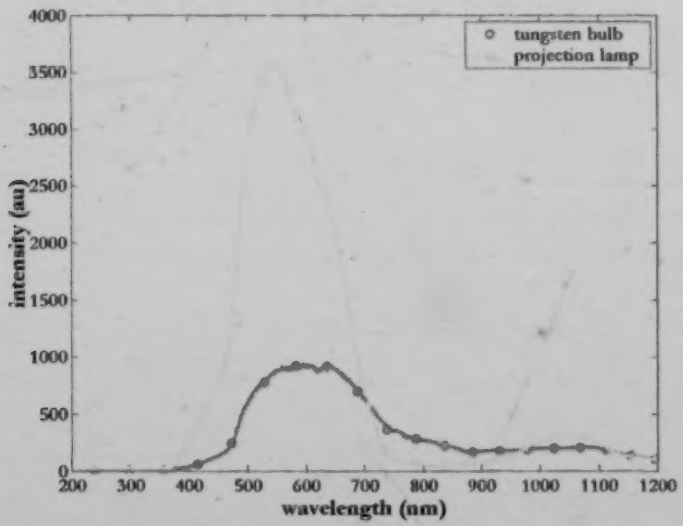


**Figure 5.12: Comparison of the output spectra of the tungsten bulb and projection lamp.**

### 5.5.2 Electrical measurements

The cells were measured using the same method as the generation I and II devices. All cells were permitted to equilibriate at open circuit conditions for 10 minutes before measurements began [67]. For confirmation of improved results with the new projection lamp light source, a mid-curve power point of sample H-a was measured with both sources. This brief experiment yielded an increase in the cell's output power with the projection lamp of 378% over the tungsten bulb. Based on the lower input power of the projection lamp, the measured efficiency under more appropriate illumination can be expected to increase by over 4 times.

A nanocrystalline particle film prepared on $SnO_2$:F coated glass was also included for reference. This sample was prepared using the second procedure presented in Chapter 4 with slow cooling and no pretreatment of the substrate. This sample was found to form a strongly adherent transparent layer and did not flake off during sintering. It was sensitized and incorporated into device Nano3 as described above.

### 5.5.3 Device performance

**Table 5.2**

| Sample | $V_{oc}$ (mV) | | $J_{sc}$ (mA/cm²) | | FF (%) | | Efficiency (%) | |
|---|---|---|---|---|---|---|---|---|
| | As-deposited | Annealed | As-deposited | Annealed | As-deposited | Annealed | As-deposited | Annealed |
| H | 221 | 635 | $4.85 \times 10^{-4}$ | 0.0245 | 30.1 | 19.6 | 0.000345 | 0.0326 |
| I | 353 | 567 | $4.22 \times 10^{-4}$ | 1.400 | 21.8 | 25.5 | 0.000347 | 2.17 |
| J | 358 | 604 | $4.19 \times 10^{-4}$ | 0.0959 | 21.3 | 18.2 | 0.000342 | 0.113 |
| K | 382 | 551 | $6.76 \times 10^{-3}$ | 1.37 | 63.9 | 23.8 | 0.0176 | 1.93 |
| L | 382 | 604 | $1.48 \times 10^{-3}$ | 1.32 | 43.7 | 24.3 | 0.00264 | 2.07 |
| M | 524 | 593 | $3.25 \times 10^{-3}$ | 0.350 | 24.3 | 24.0 | 0.00442 | 0.533 |
| N | 430 | 593 | $3.88 \times 10^{-3}$ | 0.241 | 63.3 | 23.7 | 0.0113 | 0.362 |
| Nano3 | 528 | --- | 0.708 | --- | 36.0 | --- | 1.44 | --- |

There is a great deal more scatter in this data than was found previously. This is believed to be due to the increased effects of all processes affecting electron transport in these significantly thicker films.

The significantly poorer performance in open circuit voltage and short circuit current density of the as-deposited samples as compared with the annealed samples or even previously tested samples is of note. This is believed to be due to the poorer stoichiometry of the films caused by the increased deposition rate. Using first order calculations, it can be shown that as-deposited samples will be highly oxygen deficient [105]. The behaviour of the samples likely begins to approach that of titanium, a metallic material into which the dye is incapable of injecting electrons. The annealing appears to have succeeded in promoting nearly full stoichiometry as the conduction band edge position, as indicated by the open circuit voltage, is similar to that in the titanium dioxide nanocrystalline particles.

When examining the open circuit voltages produced by the test cells, two main trends are visible. As just discussed, the annealing treatment succeeds in raising the open circuit

voltages attained by promoting the full oxidation of the film. The other trend is that the open circuit voltage of the as-deposited films generally increases with the deposition angle as shown in Figure 5.13. This is also likely explained by the stoichiometry being closer to full titanium dioxide. It is known that deposition at oblique angles results in more oxygen incorporation into the film, even with low deposition pressures and no addition of oxygen [103]. This is because of the reduced vertical growth rate of the film at oblique angles and the higher surface area for oxygen adsorption, and subsequent burial, presented by the porous films. This trend is eliminated by the annealing step, indicating that the annealing results in a similar oxygen content in the surface layer, into which the dye injects electrons, regardless of the oxygen content of the as-deposited samples.

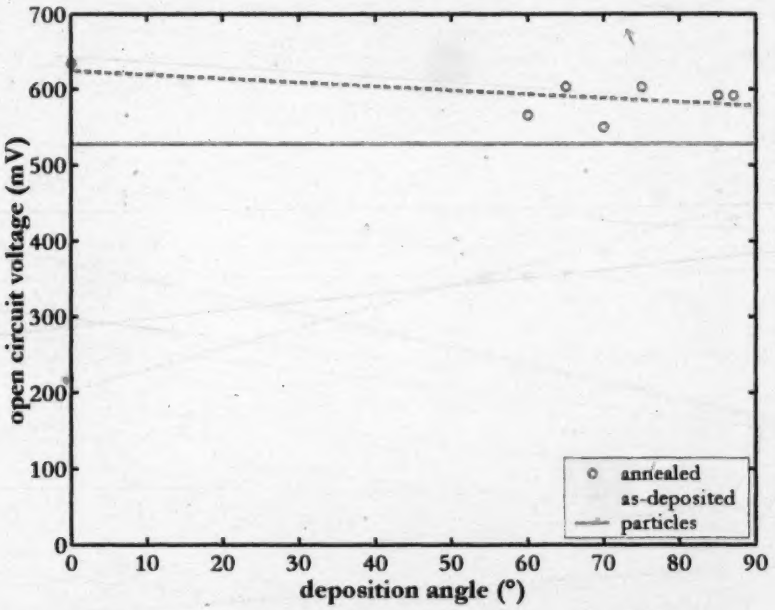


**Figure 5.13: Dependence of open circuit voltage on deposition angle.**

Two similar trends are seen in the short circuit current densities of cells. In all cases, the short circuit current density produced by the annealed sample was higher, the same trend observed in the improvement of generation II devices over generation I devices. This increase was by a factor of at least 50, with the greatest improvement by a factor of 3074 by sample I-a. Similar to the result found in Chapter 4, the samples whose as-deposited analogs generated smaller short circuit current densities were most likely to show larger improvements. Examining the short circuit current densities of the annealed samples,

plotted in Figure 5.14, it can also be seen that the current density improved as the films became more porous, reaching a maximum in the 60° to 70° range, before falling off again. This is in approximate agreement with the trend identified in the generation I devices, a maximum in accessible surface area that has been found in simulations [132], and a maximum in the surface area related photocatalytic activity of titanium dioxide found by others [135]. The belief that the amount of adsorbed dye is a critical parameter for current production is supported by this data. Although the adsorption experiment performed in previous chapters was not done here due to cost of materials, the assumption of higher surface area leading to increased adsorption seemed valid. The exception to this trend is sample J-a, which showed significantly poorer short circuit current densities. The anomaly of this sample is explained by an error in the deposition process for this film. During the first stage of the deposition of this sample, the oxygen feed was accidentally left tightly foiled. The result of this was that the oxygen flowed down between the feed tube and the foil, escaping near the base plate and pump port. Although the Bayard-Alpert gauge at the diffusion pump mouth indicated the same pressure, the oxygen pressure at the substrate was significantly reduced, resulting in a more oxygen deficient film. This error was corrected for the second and third stages of the deposition. The film produced thus had a thin layer of high oxide, resulting from the initial high pressures due to source material dissociation, followed by a significantly thicker (~3.7 μm) oxygen deficient layer, and finally a layer of the more standard oxide. This error was not noticeable in the open circuit voltage trends because of the oxygen rich layer close to the substrate, however when maximum current is drawn, the participation of the entire sensitized film is required. From these results, it seemed that the annealing process did not succeed in fully oxidizing the entire film. Although some oxidation clearly occurred because of the increased current density from the as-deposited sample, it is believed that the oxidation was not sufficient to promote full stoichiometry. It is expected that although not noticeable in sample J, this error also contributed to a lower than possible current density.

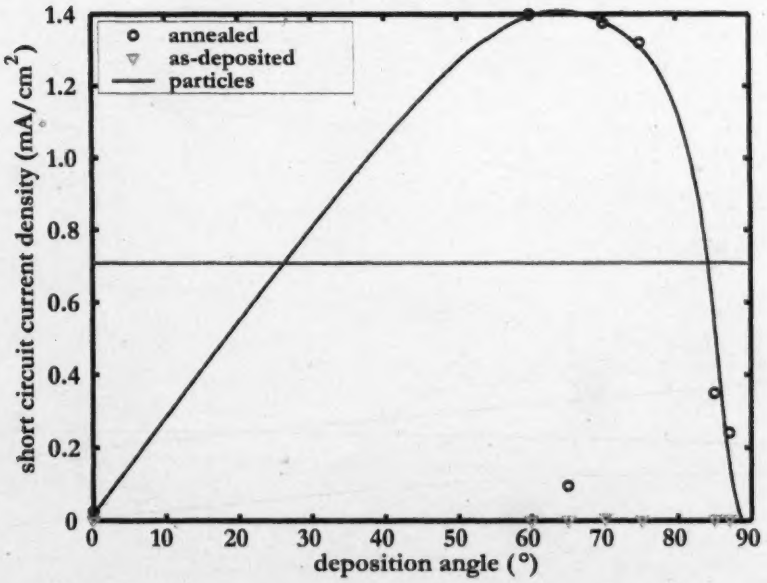


**Figure 5.14: Dependence of short circuit current density on deposition angle.**

The short circuit current densities found in the annealed samples were in the low end of reported values, but were a significant improvement over previous generation devices. Several factors contributed to this: the increased amount of adsorbed dye due to thicker films, removal of adsorbed water, and the increased film surface area due to closer column spacing at less oblique deposition angles, the improved conductivity of the substrate, and the increased source intensity in the range of wavelengths where the dye is most absorptive. Comparing samples M-a and N-a to their analogs from generation II devices, it can be seen that all of these factors led to an increase in short circuit current density of 5 to 14.5 times. Sample M-a, in particular showed increases in performance that could not be explained simply by the change of source.

The fill factor of the majority of cells examined in this study were much lower than those of the generation I and II devices. The cells incorporating annealed electron collecting layers in particular had fill factors mostly around 0.25, indicating nearly linear current-voltage characteristics.

The overall efficiencies of the cells were again found to be dominated by the trends in short circuit current density and current providing capabilities as can be seen in Figure 5.15. The efficiencies of the as-deposited samples were found to be significantly lower than those of either generation I or II devices for reasons discussed previously. The annealed samples produced efficiencies greater than any previously recorded for devices incorporating obliquely deposited electron collecting layers. The most efficient cell was found to include sample I-a and had an overall conversion efficiency of 2.17% resulting in a maximum power output of 0.61 mW for the 3 $cm^2$ device area. This sample, deposited at 60°, falls close to the previously stated range of maximum surface area. If not for the error in deposition, it is possible that sample J-a may have shown an efficiency slightly higher than this.

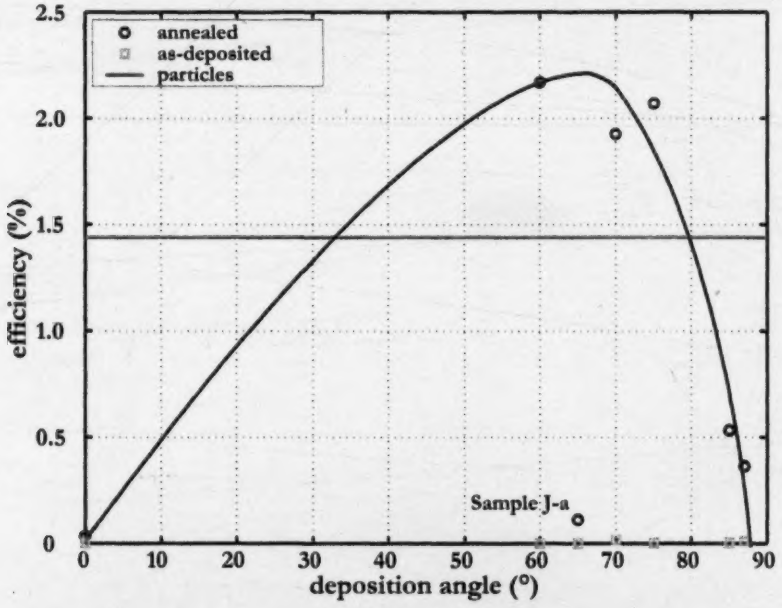


**Figure 5.15: Dependence of device efficiency on deposition angle, showing a maximum in the annealed samples between 60° and 75°.**

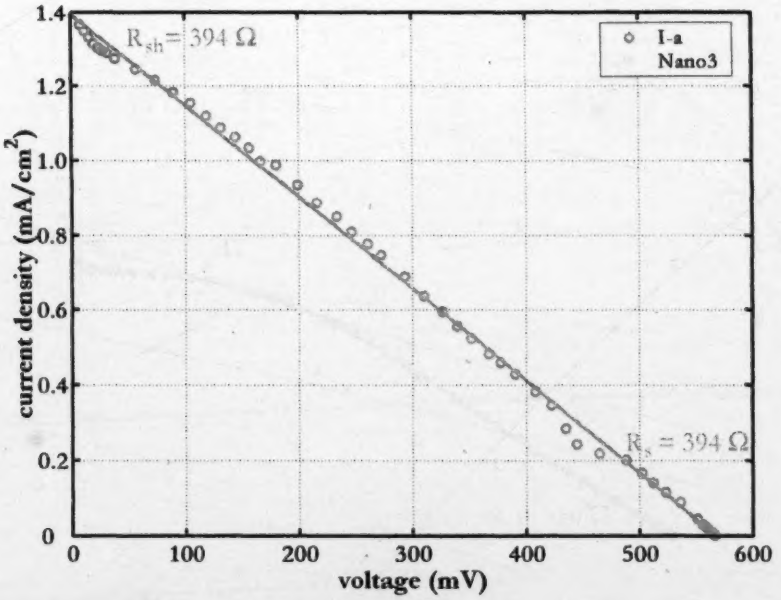


**Figure 5.16: Current-voltage characteristics of the best performing cell, incorporating sample I-a, and the cell incorporating the nanocrystalline particle layer.**

In comparison to the cell incorporating the standard nanocrystalline titanium dioxide particles as the electron collecting layer, several of the cells with obliquely deposited layers performed better. Although the particle based cell did not perform to the level reported in the literature [55], in particular in terms of current production, it is believed that this is due to the difference in counter electrode materials and test conditions. As such, this cell may be used for making comparisons between the performance of the electron collecting layers used in this study. Samples deposited obliquely in the range of 60° to 75°, with the exception previously noted, produced current densities in excess of 1.75 times that of the particle based layer. The current-voltage characteristics of sample I-a is compared against that of the nanocrystalline particles in Figure 5.16. Although the obliquely deposited samples produced fill factors lower than the particle based film, the improved current production capabilities were more than able to compensate. The source of this improvement is thought to be the increased accessibility of the obliquely deposited films to the electrolyte and improved connectivity within the film. As can be seen from the SEM images, the obliquely deposited layers present large, continuous pores into the film through which the electrolyte may penetrate into the more voided regions below any solid surface layer. The growth of

columns in oblique deposition results in a structure that is continuous from the top of the film to the substrate. While some columns may extinguish during growth, multiple columns may grow together, and new branches may split off existing columns, all of the film is directly connected in some manner to the substrate. As depicted in Figure 5.17, this leads to a direct path for electrons to follow to the substrate, reducing the transit time required and thus the amount of recombination that may occur as compared to the meandering path some electrons will travel as they percolate through the nanocrystalline particle film.

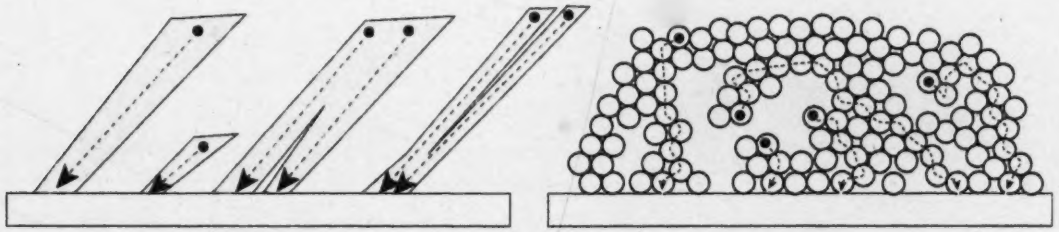

a) b)

**Figure 5.17: Diagram of electron paths in a) obliquely deposited and b) nanocrystalline particle films. The electron paths are seen to be significantly more direct in the obliquely deposited films for electrons injected far from the substrate.**

# 6 Chapter 6: Conclusions and Recommendations for Future Work

## 6.1 Conclusions

This thesis has presented the development of dye sensitized solar cells incorporating layers deposited by glancing angle deposition. Utilizing chemicals provided by Solaronix SA, the company holding the worldwide license for distributing the chemicals used in the most efficient reported cells, experiments were carried out with a variety of GLAD and obliquely deposited films. A number of trends were identified that will allow for future device optimization.

### 6.1.1 Crystallinity and composition

The constant trend throughout this thesis has been that cells incorporating annealed layers performed substantially better than cells incorporating otherwise identical as-deposited layers. The main source of this improvement is thought to be the transition from amorphous to anatase form caused by the annealing. This more structured form, with a well defined conduction band, allows for improved electron injection from excited dye molecules. This improved injection compensates for the loss in surface area available for absorption of dye molecules caused by the annealing.

While the annealing process is also believed to promote fully stoichiometric titanium dioxide, it did not have the ability to fully oxidize titanium oxide that is highly oxygen deficient. The addition of oxygen and the pressure at which the chamber is maintained during the deposition of the electron collecting layers are thus critical to fabricating high performance films.

### 6.1.2 Deposition angle and efficiency

The deposition angle was shown to play a critical role in determining the current producing capabilities of the devices. In both the generation I and III devices, the most efficient devices were found to incorporate films with the highest surface area. Measurements of the amount of dye adsorbed by the films of generation I devices showed that the higher surface

area of the films correlated to increased dye adsorption. The larger number of dye molecules provided for increased light absorption and subsequent electron injection into the film. Generation III devices, incorporating films deposited in a much larger range of angles, had efficiencies that corresponded to surface area trends calculated by simulation. The optimal range of deposition angle was shown to be in the range of 60° to 75°.

### 6.1.3 Best results

Testing of the generation III devices revealed performances comparable to a nanocrystalline particle based device tested under similar conditions. The most efficient device created had an overall conversion efficiency of 2.17%, an open circuit voltage of 567 mV, produced a short circuit current density of 1.30 mA/cm$^2$, and had a maximum output power of 0.61 mW for a device just over 3 cm$^2$ in area. This performance represented a 75% improvement over the efficiency of the cell based on nanocrystalline particles tested under the same conditions. These results, while still below the reported results for standard test conditions, show the promise of obliquely deposited films to produce improved dye sensitized solar cells.

## 6.2 Recommendations for Future Work

This study, while exploring a number of parameters, does require further work to allow concrete conclusions to be drawn and begs more studies to be done.

### 6.2.1 Standard testing

The most pressing area to be explored is the efficiency of the cells under standard test conditions. If, in fact, obliquely deposited films continue to produce efficiencies 75% higher than nanocrystalline particle films, this raises the ultimate efficiency to over 18%. While such a dramatic improvement upon a mature and well studied system is not to be expected, efficiencies comparable to the best reported values of conventional dye sensitized solar cells may certainly be within reach. Such standardized testing requires a solar simulator that closely approximates the AM 1.5 solar spectrum at an intensity of 100 mW/cm$^2$. Testing under these conditions will allow concrete comparisons with values reported in the literature.

### 6.2.2 Parameter variation

Although this thesis sought to explore a number of the parameters of interest, there remain several that are unexamined. One that came to light by error is the oxygen pressure near the substrate during the deposition. A single pressure was used throughout these experiments in order to maintain the assumptions of the GLAD process. While the negative effects of excessive pressure on the structure were seen in all generations of devices, the upper limit of oxygen pressure at which GLAD still functions was not determined. More fully stoichiometric titanium dioxide films were shown to result in improved solar cell performance, and as such this upper limit is worthy of exploration.

Another parameter of clear interest is the angle at which the deposition occurs. The range of 60° to 75° was identified to produce films resulting in the highest efficiencies. Although the width of this range points to the robustness of the technique to produce efficient cells, more precise experimentation with this parameter may allow the fabrication of more efficient devices.

The effect of thickness on the device performance was examined briefly in generation I devices and generation III devices assumed improved performance with thicker films. This parameter deserves greater attention as a maximum in device performance has been seen with nanocrystalline particle films of intermediate thickness and a similar effect is expected with these films.

### 6.2.3 Surface treatments

As mentioned in Chapter 2, it has been found that treatment of the titanium dioxide surface with agents to reduce recombination at the electrolyte/titanium dioxide interface leads to improved performance of cells. If similar device physics are present with GLAD layers, these treatments should also lead to improved performances and deserve study.

### 6.2.4 Stability

Because the cells tested in this thesis were not sealed, they were subject to drift over time as the electrolyte evaporated and was contaminated with water vapour. Hermetic sealing of the

cells would allow temporal and temperature stability studies to be performed. Stability is essential to the performance of real devices and should be examined.

### 6.2.5 Fundamental studies

The actual device physics have not been examined in this thesis. In order that more efficient cells be designed, knowledge of critical parameters must be obtained. Such studies include the determination of the time constants of electron injection from excited dye molecules by ultrafast fluorescence upconversion techniques, determination of the reaction kinetics at the electrolyte/titanium dioxide surface by standard electrochemical techniques, determination of the electron transport properties of the films by intensity modulated photocurrent spectroscopy, and determination of the incident photon to current conversion efficiency by monochromatic illumination experiments. There is a long list of physical properties to be explored, of which only the most common have been listed.

### 6.2.6 Light engineering

The true promise of glancing angle deposition is not in its ability to create highly porous structures, but in its ability to control the structure. Indeed, in this thesis the most efficient cells fabricated were made using simple oblique deposition, not the more complex processes normally associated with GLAD. It is envisioned that with appropriate structure choice, light trapping structures could be incorporated into the titanium dioxide films during deposition. Although the reflective counter electrode undoubtedly improves the efficiency over a transparent counter electrode, the electrolyte presents an absorptive medium that lessens the intensity of the reflected light. Thus some nature of light trapping structure would be beneficial.

An area identified in Chapter 2 may also be worth exploring. All reported values of efficiency have been obtained with an unmodified front TCO glass electrode. Anti-reflection coatings are a well known way of improving the light coupling into a device. With anti-reflection coatings, it is conceivable that the efficiency of either conventional, GLAD, or obliquely deposited based dye sensitized solar cells would be improved.

## 6.3 And finally

The thesis has shown the promise of GLAD and obliquely deposited films in the role of electron collecting layers of dye sensitized solar cells. Although a more complicated procedure than the currently used squeegee or screen printing techniques, GLAD offers the ability to tailor the structure in a simple and reproducible way. Benefit will be gained from more detailed studies of the physical mechanisms of both the GLAD growth process and the sensitized films.

## References


[1] A.E. Becquerel, "Recherches sur les effets de la radiation chimique de la lumiere solaire, au moyen des courants electriques," *Comte Rendus d'Academie des Sciences*, vol. 9, pp. 145, 1839.

[2] R.S. Ohl, "Light-sensitive device including silicon," US Patent No. 2,443,542, 27 May 1941.

[3] D.M. Chapin, C.S. Fuller, and G.L. Pearson, "A new silicon *p-n* junction photocell for converting solar radiation into electrical power," *Journal of Applied Physics*, vol. 25, pp. 676-677, 1954.

[4] B. O'Regan and M. Gratzel, "A low-cost, high-efficiency solar cell based on dye-sensitized colloidal $TiO_2$ films," *Nature*, vol. 353, pp. 737-740, 1991.

[5] K. Robbie and M.J. Brett, "Method of depositing shadow sculpted thin films," US Patent No. 5,866,204, 2 February, 1999.

[6] K. Robbie and M.J. Brett, "Glancing angle deposition of thin films," US Patent No. 6,206,065, 27 March, 2001.

[7] K. Robbie and M.J. Brett, "Shadow sculpted thin films," US Patent No. 6,248,422, 19 June, 2001.

[8] "AM 1.5 Solar Spectrum," ISO Standard 9845-1, 1992.

[9] M.A. Green, "Photovoltaic principles," *Physica E*, vol. 14, pp. 11-17, 2002.

[10] A. Goetzberger, "Optical confinement in thin Si-solar cells by diffuse back reflectors," presented at IEEE PVSC, Kissimmee, Florida, 1981.

[11] A. Goetzberger, C. Hebling, and H.-W. Schock, "Photovoltaic materials, history, status and outlook," *Materials Science and Engineering* R, vol. 40, pp. 1-46, 2003.

[12] M.A. Green, "Third generation photovoltaics: ultra-high conversion efficiency at low cost," *Progress in Photovoltaics: Research and Applications*, vol. 9, pp. 123-135, 2000.

[13] M.A. Green, "Silicon solar cells: evolutions, high-efficiency design and efficiency enhancements," *Semiconductor Science and Technology*, vol. 8, pp. 1-12, 1993.

[14] W. Shockley and H.J. Queisser, "Detailed balance limit of efficiency of *p-n* junction solar cells," *Journal of Applied Physics*, vol. 32, pp. 510, 1961.

[15] M. Born and E. Wolf, *Principles of optics: electromagnetic theory of propagation, interference and diffraction of light*, Fourth ed. London: Pergamon Press Ltd., 1970.

[16] S.H. Lee, I. Lee, and J. Yi, "Silicon nitride films prepared by high-density plasma chemical vapor deposition for solar cell applications," *Surface & Coatings Technology*, vol. 153, pp. 67-71, 2002.

[17] B.S. Richards, S.F. Rowlands, C.B. Honsberg, and J.E. Cotter, "$TiO_2$ DLAR coatings for planar silicon solar cells," *Progress in Photovoltaics: Research and Applications*, vol. 11, pp. 27-32, 2003.

[18] I. Lee, D.G. Lim, S.H. Lee, and J. Yi, "The effects of a double layer anti-reflection coating for a buried contact solar cell application," *Surface & Coatings Technology*, vol. 137, pp. 86-91, 2001.

[19] M.A. Green, J. Zhao, A. Wang, and S.R. Wenham, "Very high efficiency silicon solar cells - science and technology," *IEEE Transactions on Electron Devices*, vol. 46, pp. 1940-1947, 1999.

[20] S.K. Rotich, J.G. Smith, A.G.R. Evans, and A. Brunnschweiler, "Micromachined thin solar cells with a novel light trapping scheme," *Journal of Micromechanics and Microengineering*, vol. 8, pp. 134-137, 1998.

[21] J.E. Cotter, R.B. Hall, M.G. Mauk, and A.M. Barnett, "Light Trapping in Silicon-Film Solar Cells with Rear Pigmented Dielectric Reflectors," *Progress in Photovoltaics: Research and Applications*, vol. 7, pp. 261-274, 1999.

[22] P. Campbell and M.A. Green, "Light trapping properties of pyramidally textured surfaces," *Journal of Applied Physics*, vol. 62, pp. 243-249, 1987.

[23] Y. Bai, A.M. Barnett, J.A. Rand, and D.H. Ford, "Light-trapping and Back Surface Structures for Polycrystalline Silicon Solar Cells," *Progress in Photovoltaics: Research and Applications*, vol. 7, pp. 353-361, 1999.

[24] H.W. Deckman, C.R. Wronski, H. Witzke, and E. Yablonovitch, "Optically enhanced amorphous silicon solar cells," *Applied Physics Letters*, vol. 42, pp. 968-970, 1983.

[25] J.J. Loferski, "Tandem photovoltaic solar cells and increased solar energy conversion efficiency," presented at Twelfth IEEE Photovoltaic Specialists Conference, Baton Rouge, LA, 1976.

[26] A. Marti and G.L. Araujo, "Limiting efficiencies for photovoltaic energy conversion in multigap systems," *Solar Energy Materials and Solar Cells*, vol. 43, pp. 203-222, 1996.

[27] J.L. Gray and Y.J. Lee, "Numerical modeling of graded band gap CIGS solar cells," *1994 IEEE First World Conference on Photovoltaic Energy Conversion*, vol. 1, pp. 123-126, 1994.

[28] S.R. Wenham, J. Zhao, X. Dai, A. Wang, and M.A. Green, "Surface passivation in high efficiency silicon solar cells," *Solar Energy Materials and Solar Cells*, vol. 65, pp. 377-384, 2001.

[29] M.F. Stuckings and A.W. Blakers, "A study of shading and resistive loss from the fingers of encapsulated solar cells," *Solar Energy Materials and Solar Cells*, vol. 59, pp. 233-242, 1999.

[30] M.A. Green, K. Emery, D.L. King, S. Igari, and W. Warta, "Solar cell efficiency tables (version 21)," *Progress in Photovoltaics: Research and Applications*, vol. 11, pp. 39-45, 2003.

[31] J. Zhao, A. Wang, M. Green, and F. Ferrazza, "Novel 19.8% efficient 'Honeycomb' textured multicrystalline and 24.4% monocrystalline silicon solar cell," *Applied Physics Letters*, vol. 73, pp. 1991-1993, 1998.

[32] M.A. Contreras, B. Egaas, K. Ramanathan, J. Hiltner, A. Swartzlander, F. Hasoon, and R. Noufi, "Progress Toward 20% Efficiency in Cu(In,Ga)$Se_2$ Polycrystalline Thing-film Solar Cells," *Progress in Photovoltaics: Research and Applications*, vol. 7, pp. 311-316, 1999.

[33] M. Ohmori, T. Takamoto, E. Ikeda, and H. Kurita, "High efficiency InGaP/GaAs tandem solar cells," presented at International PVSEC-9, Miyasaki, Japan, 1996.

[34] J. Nelson, "Organic photovoltaic films," *Current Opinion in Solid State & Materials Science*, vol. 6, pp. 87-95, 2002.

[35] G. Yu, J. Gao, J.C. Hummelen, F. Wudl, and A.J. Heeger, "Enhanced efficiencies via a network of internal donor-acceptor heterojunctions," *Science*, vol. 270, pp. 1789-1791, 1995.

[36] J.H. Schon, C. Kloc, and B. Batlogg, "Pentacene based photovoltaic devices," *Synthetic Metals*, vol. 124, pp. 95-97, 2001.

[37] M. Gratzel, "Perspectives for dye-sensitized nanocrystalline solar cells," *Progress in Photovoltaics: Research and Applications*, vol. 8, pp. 171-185, 2000.

[38] A. Zaban, S. Ferrere, and B. Gregg, "Relative energetics at the semiconductor/sensitizing dye/electrolyte interface," *Journal of Physical Chemistry B*, vol. 102, pp. 452-460, 1998.

[39] T. Hannappel, B. Burfeindt, W. Storck, and F. Willig, "Measurement of ultrafastphotoinduced Electron transfer from chemically anchored Ru-dye molecules into empty electronic states in a colloidal anatase $TiO_2$ film," *Journal of Physical Chemistry B*, vol. 101, pp. 6799-6802, 1997.

[40] N.J. Cherepy, G.P. Smestad, M. Gratzel, and J.Z. Zhang, "Ultrafast electron injection: implications for a photoelectrochemical cell utilizing an anthocyanin dye-sensitized $TiO_2$ nanocrystalline electrode," *Journal of Physical Chemistry B*, vol. 101, pp. 9342-9351, 1997.

[41] L. Kronik, N. Bachrach-Ashkenasy, M. Leibovich, E. Fefer, Y. Shapira, S. Gorer, and G. Hodes, "Surface states and photovoltaic effects in CdSe quantum dot films," *Journal of the Electrochemical Society*, vol. 145, pp. 1748-1755, 1998.

[42] L. Brus, "Model for carrier dynamics and photoluminescence quenching in wet and dry porous silicon thin films," *Physical Review B (Condensed Matter)*, vol. 53, pp. 4649-4656, 1996.

[43] R. Konenkamp, R. Henninger, and P. Hoyer, "Photocarrier transport in colloidal $TiO_2$ films," *Journal of Physical Chemistry*, vol. 97, pp. 7328-7330, 1993.

[44] H. van 't Spijker and A. Goossens, "Quantitative study of electron transport in nanostructured materials by means of transient absorption spectroscopy.," *Thin Solid Films*, vol. 403-404, pp. 410-414, 2002.

[45] F. Pichot and B.A. Gregg, "The photovoltage-determining mechanism in dye-sensitized solar cells," *Journal of Physical Chemistry B*, vol. 104, pp. 6-10, 2000.

[46] D. Cahen, G. Hodes, M. Gratzel, J.F. Guillemoles, and I. Riess, "Nature of photovoltaic action in dye-sensitized solar cells," *Journal of Physical Chemistry B*, vol. 104, pp. 2053-2059, 2000.

[47] S.A. Haque, Y. Tachibana, R.L. Willis, J.E. Moser, M. Gratzel, D.R. Klug, and J.R. Durrant, "Parameters influencing charge recombination kinetics in dye-sensitized nanocrystalline titanium dioxide films," *Journal of Physical Chemistry B*, vol. 104, pp. 538-547, 2000.

[48] B. O'Regan, J. Moser, M. Anderson, and M. Gratzel, "Vectorial electron injection into transparent semiconductor membranes and electric field effects on the dynamics of light-induced charge separation," *Journal of Physical Chemistry*, vol. 94, pp. 8720-8726, 1990.

[49] S.Y. Huang, G. Schlichthorl, A.J. Nozik, M. Gratzel, and A.J. Frank, "Charge recombination in dye-sensitized nanocrystalline $TiO_2$ solar cells," *Journal of Physical Chemistry B*, vol. 101, pp. 2576-2582, 1997.

[50] A. Hagfeldt and M. Gratzel, "Molecular photovoltaics," *Accounts of Chemical Research*, vol. 33, pp. 269-277, 2000.

[51] M.K. Nazeeruddin, A. Kay, I. Rodicio, R. Humphry-Baker, E. Muller, P. Liska, N. Vlachopoulos, and M. Gratzel, "Conversion of light toelectricity by *cis*-$X_2$Bis(2,2'-bipyridyl-4,4'-dicarboxylate)ruthenium(II) charge-transfer sensitizers (X = $Cl^-$, $Br^-$, $I^-$, $CN^-$, and $SCN^-$) on nanocrystalline $TiO_2$ electrodes," *Journal of the American Chemical Society*, vol. 115, pp. 6382-6390, 1993.

[52] M.K. Nazeeruddin, S.M. Zakeeruddin, R. Humphry-Baker, M. Jirousek, P. Liska, N. Vlachopoulos, V. Shklover, C.-H. Fischer, and M. Gratzel, "Acid-base equilibria of (2,2'-Bipyridyl-4,4'-dicarboxylic acid)ruthenium(II) complexes and the effect of

protonation on charge-transfer sensitization of nanocrystalline titania," *Inorganic Chemistry*, vol. 38, pp. 6298-6305, 1999.

[53] S.M. Zakeeruddin, M.K. Nazeeruddin, R. Humphry-Baker, and M. Gratzel, "Stepwise assembly of tris-heteroleptic polypyridyl complexes of ruthenium(II)," *Inorganic Chemistry*, vol. 37, pp. 5251-5259, 1998.

[54] S.M. Zakeeruddin, M.K. Nazeeruddin, R. Humphry-Baker, P. Pechy, P. Quagliotto, C. Barolo, G. Viscardi, and M. Gratzel, "Design, synthesis, and application of amphiphilic ruthenium polypyridyl photosensitizers in solar cells based on nanocrystalline $TiO_2$ films," *Langmuir*, vol. 18, pp. 952-954, 2002.

[55] M.K. Nazeeruddin, P. Pechy, and M. Gratzel, "Efficient panchromatic sensitization of nanocrystalline $TiO_2$ films by a black dye based on a trithiocyanato-ruthenium complex," *Chemical Communications*, vol. 18, pp. 1705-1706, 1997.

[56] K. Tennakone, G.K.R. Senadeera, and P.V.V. Jayaweera, "Enhancement of the energy and quantum conversion efficiencies of a photoelectro-chemical cell sensitized with a combination of cationic and anionic dyes," *Current Science*, vol. 81, pp. 76-77, 2001.

[57] H. Rensmo, K. Keis, H. Lindstrom, S. Sodergren, A. Solbrand, A. Hagfeldt, and S.-E. Lindquist, "High light-to-energy conversion efficiencies for solar cells based on nanostructured ZnO electrodes," *Journal of Physical Chemistry B*, vol. 101, pp. 2598-2601, 1997.

[58] I. Bedja, S. Hotchandani, and P.V. Kamat, "Preparation and photoelectrochemical characterization of thin $SnO_2$ nanocrystalline semiconductor films and their sensitization with bis(2,2'-bipyridine)(2,2'-bipyridine-4,4'-dicarboxylic acid)ruthenium(II) complex," *Journal of Physical Chemistry*, vol. 98, pp. 4133-4140, 1994.

[59] M.G. Wheatley, M.P. Brungs, R.P. Chaplin, and E. Sizgek, "Study of reactive magnetron sputtered titanium dioxide films for use in the gratzel photoelectrochemical cell," *Journal of the Australian Ceramic Society*, vol. 37, pp. 27-34, 2001.

[60] M.M. Gomez, J. Lu, J.L. Solis, E. Olsson, A. Hagfeldt, and C.G. Granqvist, "Dye-sensitized nanocrystalline titanium-oxide-based solar cells prepared by sputtering: influence of the substrate temperature during deposition," *Journal of Physical Chemistry B*, vol. 104, pp. 8712-8718, 2000.

[61] M. Okuya, K. Nakade, and S. Kaneko, "Porous $TiO_2$ thin films synthesized by a spray pyrolysis deposition (SPD) technique and their application to dye-sensitized solar cells," *Solar Energy Materials & Solar Cells*, vol. 70, pp. 425-435, 2002.

[62] N.-G. Park, G. Schlichthorl, J. van de Lagemaat, H.M. Cheong, A. Mascarenhas, and A.J. Frank, "Dye-sensitized $TiO_2$ solar cells: structural and photoelectrochemical

characterization of nanocrystalline electrodes formed from the hydrolysis of $TiCl_4$," *Journal of Physical Chemistry B*, vol. 103, pp. 3308-3314, 1999.

[63] M.M. Gomez, J. Lu, E. Olsson, A. Hagfeldt, and C.G. Granqvist, "High efficiency dye-sensitized nanocrystalline solar cells based on sputter deposited Ti oxide films," *Solar Energy Materials & Solar Cells*, vol. 64, pp. 385-392, 2000.

[64] T.-S. Kang, K.-H. Chun, J.S. Hong, S.-H. Moon, and K.-J. Kim, "Enhanced stability of photocurrent-voltage curves in Ru(II)-dye-sensitized nanocrystalline $TiO_2$ electrodes with carboxylic acids," *Journal of the Electrochemical Society*, vol. 147, pp. 3049-3053, 2000.

[65] B.A. Gregg, F. Pichot, S. Ferrere, and C.L. Fields, "Interfacial recombination processes in dye-sensitized solar cells and methods to passivate the interfaces," *Journal of Physical Chemistry B*, vol. 105, pp. 1422-1429, 2001.

[66] J.S. Hong, M. Joo, R. Vittal, and K.-J. Kim, "Improved photocurrent-voltage characteristics of Ru(II)-dye sensitized solar cells with polypyrrole-anchored $TiO_2$ films," *Journal of the Electrochemical Society*, vol. 149, pp. E493-E495, 2002.

[67] S. Ferrere and B.A. Gregg, "Large increases in photocurrents and solar conversion efficiencies by UV illumination of dye sensitized solar cells," *Journal of Physical Chemistry B*, vol. 105, pp. 7602-7605, 2001.

[68] U. Bach, D. Lupo, P. Comte, J.E. Moser, F. Weissortel, J. Salbeck, H. Spreitzer, and M. Gratzel, "Solid-state dye-sensitized mesoporous $TiO_2$ solar cells with high photon-to-electron conversion efficiencies," *Nature*, vol. 395, pp. 583-585, 1998.

[69] K. Hara, T. Horiguchi, T. Kinoshita, K. Sayama, H. Sugihara, and H. Arakawa, "Highly efficient photon-to-electron conversino with mercurochrome-sensitized nanoporous oxide semiconductor solar cells," *Solar Energy Materials & Solar Cells*, vol. 64, pp. 115-134, 2000.

[70] G.R.R.A. Kumara, A. Konno, G.K.R. Senadeera, P.V.V. Jayaweera, D.B.R.A. De Silva, and K. Tennakone, "Dye-sensitized solar cell with the hole collector p-CuSCN deposited from a solution in n-propyl sulphide," *Solar Energy Materials & Solar Cells*, vol. 69, pp. 195-199, 2001.

[71] M.K. Nazeeruddin, P. Pechy, T. Renouard, S.M. Zakeeruddin, R. Humphry-Baker, P. Comte, P. Liska, L. Cevey, E. Costa, V. Shklover, L. Spiccia, G.B. Deacon, C.A. Bignozzi, and M. Gratzel, "Engineering of efficient panchromatic sensitizers for nanocrystalline $TiO_2$-based solar cells," *Journal of the American Chemical Society*, vol. 123, pp. 1613-1624, 2001.

[72] A. Hinsch, J. Kroon, K. Rainer, R. Sasrawan, A. Meyer, and I. Uhlendorf, "Long-term stability and efficiency of dye-sensitized solar cells," presented at 17th European Photovoltaic Solar Energy Conference, Munich, Germany, 2001.

[73] K. Robbie, M.J. Brett, and A. Lakhtakia, "Chiral sculptured thin films," *Nature*, vol. 384, pp. 616-616, 1996.

[74] J.M. Nieuwenhuizen and H.B. Haanstra, "Microfractography of thin films," *Philips Technical Review*, vol. 27, pp. 87, 1966.

[75] R.N. Tait, T. Smy, and M.J. Brett, "Modeling and characterization of columnar growth in evaporated-films," *Thin Solid Films*, vol. 226, pp. 196-201, 1993.

[76] K. Robbie, M.J. Brett, and A. Lakhtakia, "First thin film realization of a helicoidal bianisotropic medium," *Journal of Vacuum Science and Technology A*, vol. 13, pp. 2991-2993, 1995.

[77] K. Robbie, C. Shafai, and M.J. Brett, "Thin films with nanometer-scale pillar microstructure," *Journal of Materials Research*, vol. 14, pp. 3158-3163, 1999.

[78] K. Robbie, J.C. Sit, and M.J. Brett, "Advanced techniques for glancing angle deposition," *Journal of Vacuum Science and Technology B*, vol. 16, pp. 1115-1122, 1998.

[79] K. Robbie and M.J. Brett, "Sculptured thin films and glancing angle deposition: Growth mechanics and applications," *Journal of Vacuum Science and Technology A*, vol. 15, pp. 1460-1465, 1997.

[80] B. Dick, J.C. Sit, M.J. Brett, I.M.N. Votte, and C.W.M. Bastiaansen, "Embossed polymeric relief structures as a template for the growth of periodic inorganic microstructures," *Nano Letters*, vol. 1, pp. 71-73, 2001.

[81] J.C. Sit, D. Vick, K. Robbie, and M.J. Brett, "Thin film microstructure control using glancing angle deposition by sputtering," *Journal of Materials Research*, vol. 14, pp. 1197-1199, 1999.

[82] D. Vick, Y.Y. Tsui, M.J. Brett, and R. Fedosejevs, "Production of porous carbon thin films by pulsed laser deposition," *Thin Solid Films*, vol. 350, pp. 49-52, 1999.

[83] T. Smy, D. Vick, M.J. Brett, S.K. Dew, A.T. Wu, J.C. Sit, and K.D. Harris, "Three-dimensional simulation of film microstructure produced by glancing angle deposition," *Journal of Vacuum Science & Technology a-Vacuum Surfaces and Films*, vol. 18, pp. 2507-2512, 2000.

[84] D. Vick, L.J. Friedrich, S.K. Dew, M.J. Brett, K. Robbie, M. Seto, and T. Smy, "Self-shadowing and surface diffusion effects in obliquely deposited thin films," *Thin Solid Films*, vol. 339, pp. 88-94, 1999.

[85] D. Vick, T. Smy, and M.J. Brett, "Growth behavior of evaporated porous thin films," *Journal of Materials Research*, vol. 17, pp. 2904-2911, 2002.

[86] B. Dick, M.J. Brett, and T. Smy, "Controlled growth of periodic pillars by glancing angle deposition," *Journal of Vacuum Science & Technology B*, vol. 21, pp. 23-28, 2003.

[87] M.W. Seto, K. Robbie, D. Vick, M.J. Brett, and L. Kuhn, "Mechanical response of thin films with helical microstructures," *Journal of Vacuum Science & Technology B*, vol. 17, pp. 2172-2177, 1999.

[88] P.I. Rovira, R.A. Yarussi, R.W. Collins, R. Messier, V.C. Venugopal, A. Lakhtakia, K. Robbie, and M.J. Brett, "Transmission ellipsometry of a thin-film helicoidal bianisotropic medium," *Applied Physics Letters*, vol. 71, pp. 1180-1182, 1997.

[89] B. Dick, M.J. Brett, T.J. Smy, M.R. Freeman, M. Malac, and R.F. Egerton, "Periodic magnetic microstructures by glancing angle deposition," *Journal of Vacuum Science and Technology A*, vol. 18, pp. 1838-1844, 2000.

[90] K. Robbie, D.J. Broer, and M.J. Brett, "Chiral nematic order in liquid crystals imposed by an engineered inorganic nanostructure," *Nature*, vol. 399, pp. 764-766, 1999.

[91] K. Robbie, A.J.P. Hnatiw, M.J. Brett, R.I. MacDonald, and J.N. McMullin, "Inhomogeneous thin film optical filters fabricated using glancing angle deposition," *Electronics Letters*, vol. 33, pp. 1213-1214, 1997.

[92] A.Y. Elezzabi, J.C. Sit, J.F. Holzman, K. Robbie, and M.J. Brett, "Thin film vertical diffraction gratings fabricated using glancing angle deposition," *Electronics Letters*, vol. 35, pp. 491-493, 1999.

[93] S.R. Kennedy and M.J. Brett, "Porous broadband antireflection coating by glancing angle deposition," *Applied Optics*, vol. 42, pp. 4573-4579, 2003.

[94] S.R. Kennedy, M.J. Brett, H. Miguez, O. Toader, and S. John, "Optical properties of a 3-dimensional silicon square spiral photonic crystal," *Photonics and Nanostructures*, vol. (in press), 2003.

[95] K.D. Harris, D. Vick, E.J. Gonzalez, T. Smy, K. Robbie, and M.J. Brett, "Porous thin films for thermal barrier coatings," *Surface & Coatings Technology*, vol. 138, pp. 185-191, 2001.

[96] M.J. Colgan and M.J. Brett, "Field emission from carbon and silicon films with pillar microstructure," *Thin Solid Films*, vol. 389, pp. 1-4, 2001.

[97] A.T. Wu, M. Seto, and M.J. Brett, "Capacitive SiO humidity sensors with novel microstructures," *Sensors and Materials*, vol. 11, pp. 493-505, 1999.

[98] A.T. Wu and M.J. Brett, "Sensing humidity using nanostructured SiO posts: Mechanism and optimization," *Sensors and Materials*, vol. 13, pp. 399-431, 2001.

[99] K.D. Harris, M.J. Brett, T.J. Smy, and C. Backhouse, "Microchannel surface area enhancement using porous thin films," *Journal of the Electrochemical Society*, vol. 147, pp. 2002-2006, 2000.

[100] K.D. Harris, J.R. McBride, K.E. Nietering, and M.J. Brett, "Fabrication of porous platinum thin films for hydrocarbon sensor applications," *Sensors and Materials*, vol. 13, pp. 225-234, 2001.

[101] H.K. Pulker, G. Paesold, and E. Ritter, "Refractive indices of $TiO_2$ films produced by reactive evaporation of various titanium-oxygen phases," *Applied Optics*, vol. 15, pp. 2986, 1976.

[102] B.A. Dick, "Properties and growth of thin films grown by glancing angle deposition," Ph.D. Thesis, University of Alberta 2003.

[103] H. van Kranenburg and C. Lodder, "Tailoring growth and local composition by oblique-incidence deposition: a review and new experimental data," *Materials Science & Engineering R Reports*, vol. R11, pp. 295-354, 1994.

[104] R.N. Tait, T. Smy, and M. Brett, "Structural anisotropy in oblique incidence thin metal films," *Journal of Vacuum Science and Technology A*, vol. 10, pp. 1518-1521, 1992.

[105] J.F. O'Hanlon, *A user's guide to vacuum technology*, Second ed. New York: Wiley, 1989.

[106] M. Malac and R.F. Egerton, "Observations of the microscopic growth mechanism of pillars and helics formed by glancing-angle thin-film deposition," *Journal of Vacuum Science & Technology A*, vol. 19, pp. 158-166, 2001.

[107] P. Lobl, M. Huppertz, and D. Mergel, "Nucleation and growth in TiO2 films prepared by sputtering and evaporation," *Thin Solid Films*, vol. 251, pp. 72-79, 1994.

[108] "PELA-1003 Manual,"

[109] J.M. Bennett, E. Pelletier, G. Albrand, J.P. Borgogno, B. Lazarides, C.K. Carniglia, R.A. Schmell, T.H. Allen, T. Tuttle-Hart, K.H. Guenther, and A. Saxer, "Comparison of the properties of titanium dioxide films prepared by various techniques," *Applied Optics*, vol. 28, pp. 3303-3317, 1989.

[110] Solaronix, "Ruthenium 535 bis-TBA Oxide Semiconductor Sensitizer," http://www.solaronix.com/menu2.html, 2003.

[111] Personal Communication: from T. Meyer to G. K. Kiema, "RE: Ru 535 TBA Spectra," Edmonton, AB, 2002.

[112] A. Fillinger and B.A. Parkinson, "The adsorption behavior of a ruthenium-based sensitizing dye to nanocrystalline $TiO_2$: coverage effects of the external and internal sensitization quantum yields," *Journal of the Electrochemical Society*, vol. 146, pp. 4559-4564, 1999.

[113] Y. Tachibana, K. Hara, K. Sayama, and H. Arakawa, "Quantitative analysis of light-harvesting efficiency and electron-transfer yield in ruthenium-dye-sensitized nanocrystalline $TiO_2$ solar cells," *Chemistry of Materials*, vol. 14, pp. 2527-2535, 2002.

[114] Solaronix, "Iodolyte TG 50 redox electrolyte," http://www.solaronix.com/menu2.html, 2003.

[115] M. Gomez, E. Magnusson, E. Olsson, A. Hagfeldt, S.-E. Lindquist, and C.G. Granqvist, "Nanocrystalline Ti-oxide-based solar cells made by sputter deposition and dye sensitization: Efficiency versus film thickness," *Solar Energy Materials & Solar Cells*, vol. 62, pp. 259-263, 2000.

[116] S. Nakade, M. Matsuda, S. Kambe, Y. Saito, T. Kitamura, T. Sakata, Y. Wada, H. Mori, and S. Yanagida, "Dependence of $TiO_2$ nanoparticle preparation methods and annealing temperature on the efficiency of dye-sensitized solar cells," *Journal of Physical Chemistry B*, vol. 106, pp. 10004-10010, 2002.

[117] N.-G. Park, J. van de Lagemaat, and A.J. Frank, "Comparison of dye-sensitized rutile- and anatase-based $TiO_2$ solar cells," *Journal of Physical Chemistry B*, vol. 104, pp. 8989-8994, 2000.

[118] J.-Y. Zhang, I.W. Boyd, B.J. O'Sullivan, P.K. Hurley, P.V. Kelly, and J.-P. Senateur, "Nanocrystalline $TiO_2$ films studied by optical, XRD and FTIR spectroscopy," *Journal of Non-Crystalline Solids*, vol. 303, pp. 134-138, 2002.

[119] K.N. Rao, "Influence of deposition parameters on optical properties of $TiO_2$ films," *Optical Engineering*, vol. 41, pp. 2357-2364, 2002.

[120] H. Selhofer, E. Ritter, and R. Linsbod, "Properties of titanium dioxide films prepared by reactive electron-beam evaporation from various starting materials," *Applied Optics*, vol. 41, pp. 756-762, 2002.

[121] M.D. Wiggins, M.C. Nelson, and C.R. Aita, "Phase development in sputter deposited titanium dioxide," *Journal of Vacuum Science & Technology A (Vacuum, Surfaces, and Films)*, vol. 14, pp. 772-776, 1996.

[122] S. Bosch, "Lens coating in thermal evaporation physical vapour deposition chambers: optimization of the geometrical configuration," *Journal of Physics D: Applied Physics*, vol. 26, pp. 124-129, 1993.

[123] S. Bosch, "Computer-aided procedure for optimization of layer thickness uniformity in thermal evaporaton physical vapor deposition chambers for lens coating," *Journal of Vacuum Science & Technology A*, vol. 10, pp. 98-104, 1992.

[124] R.P. Netterfield, "Uniform evaporated coatings on rotating conical workholders," *Journal of Vacuum Science & Technology*, vol. 19, pp. 216-220, 1981.

[125] R.H. Davis and S.R. Deo, "An evaporation system for the metallization of bilevel substrates," *Journal of Vacuum Science & Technology*, vol. 11, pp. 77-80, 1974.

[126] L.I. Maissel and R. Glang, *Handbook of thin film technology*. New York: McGraw-Hill, 1970.

[127] V. Mikhelashvili and G. Eisentein, "Effects of annealing conditions on optical and electrical characteristics of titanium dioxide films deposited by electron beam evaporation," *Journal of Applied Physics*, vol. 89, pp. 3256-3269, 2001.

[128] Solaronix, "Ti-Nanoxide HT transparent nanocristalline titanium oxide," http://www.solaronix.com/menu2.html, 2003.

[129] T. Trupke, P. Wurfel, and I. Uhlendorf, "Dependence of the photocurrent conversion efficiency of dye-sensitized solar cells on the incident light intensity," *Journal of Physical Chemistry B*, vol. 104, pp. 11484-11488, 2000.

[130] A. Andersson, N. Johansson, P. Broms, N. Yu, D. Lupo, and W.R. Salaneck, "Fluorine tin oxide as an alternative to indium tin oxide in polymer LEDs," *Advanced Materials*, vol. 10, pp. 859-863, 1998.

[131] Personal Communication: from T. Meyer to G. K. Kiema, "RE: Peeling off of $TiO_2$," Edmonton, AB, 2002.

[132] M. Suzuki and Y. Taga, "Numerical study of the effective surface area of obliquely deposited thin films," *Journal of Applied Physics*, vol. 90, pp. 5599-5605, 2001.

[133] Solaronix, "Ruthenium 620-1H3TBA oxide semiconductor sensitizer," http://www.solaronix.com/menu2.html, 2003.

[134] Solaronix, "Dye solar cell assembly," 2001.

[135] M. Suzuki, T. Ito, and Y. Taga, "Photocatalysis of sculptured thin films of $TiO_2$," *Applied Physics Letters*, vol. 78, pp. 3968-3970, 2001.